Hollow Cone Dark Field Imaging: Automatic Acquisition, and its Contrast for Magnesium

By
Farhang Parsa

A thesis submitted to
the Faculty of Graduate Studies
in partial fulfilment of
the requirements for the degree of
Master of Science

Department of Mechanical Engineering
Faculty of Engineering
University of Manitoba
Winnipeg, Manitoba

Abstract

Hollow Cone Dark Field (HCDF) imaging is a powerful technique, yet it remains under-used for contrast-orientation studies—particularly when rapid, well-timed illumination adjustments are required and, up to the present time of authoring this thesis, no dedicated simulation protocols exist.

The key obstacle is software fragmentation: conical-illumination simulation, beam-tilt control, automatic acquisition, and quantitative validation reside in separate programs. Researchers must therefore stitch together ad-hoc scripts and file conversions, hampering usability, reproducibility, and high-throughput studies.

This study addresses the challenge by presenting a single, automated framework that unifies the entire HCDF workflow. A common scripting layer (i) generates orientation grids and supercells, (ii) performs multi-slice simulations, (iii) drives the microscope through continuous hollow-cone tilts while capturing images autonomously, and (iv) overlays experimental and simulated patterns with full parameter logging—eliminating manual data hand-offs at every stage.

Demonstrated on magnesium crystals, the system simulates several hundred HCDF images, with experimental contrast matching simulation closely enough to validate both model and instrument settings. By fusing simulation, real-time acquisition, and validation into one cohesive environment, the framework transforms HCDF from a specialist method into a practical, high-throughput technique helpful for routine orientation mapping and in-situ deformation studies in both academic and industrial contexts.

Acknowledgments

I would like to express my deepest gratitude to all those who supported me throughout my M.Sc. studies, without whom this thesis would not have been possible.

I wish to extend my profound gratitude to Professor Guo-zhen Zhu for her steadfast support and patient mentorship. Under her guidance, I gained invaluable insights—spanning technical expertise in TEM operation and image simulation to the thoughtful design of meaningful experiments. Beyond her scholarly knowledge, Dr. Zhu's kindness and approachability created an environment in which I could continually learn and thrive. I am profoundly grateful for the many ways she has shaped my skills, confidence, and outlook as a researcher.

I am also indebted to my committee members, whose valuable guidance and thoughtful suggestions have greatly enriched my research. My heartfelt thanks extend to my group members and friends—Moein Imani Foumani, Zhina Razaghi, and Syed Taha Khursheed—for their camaraderie, discussions, and support.

I would like to extend my heartfelt gratitude to Dr. Lulu Guo for his dedicated support and guidance throughout the experimental phases of my work. His patience, encouragement, and generous investment of time were instrumental to my progress. My appreciation also goes to Dr. Yushun Liu, whose extensive knowledge and assistance were invaluable. Furthermore, I am thankful for the resources provided by the Materials Lab (MIM), where the microscope essential to this research are hosted, and I wish to acknowledge Dr. Abdul Khan for his crucial expertise and support during pivotal experimental stages.

Finally, I owe a special debt of gratitude to my wife, whose unwavering love and support have been the driving force that kept me going. Her belief in me has been a constant source of motivation and strength throughout this journey.

Dedication

To my wife, whose unwavering support and encouragement have been a constant source of strength; to my family, who have instilled in me the values and determination to persevere; and to my little one, whose imminent arrival already brings hope, motivation, and joy for the future.

Contents

Front Matter

List of Tables

List of Figures

Chapter 1
Introduction

1.1 Background and Motivations

Transmission electron microscopy (TEM) is a vital technique in materials science and structural biology, enabling high-resolution imaging and diffraction analysis of structures at sub-angstrom scales, particularly with the development of advanced aberration-corrected systems [1,2]. TEM derives structural information by analyzing how electron waves scatter due to the specimen's electromagnetic potential, and thus provides crucial insights into morphology, crystallography, composition, and chemical bonding of the materials. Recent advances—such as four-dimensional scanning TEM (4D-STEM) with ptychography—significantly improve resolution and sensitivity in materials science, while cryo-electron diffraction gains prominence in structural biology. Precise instrument alignment and comprehensive theoretical modeling remain essential for accurately capturing these slight scattering changes.

Magnesium (Mg) and its alloys boast low density, recyclability, and hydrogen storage potential, making them suitable for various energy, aerospace, and transportation applications [3–5]. However, their hexagonal close-packed (HCP) structure limits room-temperature formability by restricting active slip systems, which leads to pronounced deformation-induced textures and reduced ductility [6–9]. Thus, characterizing texture evolution and orientation changes in Mg—and in other crystalline or polycrystalline materials—demands reliable, high-resolution techniques. Traditional methods like electron backscatter diffraction (EBSD) in SEM, transmission Kikuchi diffraction (TKD), or diffraction spot-based TEM analysis can generate detailed orientation maps, but they often require extensive data acquisition or large sampling of reciprocal space. While some of these approaches successfully observe in situ orientation changes during plastic deformation, they frequently suffer from limited fields of view, orientation-dependent imaging constraints, or substantial time requirements for data collection. Dark-field (DF) imaging in TEM can circumvent certain drawbacks by selecting electrons from specific diffraction rings, thereby enabling real-time orientation tracking of active slip systems. However, conventional DF typically uses only a small fraction of any given diffraction ring and thus forfeits significant orientation information.

Hollow Cone Dark-Field (HCDF) imaging offers a promising solution to many limitations in traditional orientation analysis techniques. While previous studies primarily apply HCDF to grain size and dislocation analysis, its full potential for tracking orientation changes—such as the rotation of major slip planes across larger grain populations—remains underutilized. When systematically applied, HCDF can reveal real-time changes in active slip systems, twinning, and texture evolution. However, the absence of a clear, integrated framework for HCDF—combining simulation, automated image acquisition, and microscope control—continues to limit its broader adoption [144]. This research is supporting to address that gap by establishing a straightforward and automated workflow for HCDF imaging, tailored for magnesium but adaptable to other crystalline and polycrystalline materials. By enabling synchronized acquisition and analysis of HCDF image series via TEM scripting and simulations, this work enhances accessibility to real-time orientation tracking, supporting both advanced materials research and industrial applications where rapid and reliable control of texture evolution is critical.

1.2 Objectives

The overall objective of this research is to apply TEM scripting and image simulation tools to enable automated acquisitions of HCDF images using TEM and further interpretation of the acquired images of Mg. This includes: (i) to develop and integrate an automated software solution using TEM scripting for real-time HCDF data acquisition and microscope control; (ii) to allow the use of different electron microscopy simulation software tools in the same project to facilitate the full HCDF simulation chain. Experimental contrast obtained in (i) is used to compare and validate the simulation. The outputs provide a solid foundation for further technique development of tracking orientations during deformation, an essential topic for both academic and industrial applications.

1.3 Structure of this Thesis

Chapter II outlines the fundamentals of HCDF, detailing its principles, potential applications, and advantages over traditional techniques. Various software tools for automated TEM control are discussed, highlighting their capabilities and limitations.

Chapter III discusses the design and implementation of the HCDF Contrast Simulation Framework. It explains the multi-slice simulation approach, covers the process of generating orientation grids, explores methods for creating supercells, and describes strategies for automating the simulation workflow.

Chapter IV focuses on automated microscope control for HCDF. It explains how the scripting system is executed, addresses error handling and potential failure scenarios, and provides details about hollow cone scanning parameters. The chapter also reviews the software implementation for thickness measurement and hollow cone scanning operations.

Chapter V presents the results and discusses their significance. It evaluates the uniform grid of orientations, the effect of slice thickness, and the behavior of intensity oscillations. The chapter also illustrates hollow cone contrast on inverse pole figures and showcases experimental results, including the verification of Delphi TEM-scripting.

Chapter VI summarizes the findings of the thesis and offers suggestions for future work.

Finally, the thesis concludes with appendices, which contain scripts and their explanations, and Bibliography.

Chapter 2
Literature Review

2.1 Introduction

In recent years, electron microscopy evolves into an increasingly sophisticated discipline, with the emergence of HCDF imaging as a valuable technique. Despite its potential, HCDF remains underutilized and lacks a dedicated and integrated framework capable of automating both the simulation and experimental acquisition processes. The existing ecosystem of electron microscopy software is highly fragmented; researchers often rely on a disparate combination of tools to simulate, acquire, and validate HCDF contrast across multiple crystallographic orientations. This fragmented landscape poses significant challenges for usability, reproducibility, and high-throughput execution—especially in applications that require conical illumination modeling, dynamic beam tilting, and synchronization between simulation and instrument control.

Currently, many widely used electron microscopy software packages focus on specific segments of the processing pipeline. For instance, MTEX [95] is employed within MATLAB to generate orientation grids and fundamental zone-axis representations; Atomic Simulation Environment (ASE) [92], typically used via Python, is applied to build, orient, and orthogonalize atomic models; and abTEM [74] provides a Python interface for multi-slice simulations, though its direct support for HCDF-specific conical illumination conditions remains limited. On the other hand, highly accurate but standalone codes such as Kirkland's C++ multi-slice suite continue to be the gold standard for frozen phonon-based simulations but require significant manual setup and scripting expertise for batch processing across multiple orientations [32].

While frameworks such as abTEM and STEM_CELL [144] integrate supercell generation, frozen lattice multi-slice simulation, and basic post-processing into a single interface, they do not address the specific requirements of HCDF simulations. Moreover, software packages in materials-focused

2.1 Introduction

TEM often lack the direct connection to automation platforms that enable real-time acquisition and validation workflows.

In contrast, the field of cryo-electron microscopy (cryo-EM) sees substantial development in integrated and automated software platforms. For example, Scipion [146] is a modular framework designed to facilitate interoperability across different cryo-EM software tools while emphasizing reproducibility and traceability by logging all parameters and processing steps. Appion, closely tied to the Leginon project, integrates a wide range of cryo-EM processing tools through a centralized database and scripting architecture, allowing users to trace each data point back to the microscope settings and processing conditions [147], [47].

Automation in experimental acquisition is supported by several notable software tools. Leginon enables automated data collection and drift correction with metadata logging and session tracking; it is widely adopted for automated high-throughput cryo-EM imaging [47]. SerialEM, another prominent tool, offers flexible, scriptable control over TEM operations including tilt series acquisition and real-time correction for goniometer inaccuracies, and it is compatible with various hardware configurations including JEOL and FEI microscopes [48]. Digital Micrograph (DM), developed by Gatan, is extensively used for controlling TEM hardware, scripting acquisition routines, and enhancing detector functionality. It offers a proprietary but user-friendly scripting environment that has become a de facto standard in many TEM laboratories [60]. Additionally, TOM Toolbox provides an open-source MATLAB-based environment for low-dose acquisition, real-time alignment, and integration with specimen-sensitive imaging workflows [49].

Each of these automation solutions has its strengths, yet none offers native support for HCDF-specific acquisition protocols—such as continuous beam tilt within a hollow cone geometry or synchronized acquisition of contrast series across multiple orientations. Furthermore, while tools like SPIDER [148], EMAN2 [149], SPARX [150], and Xmipp [151] significantly advance data processing and reconstruction in cryo-EM, their focus remains on single-particle analysis rather than diffraction-based contrast simulation and orientation-resolved acquisition.

The lack of an integrated solution leads researchers to manually connect these tools through ad hoc scripting and complex file conversions, often involving different programming languages, coordinate systems, and data formats. This approach not only increases the possibility of error but also limits scalability and reproducibility.

2.2 Hollow Cone Illumination Technique

TEM is a vital technique in materials science and biology, enabling researchers to investigate structures at the nanoscale. TEM operates through two primary approaches: conventional TEM (CTEM) and scanning TEM (STEM). In CTEM, the specimen is illuminated by a uniform plane wave, and the transmitted electron signals are magnified and focused on an imaging plane using a lens located beyond the sample. In contrast, STEM involves scanning the specimen with a finely focused electron beam, and the signals generated at each beam position are collected by a detector placed in the diffraction plane after the sample. This allows STEM to produce detailed spatially resolved data based on the beam's interaction with the material at specific locations.

In bright-field TEM (BF-TEM), an aperture in the back focal plane of the objective lens selectively allows unscattered or weakly scattered electrons to form the image. This contrast mechanism is particularly useful for analyzing sample thickness variations, crystallographic defects, and phase boundaries. Conversely, dark-field TEM (DF-TEM) enhances contrast by selecting only the diffracted electrons to contribute to the image, effectively making strongly scattering regions appear bright against a dark background. DF-TEM is widely used for imaging crystalline defects, dislocations, strain fields, and specific crystallographic orientations within a material [13].

Hollow cone illumination (HCI) addresses this by illuminating the specimen with a conical distribution of electrons rather than a single, focused beam or a narrow parallel beam. HCI is introduced by Scherzer in the late 1940s as a means of improving TEM resolution [12]. Because HCI utilizes a broad range of incident angles, it effectively captures the contributions from multiple diffraction spots simultaneously. This wide-angle approach also circumvents many of the CTF-related constraints encountered in CTEM, as it mitigates phase-contrast effects that can otherwise distort quantitative analyses. The resultant images from HCI are thus more representative of the specimen’s overall scattering behavior, making analyses less susceptible to misleading artifacts from strong diffraction maxima. The ability of hollow cone illumination to reduce phase contrast artifacts has made it a potent approach for high-resolution imaging with conventional TEM, improving image clarity and interpretability.

To generate a cone-shaped beam, Hollow Cone Illumination (HCI) can be achieved in two ways: (1) a hardware approach that uses a donut-shaped condenser aperture to produce conical illumination, or (2) a software approach in which tilt coils process the electron beam to form a ring-shaped diffraction pattern [13]. Since its inception, HCI is extensively studied. In 1953, Willis W. Mathews publishes a study demonstrating that HCI improves image clarity by enhancing contrast—i.e., increasing the intensity difference between features so that they appear more distinct from one another—thereby making fine details easier to discern [14]. Due to this enhanced contrast, HCI finds applications in fields such as dark-field microscopy of biological specimens [15], crystallography, and orientation mapping.

2.2.1 Hollow Cone Illumination Using an Annular Condenser Aperture

Under this method, the second condenser lens focuses a reduced image of the illumination source onto the specimen, while the objective lens projects an image of the annular aperture onto its rear focal plane. As illustrated in Figure 1, the electron beam follows a defined trajectory—passing through the annular condenser aperture, interacting with the specimen, and ultimately converging in the objective lens' rear focal plane. Sometimes referred to as the back focal plane, this location is where the lens unites all diffracted beams, thereby producing a diffraction pattern rather than a real-space image.

Within this framework, both dark-field and bright-field imaging modes can be realized by modifying how the electrons are selected after passing through the specimen. Dark-field imaging involves inserting a small objective aperture to block unscattered electrons, thus allowing only scattered electrons to form the image contrast. For bright-field imaging, two main strategies may be employed. The first entails enlarging the objective aperture (Diameter "d" in Figure 1), so that both scattered and unscattered electrons contribute to the final image. The second method narrows the diameter of the annular condenser aperture (Diameter "D" in Figure 1), which not only permits higher beam currents but also facilitates easier correction of objective astigmatism. This latter approach is particularly beneficial when operating under high-intensity beam conditions [13].

2.2 Hollow Cone Illumination Technique

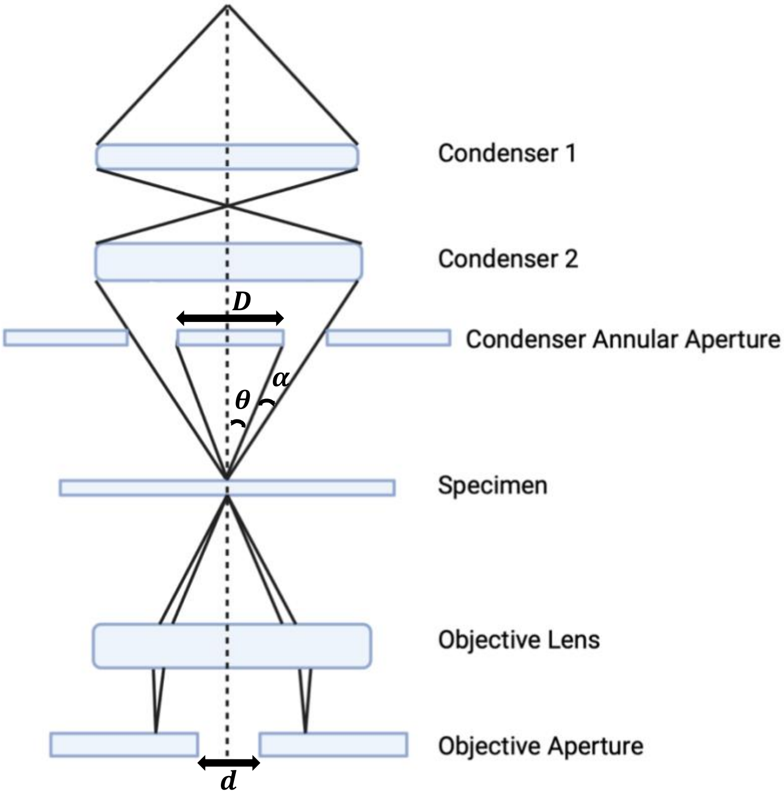

Figure 1: Diagram depicting the beam path for dark field imaging utilizing an annular condenser aperture. The condenser aperture is replaced by an annular opening—a "ring" with an inner and outer radius—the resulting electron beam emerging from this annulus is inherently cone-shaped. Specifically, the inner radius of the aperture blocks the central portion of the beam, while the outer radius confines the beam to a ring profile. Consequently, when the aperture is projected onto the specimen via the condenser lens, the electrons converge and diverge in a manner that outlines a hollow cone.

While hollow cone illumination offers several benefits, including high beam current, ease of correcting objective astigmatism, and axial symmetry, it has several limitations that reduce its practicality [16]:

- Focusing Requirements: The illumination must be accurately focused on the specimen plane to ensure proper coverage; otherwise, areas near the optical axis may remain insufficiently illuminated.
- Fixed Illumination Angle (θ, see Figure 1): It is determined by the aperture size.
- Fixed Divergence Angle (α, see Figure 1): Because the aperture size is fixed, the divergence angle remains constant unless a different annular aperture is used.
- Limited Microscope Aperture Space: In many electron microscopes, the condenser aperture holder is limited in size and positions, often accommodating a small number of circular apertures by default. When an annular aperture is introduced, it must occupy one

of these limited slots. Switching between circular and annular apertures typically requires physically exchanging these apertures on the aperture drive, followed by an instrument alignment procedure to ensure the beam profile is correctly configured for the new aperture geometry.

- Fabrication Challenges: Manufacturing annular apertures is a difficult and precise process.

Due to these constraints, an alternative method involving electronic control of the cone illumination is introduced, offering a more flexible and practical approach.

2.2.2 Electronic Cone Illumination

An electronic approach to creating cone illumination involves using the microscope's tilt coils with standard apertures and applying modulated waveforms to the x and y tilt coils [16]. By using sine waves with a 90° phase shift between them, the electron beam traces a circular path, forming a cone of illumination on the specimen.

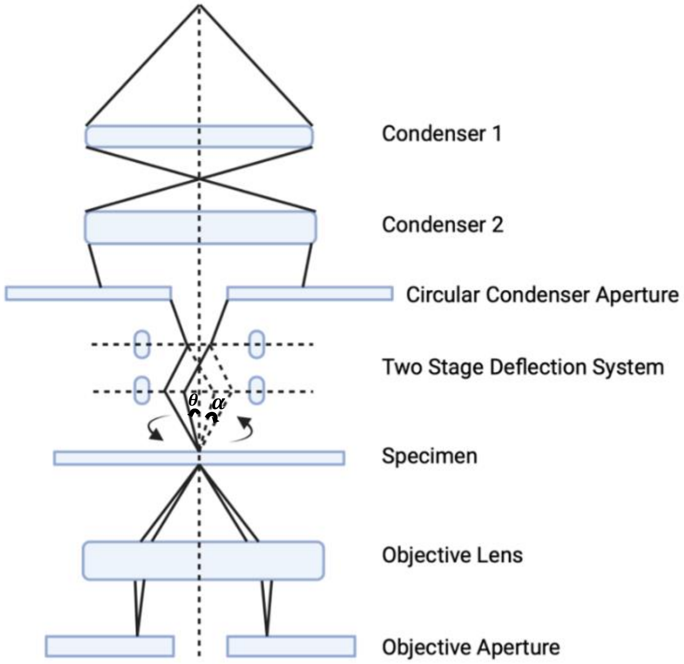

Figure 2: Diagram illustrating the ray paths for electronic hollow cone illumination.

2.2 Hollow Cone Illumination Technique

The key components of the electronic cone illumination system are the function generator and control unit.

Function Generator: This is a versatile piece of electronic test equipment designed to produce signals of varying frequency, amplitude, and waveform shape. In general laboratory settings, function generators are used to drive or test electronic circuits by providing a controlled signal input.

Control Unit: This unit manages the function generator signals and routes them to the x and y tilt coils of the microscope. Its key components include:

- A voltage attenuator to regulate the signal amplitude.
- A divider circuit that generates identical waveforms for the x and y coils, with an option to introduce a phase shift between the two waveforms.
- Isolation amplifiers for both coils, and
- Switches to control whether the x and y coils operate individually or together, with an off option for normal operation.

By properly adjusting the amplitudes and phase shifts of the signals, the electron beam traces a circular trajectory in the back focal plane of the objective lens, effectively creating a cone of illumination. This method enables precise control over both the azimuthal angle and angular divergence of the cone. When the electron beam is made to travel in a circular path, as in hollow cone illumination, the azimuthal angle describes how far around the circle the beam has swept relative to this reference direction (rotating arrows in Figure 2).

Electronic cone illumination offers several advantages over the traditional annular aperture technique. It allows the azimuthal angle to be modified without reducing the beam intensity at the specimen plane and eliminates the need to realign the microscope when switching between normal and hollow cone modes. Moreover, the illumination spot remains fixed on the specimen plane regardless of changes in the azimuthal angle, enabling a smooth transition between bright-field and dark-field imaging. The ability to electronically adjust the cone's angular divergence adds further versatility, providing a level of flexibility in imaging conditions that is not possible with fixed annular apertures.

2.3 Contrast Transfer Function in HCI

2.3.1 Conventional CTF

The contrast transfer function (CTF) is a mathematical representation of how imaging occurs in TEM under given illustration conditions and optics aberrations, formulated in terms of Fourier analysis. In an ideal scenario, TEM images would accurately depict the electron density of the specimen through direct projections. However, due to the influence of microscope optics, the images deviate from this ideal. In real space, aberrations, and defocus manifest as complex, overlapping features that can be difficult to interpret by simple visual inspection. However, in the frequency (Fourier) domain, each spatial frequency component appears separately, allowing one to see exactly which frequencies are being emphasized or attenuated. This clearer separation of frequency components makes it far easier to identify how defocusing, lens imperfections, and other aberrations are influencing the final image. Consequently, analyzing the Fourier transform provides a more direct view of the underlying contrast transfer behavior, making it an ideal tool for diagnosing and correcting optical distortions.

In on-axis imaging, the specimen is illuminated with a (nearly) parallel beam, and the lens aberrations—including defocus Δf and spherical aberration C_s can be encapsulated in a phase shift term $\chi(\alpha)$. This term describes how much the scattered electron wave is shifted relative to the unscattered wave at a given scattering angle α. A common form of $\chi(\alpha)$ is given by [17]:

$$\chi(\alpha) = \frac{2\pi}{\lambda}\left[-C_s\frac{\alpha^4}{4} + \Delta f\frac{\alpha^2}{2}\right] \qquad \textit{Eq 1}$$

where λ is the electron wavelength, Δf is the defocus (positive values typically indicating under focus), and C_s is the spherical aberration coefficient. In axial illumination, the image contrast can be described by a CTF that depends on $\sin\chi(\alpha)$, $\cos\chi(\alpha)$, and other relevant factors (e.g., amplitude vs. phase contrast contributions).

2.3.2 HCI-CTF

HCI, however, departs from this single on-axis beam paradigm by illuminating the sample from a full ring of angles rather than from a single direction. This off-axis approach introduces two principal modifications. First, every ray within the illumination cone has a different incidence angle, causing the image to shift by $s = M\Theta_c$ where M is the magnification and Θ_c is the semi-angle of the cone. Second, because the cone subtends 2π in azimuth, the final CTF results from integrating the phase contributions around the entire annulus.

To obtain the hollow cone CTF, one starts with the same general principles as the on-axis case:

- The scattered electron wave picks up an aberration-induced phase $\chi(u)$.
- The objective lens aperture or any other lens function is applied in reciprocal space.
- The final image contrast arises from the interference between the scattered and unscattered components.

However, for HCI, each incident angle on the annulus effectively corresponds to a different “tilt” of the incident wave. Mathematically, this off-axis illumination can be represented by an additional phase term, and the total electron wave field becomes an integral over all angles around the ring. This leads to the following hollow cone CTF $L(q, \Theta_c)$, which incorporates the same physical effects as the on-axis case—defocus and spherical aberration in particular—but must also account for the off-axis geometry and the continuous distribution of azimuthal angles [18]:

$$L(q,\Theta_c) = -\frac{1}{2\pi}\int_0^{2\pi} d\alpha\, A\left(f\Theta_c + \frac{f}{k}q\right)\sin[\gamma\left(f\Theta_c + \frac{f}{k}q\right) - \gamma(f\Theta_c) - sq\Theta_c] \qquad Eq\ 2$$

Here, q is the spatial frequency vector, and $A\,(f\Theta_c + \frac{f}{k}q)$ is the aperture function that defines which scattering angles contribute to the image. The function γ encapsulates the lens aberrations (including defocus and spherical aberration) evaluated at the off-axis angles, how this links to $\chi(u)$. The term $sq\Theta_c$ represents the lateral displacement in the image plane due to the oblique incidence, and the integral from 0 to 2π indicates that all azimuthal angles around the cone are considered, k is the wave number ($k = \frac{2\pi}{\lambda}$), f is the focal length of the objective lens and the other terms are defined previously.

2.3 Contrast Transfer Function in HCI

Conceptually, this expression shows how hollow cone illumination "averages" the phase shift contributions from every direction in the annulus [18]. In contrast to on-axis imaging, which only considers a single angle, HCI thus mitigates certain strong interference or Fresnel fringe effects by combining multiple angles. The cost of this broader coverage is that interpretation of the resulting images can become more complex. Nonetheless, hollow cone illumination can provide a more isotropic contrast transfer, making it attractive for applications where phase contrast benefits from averaging out directional dependencies.

Achieving an optimal CTF in HCI requires balancing defocus, aperture size, cone radius, and coma-free alignment for stable, high-quality imaging. Although determining the optimal defocus can be more complex in HCI, once identified, maintaining it is comparable to on-axis modes. Slightly larger apertures (about ten percent above the ideal diameter) help accommodate minor misalignments without substantially degrading image quality. For crystalline specimens, aligning the cone radius with specific Bragg reflections maximizes diffraction-based contrast or crystallographic data. Proper centering and preserving the circularity of the cone circle ensure uniform illumination, while coma-free alignment prevents comet-shaped distortions by matching the cone axis with the optical axis. This becomes particularly critical with larger cone radii, where even small alignment errors are magnified [17].

As illustrated in figure 3, a direct benefit of HCI is that the initial zeros of the phase contrast transfer function can shift to higher spatial frequencies compared to axial imaging, implying that finer structural details become accessible [17]. When the cone radius and defocus are tuned optimally, the point-to-point resolution is improved, as smaller features are effectively transferred before the CTF's first zero occurs. Consequently, HCI can reveal details beyond those typically captured under on-axis illumination, provided that the parameters—defocus, aperture size, cone radius, cone centering, and coma-free alignment—are all carefully managed.

2.3 Contrast Transfer Function in HCI

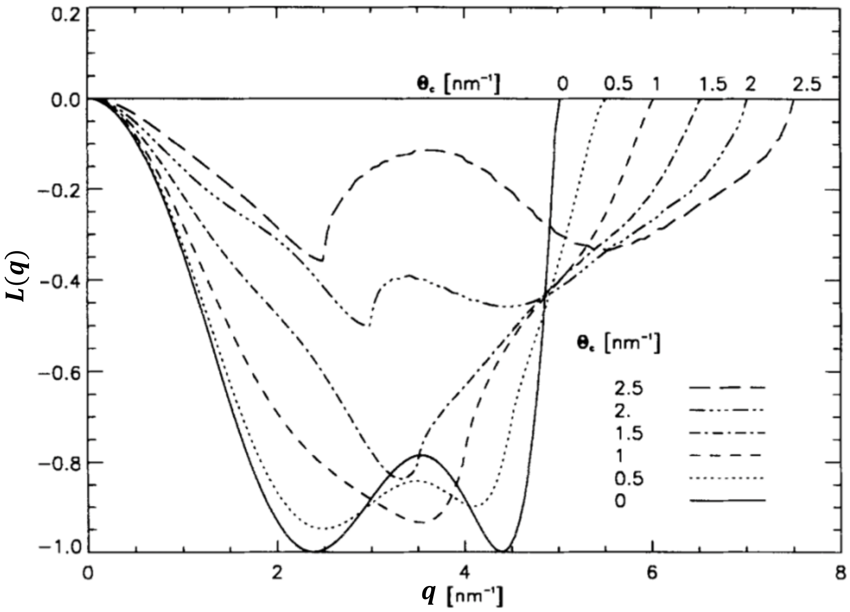

Figure 3: The PCTF $L(q)$ assuming coherent illumination with cone radii $\Theta_c = 0 - 2.5$ nm^{-1} (Θ_c is same as θ in figure 1) and optimum defocus each. The objective aperture radius is $\Theta_0 = 5$ nm^{-1}. Solid line (Corresponding to $\Theta_c = 0$) is for the conventional axial PCTF [17].

2.4 Applications

2.4.1 Different techniques based on HCI

Techniques based on hollow cone illumination (HCI) gain increasing importance in materials science since the late 1990s and early 2000s. Among these, hollow cone dark-field (HCDF) transmission electron microscopy (TEM) is widely employed to enhance contrast and obtain detailed crystallographic information from nano- and micro-crystalline samples. Researchers use HCDF TEM to investigate secondary phases, precipitates, dislocations, grain boundaries, and crystal orientations, finding it particularly valuable for visualizing grain boundaries and extracting precise structural data in nanocrystalline materials.

A closely related approach is precession electron diffraction (PED), introduced by Vincent and Midgley in Bristol, UK, in 1994 [10]. PED involves tilting the incident electron beam around the optical axis to produce a quasi-kinematical diffraction pattern, effectively minimizing dynamical scattering effects. The first commercial retrofit precession system appears in 2004 [11], popularizing PED for structure solution, phase identification, and orientation mapping. Building on concepts from both HCDF and PED, a specialized variant—precession illumination hollow cone dark field—combines the contrast-enhancing power of hollow cone illumination with the reduced dynamical artifacts afforded by beam precession.

HCDF-TEM emerges as a highly effective technique for high-resolution orientation imaging in nanocrystalline materials. Traditional methods such as Orientation Imaging Microscopy (OIM) in a scanning electron microscope (SEM) [20] achieve lateral resolutions on the order of 20–80 nm, but adapting these methods to TEM poses challenges related to resolution and reliability. In conventional TEM, orientation measurements often rely on techniques like Kikuchi diffraction, selected area diffraction, and convergent beam diffraction [21]. However, these approaches have inherent limitations: selected area diffraction lacks sufficient resolution, while Kikuchi and convergent beam diffraction patterns become unreliable with smaller probe sizes, particularly in thin or heavily deformed samples. Moreover, collecting many data points can be time-consuming and prone to sample drift, and the intensity gradients in diffraction patterns complicate automated analyses.

2.4 Applications

HCDF imaging tackles the drawbacks of conventional TEM orientation methods by recording a series of dark-field images at varying beam tilts. Each pixel’s brightness is measured as the beam tilts, yielding intensity–angle curves that combine into reconstructed diffraction patterns (RDPs). For instance, a 256×256 image can generate 65,536 RDPs, with spatial and angular resolutions determined by magnification, pixel count, and tilt range [21].

These RDPs are then treated like standard diffraction patterns, enabling automated orientation indexing adapted from EBSD approaches. Mapping tilt angles to a 2D grid captures each pixel’s reciprocal-space signal, facilitating spot detection, lattice-spacing calculations, and the assignment of Miller indices. By iterating this process for multiple reflections and ensuring internal consistency, one obtains precise local crystal orientations on a pixel-by-pixel basis. Consequently, HCDF imaging—particularly when combined with beam precession—offers a powerful, high-resolution technique for analyzing complex microstructures in TEM.

2.4.2 Application of HCI in Materials Research

Nanocrystalline materials, defined by grain sizes below 100 nm, possess distinctive physical and mechanical properties, primarily due to their high density of grain boundaries. For example, nanocrystalline copper exhibits a yield strength that is more than six times greater than that of its coarse-grained counterpart, as the dense grain boundaries inhibit dislocation movement. Similarly, in ultra-thin copper films, electrical resistivity increases with decreasing film thickness because conduction electrons experience enhanced scattering at the grain boundaries.

A study [43] employs HCDF TEM to investigate thin copper films and bulk nanocrystalline aluminum samples. Fine microstructures enhance image clarity and detail in HCDF. The authors emphasize the vital role of sample preparation for obtaining high-quality HCDF images, noting that even minor imperfections in specimen thickness, cleanliness, or crystallinity can hinder the visibility of microstructural features. Consequently, rigorous control over both the fabrication and preparation stages is critical for reliable TEM-based investigations.

In another study [44], HCDF-TEM is employed to investigate dislocation arrangements within nano- and micro-scale grains of trimodal aluminum metal matrix composites (MMCs). Compared to conventional bright-field or selected-area diffraction imaging, HCDF-TEM offers enhanced flexibility in isolating specific diffraction conditions. After acquiring HCDF-TEM images under optimized conditions, dislocation densities are determined using an area-based approach. The results reveal that dislocation strengthening significantly contributes to the mechanical properties of these composites, particularly in their nanocrystalline regions, demonstrating HCDF-TEM's advantage in both detecting and quantifying lattice defects. By permitting systematic adjustments of the diffraction vector, excitation error, and beam tilt, HCDF-TEM ensures that subtle dislocation structures are captured more reliably than in standard TEM imaging modes, making it an invaluable tool for detailed microstructural characterization.

A study [45] introduces Precession Illumination Hollow Cone Dark Field (PI-HCDF) imaging as an effective approach for determining grain sizes in nano-scale polycrystalline aggregates, specifically addressing the challenges of analyzing nanocrystalline materials. Compared to standard HCDF, PI-HCDF combines HCDF imaging with a precessed electron beam, meaning the beam is tilted around the optical axis at a controlled angle. This additional beam precession helps minimize dynamical diffraction effects and produces more uniform diffraction conditions, thereby enhancing the visibility of grain boundaries. In PI-HCDF, image contrast is influenced by both the objective aperture size and the precession angle, which together allow for selective sampling of grains under specific diffraction conditions. This method is applied to investigate nickel-aluminum alloys and the heat-affected zones (HAZ) in thin aluminum films processed by pulsed lasers, revealing sharp grain boundaries near the melted pool edge—indicative of localized grain growth—while the original nanocrystalline grain size remains unaffected. By offering improved boundary detection and more consistent diffraction contrast, PI-HCDF provides enhanced accuracy in grain size measurement compared to conventional HCDF [45].

In further research [46], PI-HCDF imaging is employed to quantify the $L1_0$ FePt phase fraction in annealed Fe/Pt multilayer films—an analysis that proves challenging for standard X-ray diffraction (XRD) and conventional TEM methods because both the $L1_0$ and disordered face-centered cubic (FCC) phases exhibit similar diffraction patterns. By incorporating a precessed electron beam in HCDF, PI-HCDF can selectively target specific diffraction rings associated with the $L1_0$ phase. This targeted imaging strategy ensures that only grains satisfying the unique $L1_0$ diffraction condition appear brightly in dark-field images, thereby isolating $L1_0$ from other phases that share similar diffraction signatures. In contrast, XRD averages signals over the entire sample, often producing overlapping peaks for phases with closely spaced reflections, and conventional TEM may not effectively distinguish between slightly different lattice parameters or orientations. The rotating, off-axis illumination in PI-HCDF circumvents these issues by systematically scanning the chosen diffraction condition, resulting in high-contrast separation of $L1_0$ FePt grains and enabling accurate determination of the $L1_0$ volume fraction in the sample.

2.5 Simulation in TEM

2.5.1 Fundamentals

Two main approaches—Bloch wave theory [19] and the multi-slice algorithm [20]—are instrumental in TEM image simulation, yielding equivalent results for high-resolution TEM (HRTEM), diffraction contrast, and convergent beam electron diffraction (CBED) patterns [21,22]. In Bloch wave theory [19], the crystal potential is treated as a repeating periodic field through which the incident electron wave travels. The total wavefunction within the crystal is then represented as a superposition of Bloch states—eigenfunctions that inherently satisfy the crystal's translational symmetry. By appropriately combining these states, Bloch wave simulations can capture phase and amplitude changes arising from multiple scattering events, providing accurate descriptions of diffraction contrast and phase contrast in high-resolution TEM (HRTEM) [21,22]. In contrast, the multi-slice algorithm [20] discretizes the specimen along the electron propagation direction into a series of thin slices. The electron wavefunction is sequentially propagated through each slice, where it acquires phase shifts based on the local scattering potential. These incremental modifications are accumulated across the full sample thickness, ultimately producing a simulated exit wave at the sample's exit surface. This stepwise approach is computationally robust and has been widely applied to HRTEM imaging, diffraction contrast, and convergent beam electron diffraction (CBED), yielding results comparable to Bloch wave methods [21,22].

2.5.2 Software development: Computational power considerations

The field of TEM simulations undergoes substantial growth, propelled by the need to interpret increasingly complex experimental data and to capture subtle phenomena such as chemical bonding and electron redistribution. Early computational methods often rely on the independent atom model (IAM), which treats the specimen potential as a sum of isolated atomic potentials.

2.5 Simulation in TEM

While IAM can be sufficient for many applications, it neglects the valence electron density and any charge transfer between atoms—critical factors in materials where bonding plays an important role [19–23]. The advent of density functional theory (DFT)-based potentials addresses this limitation by incorporating valence electron distributions, making it possible to predict scattering signals more accurately and to model phenomena such as phase-contrast variations and electron holography with greater fidelity.

Beyond the refinement of specimen potential, numerical methods for propagating electrons through the material also advance. The multi-slice algorithm, a workhorse for high-resolution TEM simulations, is continually optimized and parallelized to leverage modern, high-performance computing (HPC) resources. Many groups now utilize graphics processing units (GPUs) to accelerate the computationally demanding matrix operations inherent in the multi-slice procedure, leading to substantial speed gains and enabling larger-scale simulations of extended defects, interfaces, and thicker specimens.

A range of user-friendly software packages also reflects this progress. Tools such as Dr. Probe [24], QSTEM [25], PRISM/Prismatic [26], and xHREM [27] evolve in tandem with the growing capabilities of electron microscopes themselves. MULTEM [152] exploits GPU computing to accelerate multi-slice diffraction and imaging calculations, combining accuracy with speed on CUDA hardware. Later releases add support for multiple TEM/STEM modes and large datasets, making realistic simulations of thick specimens or wide fields of view feasible; the code is used to generate large machine learning datasets and to prototype advanced imaging methods. STEMsalabim [153] targets high-throughput STEM studies on HPC clusters: its distributed CPU parallelization lets users sweep many thicknesses, orientations, or 3D supercells in batch mode. μSTEM [154] focuses on inelastic processes—phonon excitation, thermal diffuse scattering, EELS—pairing detailed quantum mechanical models with early GPU acceleration. Together, these packages exemplify the field’s movement toward automated, high-performance simulation workflows capable of running hundreds of calculations in parallel for systematic comparison with large experimental datasets. There are also scripting libraries like py_multislice and others built on machine-learning frameworks PyTorch or GPU libraries CuPy that implement multi-slice and PRISM algorithms for researchers who prefer Python-based workflows [153, 154]. These newer tools, along with the comprehensive platforms described above, form an ecosystem of TEM simulation software. Importantly, many modern packages strive to interface with experimental workflows—either by enabling on-the-fly data analysis or by providing hooks for real-time image comparison—blurring the line between pure simulation and interactive experimentation. These packages commonly implement advanced features to incorporate lens aberrations, partial coherence, detector performance, and dynamic scattering effects, allowing researchers to tailor simulations to specific experimental parameters. However, atomic models need to be constructed and inputted into these packages.

Recent developments in four-dimensional STEM (4D-STEM) and ptychography further underscore the importance of robust, high-speed simulation frameworks [28]. By recording entire diffraction patterns at each probe position, 4D-STEM gathers an enormous amount of spatial and reciprocal-space information. Accurate modeling requires simulating a convergent electron probe interacting with the specimen at multiple incidence angles and capturing the diffraction signal on a pixelated detector. Advanced algorithms, sometimes employing DFT-derived potentials, help researchers interpret these large datasets—revealing local strain, electric fields, or bonding characteristics at sub-angstrom resolution.

Finally, incorporating machine learning (ML) and artificial intelligence (AI) promises to accelerate both the generation and interpretation of simulated data. AI-driven approaches can optimize model parameters, adaptively refine simulation settings based on experimental feedback, and streamline repetitive tasks like parameter sweeps in high-dimensional phase space [29]. As hardware, algorithms, and modeling strategies co-evolve, the next generation of TEM simulations is poised to capture an even broader range of physical phenomena, from subtle shifts in valence electron density to the dynamics of in situ experiments, cementing their role as an indispensable partner to modern electron microscopy.

2.5.3 Multi-Slice Simulation

The multi-slice algorithm is a highly adaptable approach for simulating different types of TEM measurements, tailored to the initial electron probe wave function and the method used to detect the exit wave function. At its core, the algorithm works by segmenting the specimen's electrostatic potential into a series of thin slices along the z-axis, which aligns with the electron beam direction. The electron wave is treated in two alternating steps: first, it transmits through each slice, where it interacts with the projected potential of the atoms (modeled as a phase object); second, it propagates to the next slice.

2.3.1.1 Electrostatic Potentials in Multi-slice

In multi-slice simulations, the choice of specimen potential is central to accurately capturing the electron-specimen interaction. In the present work, the independent atom model [88] is employed, where the total potential is treated as a sum of isolated atomic potentials. This approach, though it neglects valence electron redistributions, is computationally efficient and is sufficient for many applications—particularly where the contrast is primarily governed by elastic scattering at atomic cores. The electron charge distribution of an atom can be determined through first-principles methods, such as Hartree-Fock [82–83] or density functional theory [84–85]. From this charge distribution, the electrostatic potential is derived using Poisson's equation. In many multi-slice simulation codes, atomic potentials are provided in a pre-parametrized form, with parameter tables for each element derived from separate, first-principles calculations. These parameterizations offer approximate atomic scattering factors that account for radial dependencies of the potential, often relying on well-established models such as those by Lobato and Van Dyck [86] or Kirkland [32]. By fitting the potential for each element to a functional form, these models enable robust and efficient scattering calculations, making them particularly useful when elastic (nuclear) interactions are the dominant source of contrast.

2.3.1.2 Projected Potentials and Slicing Techniques

In multi-slice simulations, the specimen's three-dimensional potential is partitioned into two-dimensional slices along the beam direction, allowing stepwise wavefunction modification. Slice thickness directly impacts both accuracy and computational cost: thinner slices better approximate continuous variations but require more computations, while thicker slices risk numerical errors yet reduce runtime. The potential within each slice can be incorporated using two main approaches. Finite projection integrals [91] numerically integrate across the slice thickness for higher fidelity, though at increased computational expense, whereas the infinite projection method [90] is faster but less precise, treating each atomic potential layer with delta functions and applying analytic integration in Fourier space.

2.3.1.3 Other Consideration in Multi-slice algorithm

The multi-slice algorithm remains one of the most widely used methods for image simulation, and numerous software packages implement it [30–41]. In early simulations, comparing computed and experimental images often reveals inconsistencies, such as the so-called "Stobbs factor" [23], which denotes a systematic discrepancy between simulated and experimental intensities. This discrepancy originally necessitates arbitrary scaling (e.g., multiplying the simulated contrast by a factor) to align with experimental data. Advances in normalization methods and digital image processing have since reduced the impact of the Stobbs factor, enabling TEM to evolve into a more quantitative analytical tool in which image simulations play a critical role [30].

The flexibility of the multi-slice approach enables extensions to include effects such as inelastic scattering [38], backscattering [39], and innovations like "real space" multi-slice [40]. Inelastic scattering models how electrons lose energy within the specimen (e.g., via phonon interactions or ionizations), while backscattering accounts for electrons that scatter to high angles and potentially return toward the source. The "real space" variant of the multi-slice algorithm employs propagation steps defined directly in real space, offering alternative pathways for computational efficiency and precision in certain simulation scenarios. The "frozen lattice" or "frozen phonon" method, a key advancement within the multi-slice framework, models thermal diffuse scattering (TDS) by assigning random displacements to atoms (simulating phonon vibrations) and taking a Monte Carlo average of the resulting intensities. Initially limited to uncorrelated vibrations, this method has been refined to incorporate realistic phonon dispersions [22] and inelastic processes such as plasmon loss and inner-shell ionization [41,42].

The widespread adoption of scanning TEM (STEM), often performed in conjunction with energy-dispersive X-ray (EDX) spectroscopy and electron energy loss spectroscopy (EELS), establishes frozen-lattice multi-slice as the standard method for thermal diffuse scattering (TDS) simulations, particularly in high-angle annular dark field (HAADF) STEM, but also in TEM and CBED [66,67]. In these analyses, a finely focused electron probe is rastered over the specimen, while local signals (e.g., EDX or EELS spectra) are recorded. At large scattering angles typical of HAADF detection, atomic vibrations (phonons) lead to significant TDS contributions that shape the observed intensity. By modeling these vibrations as static, random displacements of atoms and averaging the resulting wavefronts over multiple iterations, the frozen-lattice (or frozen-phonon) approach captures the inelastic processes and background scattering essential for accurate EDX and EELS quantification in STEM experiments.

Kirkland's pioneering work on frozen-phonon routines for high-resolution TEM, CBED, and STEM simulations sets an early benchmark, with separate routines for atomic potential calculation, image formation, and probe-shape determination [32]. However, the original text-based, serial codes offer limited visualization capabilities and lack tools for modifying supercells or optimizing model parameters. As a result, subsequent developments focus on adding user-friendly interfaces, parallel computation, and more flexible data handling, all of which expand the scope and practicality of frozen lattice multi-slice simulations.

While parallel computing expedites the lengthy process of multi-slice calculations, there is limited progress in user interfaces and modeling tools [68–72]. The multi-slice algorithm itself faces challenges related to unit cell symmetry and periodicity, complicating simulations along non-rectangular zone axes [73]. Some methods, such as replicating supercells to approximate rectangular symmetry, partially address these issues, though they remain crucial in frozen phonon STEM simulations where probe size must match the supercell dimensions, and high-frequency sampling is necessary to capture diffuse scattering accurately.

Recent advancements in STEM simulations are marked by the introduction of the PRISM algorithm, which significantly enhances computational efficiency by leveraging modern hardware, such as graphics processing units (GPUs). This innovation accelerates simulations without compromising accuracy. Additionally, new software tools like abTEM [74], a Python-based multi-slice image simulation package, simplify the integration of TEM simulations with atomistic modeling techniques, such as density functional theory (DFT). By supporting both the multi-slice method and the PRISM algorithm, abTEM offers a flexible and accurate framework for simulating TEM images, including effects of chemical bonding. Its use of open-source libraries ensures high performance, rivaling that of traditionally faster languages like C and Fortran, while maintaining accessibility and ease of use.

2.6 Scripting in TEM

Automation and scripting in TEM become crucial for techniques such as HCDF imaging. These tools enable precise beam control, minimize human error, and enhance the consistency and reliability of imaging results. As the need for high-quality, statistically significant characterization at the micro and atomic scales continues to grow, the integration of sophisticated automation in electron microscopy becomes increasingly important. Similar advancements, as seen in cryo-electron microscopy [47–50], highlight the role of enhanced instrument control and automation in meeting the evolving demands of materials research. There is a growing interest in understanding and manipulating structures at the nanoscale, fueled by progress in materials informatics and the demand for reproducible imaging in electron microscopy. This need is hindered by predominantly manual workflows in data acquisition, which slow material development and limit experimental throughput.

Electron tomography, building on foundational methodologies [52–53] and bolstered by advancements in instrumentation [54–55], provides a vital step toward addressing these challenges. By enabling three-dimensional visualization of cellular architectures and macromolecular assemblies, tomography generates richer datasets that require more efficient collection, processing, and analysis methods. Consequently, integrating automated TEM scripting and enhanced microscope control becomes essential not only for capturing these complex 3D reconstructions reliably, but also for streamlining the broader materials characterization process—a necessity in a landscape where high-throughput, reproducible investigations increasingly drive scientific progress.

Key developments in tomography—founded on foundational methodologies [52–53] and bolstered by advancements in instrumentation—drive a surge in data acquisition efficiency [54–55]. Consequently, there is an increased need for more sophisticated TEM scripting and automation solutions to manage these larger, more complex datasets and ensure seamless microscope control. Notable techniques such as weighted back projection [56] are crucial for three-dimensional reconstructions. Automation remains a focal point, with studies addressing tracking and focusing techniques to minimize beam exposure for sensitive samples [57]. Innovations like the pre-calibration method [58] and the Z-prediction method [59] further streamline the tilt series acquisition process, enabling more reliable specimen positioning. Additionally, research into automated tomography software, such as that reported by Mastronarde [48], emphasizes adaptive prediction algorithms that enhance acquisition speed while maintaining reliability under less-than-ideal conditions.

2.6 Scripting in TEM

Most recent research focuses on developing a Universal Scripting Engine for TEM (USETEM), designed to integrate machine learning and automate data acquisition across different microscope platforms [97]. Next-generation microscopy requires innovative approaches to manage vast data volumes. An integrated data science platform is vital for translating complex datasets into actionable insights. The goal is to create adaptive microscopy that uses real-time data to guide experiments, leveraging machine learning to optimize imaging and predict outcomes [61].

2.6.1 TEM Scripting Components

TEM scripting provides an automated framework for controlling and coordinating microscope subsystems, including detectors and electron sources, through a stable, COM-based interface (Fig. 4). By functioning in single-thread mode, the component circumvents the complexities of event-driven or concurrent operations, thereby offering a simpler yet flexible environment for custom scripting. The Instrument object serves as the central access point, enabling navigation across various specialized capabilities—such as acquisition management, camera control, and electron source configurations—in a capability-driven design. Although the interface scope is deliberately constrained to maintain stability across software releases, support for a range of detectors (Ceta 1, Ceta 2, Falcon 3, Falcon 4) and emitter types (e.g., FEG, Cold FEG) ensures broad applicability in different experimental setups.

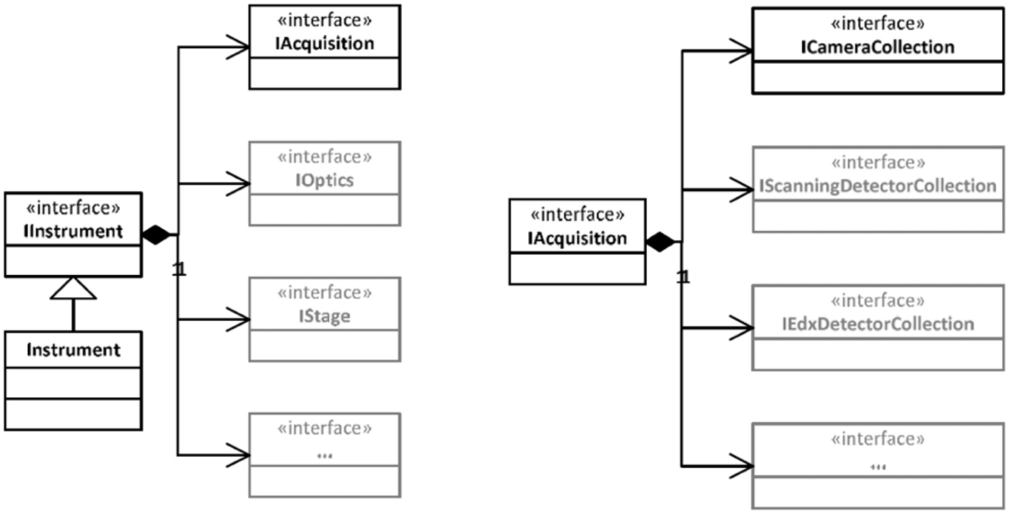

Figure 4: Diagram illustrating the Scripting components.

2.6.2 Software tools Comparison

This review examines prominent software tools—Leginon [47], SerialEM [48], Digital Micrograph (DM) [60], TOM Toolbox [49] and TEM Scripting [81]—in terms of their purpose, methods and structure, compatibility with different microscopes, and key advantages. These software platforms are integral to advancing automation and efficiency in electron microscopy, particularly in fields such as tomography and single-particle analysis.

Table 1: Comparison of Software Tools for Automated TEM Data Collection, Control, and Analysis.

Software Tool	Purpose	Method and Structure	Compatibility	Advantages
Leginon [47]	-Automates data collection -Handles goniometer issues -Drift Correction -Stage accuracy	-Modular node-based system -MySQL integration -Metadata storage -Session management	-FEI Tecnai T12 -FEI Polara F30	-Centralizes data management -Real-time tracking -Automatic stack generation -Increases throughput -Reduces downtime
SerialEM [48]	-Automates ET -Less manual -Handles goniometer issues -Drift correction -Holder Accuracy	-C++ (MFC) -COM interface -Custom plugins -Buffered stacks	-Tecnai F30 -Tecnai F20 -JEOL microscopes -TVIPS cameras -300 kV systems with energy filters and liquid-helium stages	-Position prediction -Minimizes tracking. -High accuracy -Supports large data
Digital Micrograph (DM) [60]	-Extends software functionality. -TEM Control -Enhances standard features.	-C++ - like scripting -Line-by-line execution	-Compatible with Windows (2000 and later). -Gatan cameras and spectrometers -JEOL TEMs -FEI microscopes with compatible hardware.	-Customization: No manufacturer dependence. -User-friendly for beginners.
TOM Toolbox [49]	-Integrates acquisition and analysis -low-dose imaging. -Specimen sensitivity	-MATLAB operated -COM-based interface	-FEI Tecnai -Gatan Imaging Filter -Linux -Irix -macOS -Windows	-Automates alignment -Real-time corrections -Open-source
TEM Scripting [81]	-Facilitates HCDF imaging	-Delphi scripting -High integration -Both functions within the same script.	-Thermo Fisher Talos F200X -Ceta	-Real-time synchronized control -No additional dependencies

	-Real-time microscope and image acquisition control. -Precise adjustments -Compatible with version discrepancies			-Tailors and validates

2.6.3 Limitations and challenge

A significant challenge is the risk of using these packages on Thermo Fisher Talos F200X series, which has not been specifically tested with these tools. The untested compatibility with Talos microscopes and Ceta detectors presents a high-risk factor, as unexpected behavior during testing can result in costly time delays or damage to the instrument. This concern is mitigated with Delphi scripting, which is tested and validated by the manufacturer [81] on these microscopes, reducing the likelihood of issues arising during use and thus minimizing risk.

Moreover, these software packages require the installation of specific dependencies, such as MATLAB, Digital Micrograph, or Python, alongside C++ handlers. These prerequisites introduce risks in terms of system stability and may cause complications on the microscope control computer, potentially affecting performance.

Lastly, the programming languages and methods used in these software tools are typically tailored to the specific microscopes on which they are tested, creating further challenges when adapting them to other microscope systems, such as the Talos F200X series. Ensuring compatibility requires time investment to investigate, modify, and test the functions and methods in these packages to match the Talos microscope's operation, further extending the time and complexity of the project.

2.6.4 Other Software packages

The software products developed directly by or in close collaboration with microscope or camera manufacturers—such as Hitachi 3D Tilt Image Acquisition, TEMography Recorder, Thermo Fisher Scientific Autoscript, and TVIPS EM-Tomo—are typically closed-source and distributed under commercial licenses. While these tools are highly specialized and tailored to the specific hardware, making them well-suited for advanced imaging applications, their proprietary nature and high costs pose significant financial challenges.

Chapter 3
HCDF Contrast Simulation Framework Design

3.1 Simulation Design Flowchart

Figure 5 presents a flow chart that outlines the principal stages of the simulation framework, from generating a uniformly distributed set of orientations to visualizing the resulting HCDF intensity. The process begins with the use of a MATLAB script equipped with the MTEX toolbox [95] to produce a grid of rotation matrices representing various crystallographic orientations. These matrices are then employed in a custom Python script that, together with the Atomic Simulation Environment (ASE) [92] and the abTEM package [93], creates and orthogonalizes atomic models of Mg. Minor adjustments—such as minimal strains—ensure that each model is suitably aligned with the Cartesian coordinates necessary for the multi-slice method.

Next, a specialized "slicethickness" Python code identifies an optimal slice thickness, preventing artifacts like wrap-around errors by ensuring that slices remain congruent with the natural atomic layers in each orientation. With the optimal slice thickness determined, the "ModelMaker" Python script repeats the orthogonalized unit cell along the z-axis to construct supercells for two designated sample thicknesses (200 Å and 500 Å). The complete atomic configurations are then exported in .xyz format, ready for simulation.

Subsequently, an automated workflow invokes the multi-slice simulation program—originally developed by Kirkland [94]—and a separate image generator tool to replicate the effects of lens aberrations and defocus. Within this modified setup, a virtual objective aperture is implemented to mimic hollow cone illumination [96]. Each run produces a 1024×1024-pixel intensity matrix normalized to the direct beam, which is subsequently imported into MATLAB. Here, the values are averaged and normalized, yielding a single quantitative measure of HCDF contrast for each orientation. Finally, these intensity values are visualized on an inverse pole figure

(IPF), where each orientation point is color-coded according to its normalized intensity. Additional graphical outputs, such as thickness-dependent intensity oscillation curves, may also be included to illustrate dynamical scattering trends.

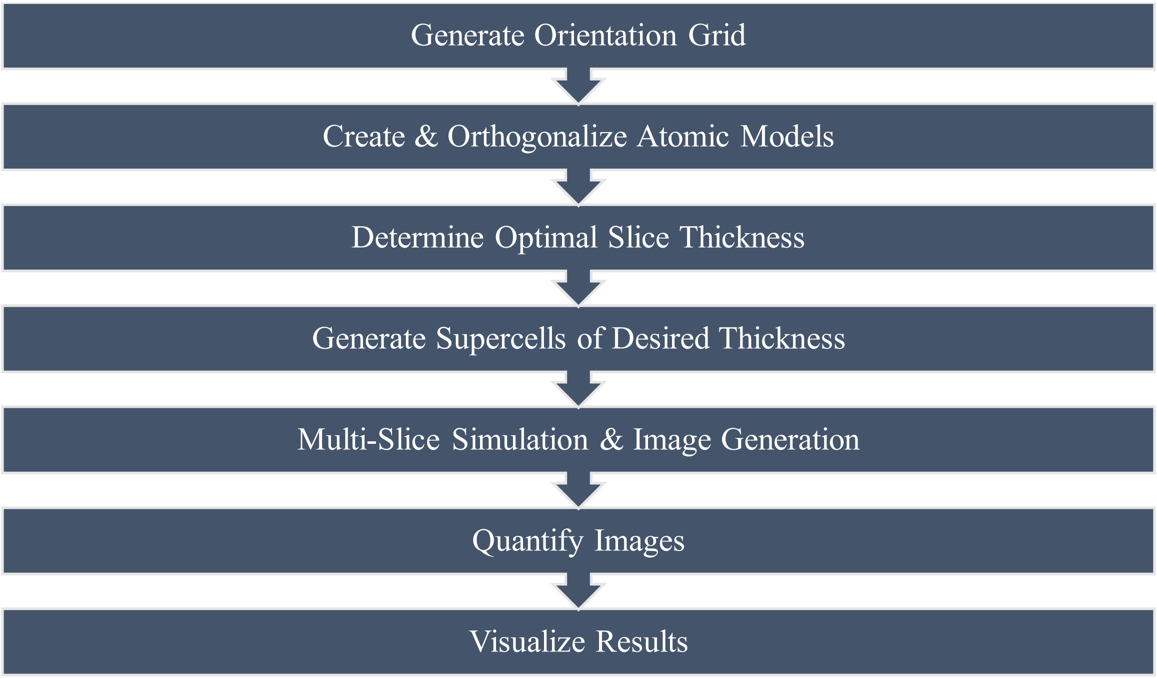

Figure 5: Flow Chart for HCDF Image Simulation Process.

3.2 Multi-Slice Simulation

The initial multi-slicing algorithm is created by Kirkland [94] and is intended to simulate how electrons travel through thin foils in a TEM. As illustrated in Figure 6, the thin foil is segmented into atomic layers along the z-axis, corresponding to the direction of electron beam transmission. By using this method, the intricate three-dimensional electron–matter interaction is simplified into a sequence of two-dimensional interactions that occur inside each atomic layer across the thickness of the sample. The two steps of the electron transmission process through the sample are the propagation via the vacuum between these layers and the transmission at the slicing layers. The program produces highly precise simulation results by matching the sample's atomic coordinates with the slicing layers.

3.2 Multi-Slice Simulation

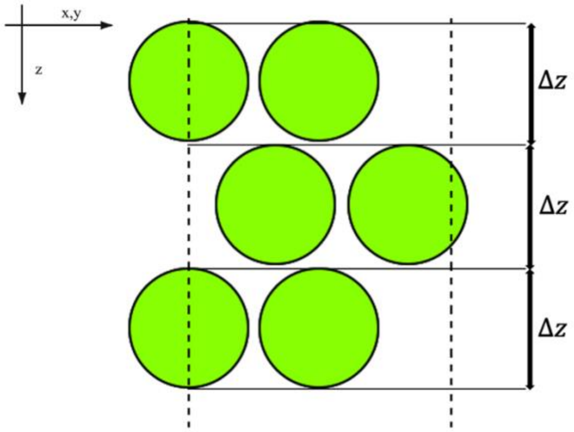

Figure 6: The standard multi-slice method models the specimen as a sequence of thin slices aligned perpendicular to the optical axis of the electron microscope, as illustrated here with three slices. Each slice Δz is made sufficiently thin to behave as a weak phase object, generally representing one atomic layer of the specimen. The optical axis of the microscope is oriented along the positive z-axis, and the slices must conform to periodic boundary conditions in the x and y directions to ensure computational accuracy.

In electron microscopy simulations using the multi-slice method, the specimen is modeled as a series of thin, rectangular slices (Δz) arranged perpendicular to the optical axis (z-axis), as depicted in Figure 6. To ensure an accurate depiction of the atomic potential, each slice is kept sufficiently thin to act as a weak phase object. The projected atomic potential for each slice is computed, and the electron wave function is propagated through it. After completing this computation for a slice, its atomic potential is discarded, and the simulation proceeds to the next slice.

This iterative procedure is repeated until the electron wave function propagates through all slices, ultimately reaching the specimen's exit surface. By compressing the atomic layers into a flat plane within each slice, the method preserves the natural periodicity of the structure. The resulting wave function at the specimen's exit surface is subsequently processed by the objective lens, which accounts for effects such as aberrations and defocus. This step produces a simulated image that closely resembles what would be captured in an actual electron microscope.

For HCDF imaging, which enhances contrast along specific crystallographic directions, the standard multi-slice approach is modified. A virtual objective aperture is introduced to simulate conical illumination conditions, enabling the algorithm to accommodate HCDF imaging [96]. This customization allows the electron beam to illuminate the specimen more effectively by covering a wider range of spatial frequencies, replicating the unique contrast patterns seen in HCDF images.

3.2 Multi-Slice Simulation

3.2.1 Generating uniformly distributed grid of orientations

This study requires the generation of a grid of orientations that uniformly covers the orientation space, which is a sphere and can be further reduced to one twelfth of a half-sphere considering the symmetry. Utilizing the commands from a MATLAB toolbox called "MTEX" [95], grids with defined resolution can be obtained. The resolution defines the angular step size, in degrees, between neighboring orientations in the grid. A smaller resolution means finer angular steps and thus more orientations, while a larger resolution means coarser steps and fewer orientations.

This process converts spherical coordinates to polar coordinates, calculates rotation angles as Euler angles, and applies a 'YZY' rotation sequence to align the crystal structure with the specimen's symmetry, storing the results as orientation matrices.

To test the generated data, a vector aligned with the Z-axis is defined, and the orientation matrices are applied to this vector after inversion. This step shows how the Z-axis orientation transforms according to the generated orientations. The pertinent script is represented in Appendix A.

3.2.2 Creating and orthogonalizing atomic models

After generating the equally spaced orientations, 790 rotation matrices are available as the output of the mentioned MATLAB script. Next, using the Python programming language and ASE (Atomic Simulation Environment) modules [92], atomic models in different orientations are created by a self-developed Python script. The multi-slicing algorithm operates with Cartesian coordinates, necessitating the use of an orthogonal unit cell for magnesium (Mg) rather than its native hexagonal lattice configuration. To achieve this, the unit cell is repeated multiple times until its lattice vectors approximate alignment with the three principal Cartesian axes. If this repetition process does not fully achieve orthogonality within a predefined limit, any residual misalignment is addressed by applying strain to the structure.

The orthogonalization procedure is performed using a method in the abTEM package [93], which transforms a non-orthogonal unit cell into an orthogonal one, necessary for multi-slice simulation algorithms that operate with Cartesian coordinates. The process starts by adjusting the atomic cell and ensuring atom positions are properly confined within it. If the origin is specified, the atoms are translated accordingly. Next, it aligns the cell with the specified plane if needed. To achieve an orthogonal structure, the original cell is repeated to approximate the principal Cartesian directions. If the cell doesn't already match the calculated orthogonal configuration, the process cuts and adjusts the repeated unit cell, applying transformations to ensure the atom positions and cell dimensions conform to an orthogonal layout. The result is a structure that aligns correctly for use in algorithms requiring orthogonal cells, with optional transformation details provided if requested.

Hexagonal cells can be transformed into an orthogonal configuration by doubling their size, allowing the conversion to occur without introducing any strain into the structure. However, this approach may not always be feasible. The necessary transformation can be obtained. Since the method for creating orthogonal cells introduces additional transformations beyond the initial rotation matrices, the final atomic models may deviate from the originally defined orientations. Therefore, it is necessary to identify rotation matrices that generate orthogonal cells without any extra transformation. This allows for the reporting of the actual rotation matrices corresponding to orthogonal atomic models with no additional adjustment. To achieve this, a custom Python script (Appendix B) is developed to generate these models and accurately report the associated rotation matrices.

3.2.3 Input File Design

The multi-slice simulation process begins by representing the specimen as a series of (x, y, z) coordinates, organized based on their depth along the z-axis. The simulation program requires atomic models in the .xyz file format. As represented in table 2, The .xyz file begins with a comment line describing the specimen, followed by a line specifying the unit cell dimensions in Angstroms. Each subsequent line contains an atom's atomic number, its coordinates, occupancy, and the standard deviation of its thermal displacement. The thermal displacements are randomly generated using a Gaussian distribution, ensuring different results in each run. Converting atomic models into this format is necessary for simulation.

Table 2: Acceptable atomic model .xyz file structure [94].

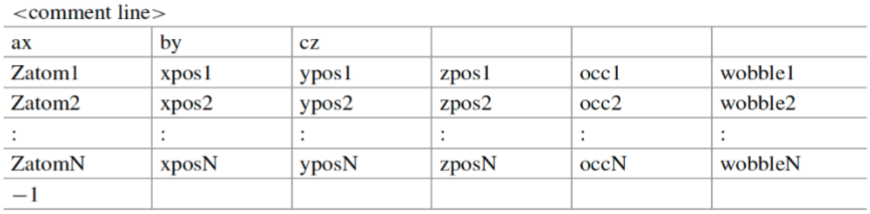

<comment line>

ax	by	cz			
Zatom1	xpos1	ypos1	zpos1	occ1	wobble1
Zatom2	xpos2	ypos2	zpos2	occ2	wobble2
:	:	:	:	:	:
ZatomN	xposN	yposN	zposN	occN	wobbleN
−1					

3.2.4 Slice Thickness

Accurate slicing is crucial to prevent computational artifacts, such as wrap-around errors [94] arising from improper boundary conditions in the x and y directions. Wrap-around errors occur when portions of the simulated wavefunction or potential erroneously reappear on the opposite side of the computational grid due to periodic boundary conditions. This can lead to inaccurate results by introducing artificial interactions between opposite edges of the sample, distorting the simulated image or data. Ensuring proper boundary conditions and appropriate slice thickness mitigates these errors, maintaining the integrity of the simulation. Aligning the slices with the specimen's natural atomic layers enhances simulation precision by reducing multi-slice errors and ensuring accurate reproduction of higher-order Laue Zones (HOLZ) in the diffraction pattern. Selecting an appropriate slice thickness, tailored to the atomic potential range, is essential for reliable results. Incorrect slice thickness can lead to false periodicities and artifacts, especially if it exceeds the specimen's natural periodicity.

To ensure that the slices are properly aligned with the atomic layers across various orientations, a Python code, “slicethickness,” is designed to calculate the most effective slice thickness. After extracting the lattice parameters—particularly focusing on the c parameter, which defines the unit cell dimension along the z-axis—a function checks whether the thickness divides the structure such that atom counts across slices remain consistent. The script calculates the possible range of slice numbers and tests various thicknesses within this range. The first thickness that meets the uniformity criteria is deemed optimal. The results for each model, including the optimum slice thickness, are stored in a list, converted into a Pandas DataFrame, and saved to an Excel file.

3.2.5 Generating Supercells

3.2 Multi-Slice Simulation

Once the orthogonalized atomic models in various orientations have been generated and the optimum slice thickness for each model is determined, the next step is to create supercells with the desired sample thicknesses—200 Å and 500 Å for this study. These supercells are formatted appropriately, as previously described, to serve as input files for the simulation program. The "ModelMaker" Python code, which is demonstrated in Appendix D, is designed to generate atomic models with specified sample thicknesses, either 200 Å or 500 Å, from existing input files. This process is repeated for all 790 atomic models, ensuring each is adjusted to the desired thickness.

To analyze intensity oscillations across different sample thicknesses, a modified script is used to generate supercells along a single zone axis. These atomic models are created with thicknesses varying from 10 Å to 790 Å.

3.2.6 Auto-Running Multi-Slice Simulation

After generating all the supercells in the required format using the previously described procedure, Python scripts are employed to automatically feed these models into the multi-slice simulation program and to automate the image creation process for the image generator program, similar to the multi-slice program. This automation significantly reduces the time and effort required for a task that would otherwise be tedious if done manually. The script iterates over each input file, executing simulation for each one, thereby automating the simulation process for all specified input files. The input values required by the multi-slice program are represented in Table 3.

Table 3: Important input values for the multi-slice simulation

Incident beam energy (keV)	Wavefunction size (pixels)	slice thickness (Å)	Temperature (K)
200	1024×1024	Between 1-2.54	298.15

Similarly, the automated process for the image creation program executes the image software using the bash shell within the Windows Subsystem for Linux (WSL), sequentially processing each input file. The input values required by the image program are represented in table 4.

3.2 Multi-Slice Simulation

Table 4: Important input values for the image program

Defocus (Å)	Spherical aberration Cs3-Cs5 (mm)	Minimum angle of the objective aperture (Milliradians)	Maximum angle of the objective aperture (Milliradians)
0	1.3-13	8.4	11.7

After generating all the images as outlined earlier, the next step involves quantifying these images for further analysis and comparison. To accurately represent the HCDF intensity, the logical approach is to average the intensity across the entire simulated image. To guarantee the comparability of all images, the averaged intensity is normalized against the intensity of the direct beam. The image program already outputs intensity normalized against the direct beam, so it is necessary to quantify this into arrays of intensity values. Given that the wavefunction size for this study is defined as 1024×1024 pixels for simulating each atomic model, an array of 1024×1024 normalized intensity values is obtained. These values can be read, averaged, and plotted using a custom MATLAB script. Another MATLAB code is responsible for plotting a color-coded inverse pole figure (IPF) based on previously calculated mean intensity values associated with different crystal orientations. Each orientation is plotted as a point in the IPF, with its color determined by the corresponding normalized intensity value.

Chapter 4
Automated Microscope Control for HCDF

4.1 Executing the Script

The process of compiling and running the TEM Scripting FP5451/00 application in Delphi 11.0, which is originally developed in Delphi 4.0 by the manufacturer, requires several steps, adjustments, and prerequisites due to significant differences between the two versions. These differences span changes in programming paradigms, data types, library structures, and graphical frameworks. Delphi 11.0 introduces the FireMonkey (FMX) framework, which replaces the older Visual Component Library (VCL) used in Delphi 4.0.

Before starting the migration, it is important to back up the original Delphi 4.0 project files to avoid data loss. Next, the existing project structure should be reviewed, including all forms, units, and components, to understand the scope of the necessary adjustments. One of the first technical tasks involves addressing compatibility issues by removing obsolete statements in the form files. Compiler warnings should be resolved by updating or removing the deprecated code. VCL components, such as TButton and TEdit, must be replaced with their FMX equivalents, and the properties of these components need to be adjusted to meet FMX requirements.

A key part of this process involves updating data types and library references. Obsolete data types used in the original Delphi 4.0 code must be replaced with their modern counterparts in Delphi 11.0. TColor used in older Delphi versions is replaced with the more advanced FMX.Colors in FMX, which requires updates to color manipulation functions.

The migration process also requires changes to the user interface (UI) design. Forms and layouts should be redesigned using the FMX form designer to ensure that the UI is responsive and compatible with modern platforms. In terms of performance, a key consideration is managing the connection to the microscope, which should be established in the FormCreate event. This connection is then verified for each tab in the PageControl component to avoid redundant connection attempts and streamline resource utilization.

The project also includes several reusable program units, such as GetVersion, which are intentionally kept separate from the main code to promote reusability across different applications. These units are updated to ensure compatibility with Delphi 11.0 and tested independently to verify functionality. In terms of version control, the program retrieves the version number dynamically from the executable file itself, using Windows API functions such as GetFileVersionInfo. This eliminates the need to manually synchronize multiple version numbers in the source code.

Another important aspect of this migration is event management. Delphi does not provide direct event handling, so the EventSinkImp utility by Binh Ly is used to generate event-handling code. This utility creates an event interface unit, which is compiled into a package and installed in the Delphi IDE. This process enables ActiveX event handling, which is crucial for controlling the microscope through custom events.

Overall, this migration process involves addressing key differences between Delphi 4.0 and Delphi 11.0, particularly in terms of data types, libraries, and UI frameworks.

4.1.1 Error Handling and Failure Scenarios

Several failure scenarios must be considered when using the TEM Scripting component:

1. **License Limitations**: If the requested feature is not licensed, the command fails, and an error message is provided.
2. **Parameter Inconsistencies**: If the client provides a set of acquisition parameters that are inconsistent, the operation fails. The system attempts to adjust parameters where possible, and the error message specifies which parameters are changed to resolve the inconsistency.
3. **Camera Availability**: Cameras can only be used for one acquisition at a time. If another client is using a camera, the Acquire() command fails. This also occurs if there is a physical conflict, such as another camera being inserted or a defect preventing camera insertion.

4. **Camera Offline**: If a camera is physically present but unavailable due to issues such as network disconnection or power loss, the Acquire() operation fails. The error message indicates the likely cause.
5. **Storage Server Issues**: If the Storage Server becomes temporarily unavailable, any acquisitions that require image downloads to the server (e.g., dose fractionation or EER-enabled acquisitions) fail.

4.2 Hollow Cone Scanning Parameters

In hollow cone scanning, the electron beam follows a path that traces an inverted cone. The “Arc Step” parameter defines the angular distance between successive beam positions, measured in degrees. For instance, a step size of 30 degrees results in a circular hollow cone scan consisting of 12 points (360/30), as shown in Figure 7. This parameter is user-controlled and can be adjusted between 0.1 and 359 degrees. In the microscope control software, the “Arc Step” is set via a TEdit box located in the “Illumination” section of the Delphi tab, allowing users to tailor the scanning process to specific needs.

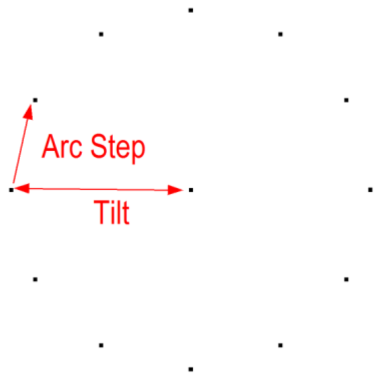

Figure 7: Schematic of a hollow cone scan showing how the Arc Step and Tilt parameters relate to the scan. Here the arc step is 30 degrees, and the tilt is 10 milliradians.

The scanning process operates through software using Ethernet communication, which significantly limits its speed compared to built-in hardware-based hollow cone scanning devices. The ultimate scanning speed depends on both the scan step size and the dwell time at each beam position. With optimal parameter selection, it is possible to achieve scan rates of several Hertz, though these rates remain slower than hardware-driven alternatives due to the inherent limitations of software-based control and network communication.

The “Tilt” parameter defines the angular displacement of the beam from the zero-tilt axis, with values measured in milliradians (mrads). For context, a typical Bragg reflection occurs at approximately 10 mrads (0.6 degrees). Extending the tilt scan to 50 mrads or beyond may prove beneficial in certain imaging applications. The allowable range for the “Tilt” parameter extends from 0 to 200 mrads, primarily due to the differential pumping aperture situated above the viewing chamber.

When using a diffraction contrast aperture for bright-field imaging, the maximum permissible tilt is constrained by the aperture’s acceptance angle, which varies depending on its size. For effective diffraction contrast imaging, tilts in the range of 9–12 mrads may be achievable with larger objective apertures.

In the case of hollow cone scanning, the “Tilt” parameter corresponds to the radius of the circular scanning pattern, where the tilt value represents the semi-angle. For example, a tilt semi-angle of 20 mrads results in a scanning pattern with a 20 mrad radius. In hollow cone scanning, the electron beam traces a circular trajectory, maintaining a constant tilt angle throughout the scan, ensuring uniformity in the angular displacement of the beam.

The “Dwell Time” parameter defines the duration (in seconds) that the electron beam remains at each scanning point. Since the scanning is executed via software, it operates significantly slower than hardware-based scanning methods. To mitigate these limitations, several optimization techniques can be employed. However, the use of extremely short dwell times—such as those below 0.01 seconds—is ineffective due to software constraints, which introduce processing overhead. Additionally, controlling threads becomes erratic when using very short dwell times. Consequently, the minimum dwell time is set to 0.01 seconds, with an upper limit of 20 seconds, applicable to all scanning modes except manual control.

System performance constraints also impact the actual dwell time. For instance, on certain systems such as ARM processors, the minimum effective dwell time is approximately 0.07 seconds, though this may vary depending on the specific hardware configuration. The primary bottleneck in reducing the dwell time further is the latency involved in adjusting the beam tilts, particularly due to the limitations of the software-driven system and the stabilization time of the microscope's deflector coils. Attempts to use dwell times shorter than 0.01 seconds can lead to instability in thread timing, further exacerbating performance issues.

To optimize scanning speed, the use of the shortest dwell time (0.01 seconds) combined with larger angular step sizes (e.g., 45 degrees) enables more rapid scanning, though the overall process remains slower compared to hardware-based solutions. Additionally, it is essential to synchronize camera acquisition times with the scanning period to ensure uniform sampling of reciprocal space during hollow cone scans. If the camera exposure times closely match the dwell times, undesired moiré patterns may emerge. Therefore, it is recommended to use camera exposure times significantly longer than the dwell times to avoid such effects and ensure consistent image quality.

The program allows users to adjust the step size and define the dwell time, which is automatically set to the minimum allowable value. Users can specify the tilt angle in milliradians (mrads). Once the step size is entered, the program calculates and displays the corresponding rotation time. This enables users to adjust the camera exposure time to synchronize with or be an integer multiple of the rotation time, ensuring proper image acquisition during the hollow cone scanning process. The user interface of the hollow cone tilting thread is displayed in Figure 8.

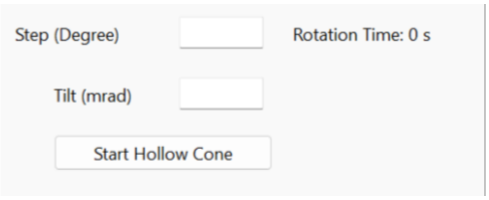

Figure 8: Interface of the hollow cone scanning thread

In the initial implementation of the hollow cone scanning process, an attempt is made to convert the Cartesian coordinates to polar coordinates for controlling the beam movement. The X and Y parameters in the scanning thread are handled separately, with the X parameter representing the radial distance (or tilt angle), and the Y parameter corresponding to the angular position in polar coordinates. This approach, however, introduces unnecessary complexity and leads to unintended beam trajectories. Specifically, the beam moves according to a pattern like that shown in Figure 9, where the Cartesian-to-polar conversion causes the beam to follow an incorrect path, deviating from the desired circular trajectory.

Upon further investigation, it becomes clear that this conversion step is not required. The microscope's internal control system already operates in a conical dark field mode, where the X parameter naturally corresponds to the tilt angle, and the Y parameter directly represents the angular position in polar coordinates. By eliminating the redundant conversion process, we streamline the scanning code, allowing the beam to follow the correct, smooth circular trajectory, as illustrated in Figure 7.

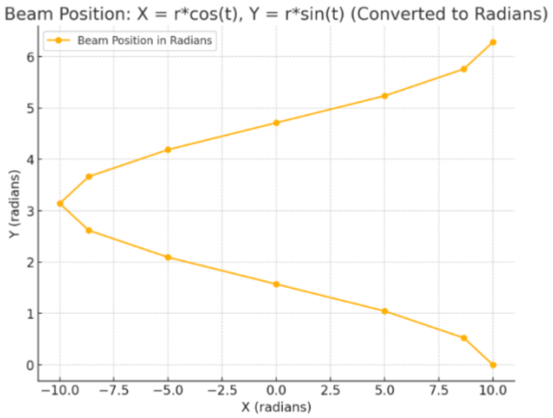

Figure 9: Beam trajectory pattern resulting from the inclusion of Cartesian-to-polar conversion in the script.

The program automates image acquisition during hollow cone scanning by synchronizing image capture with the scanning process based on user-defined exposure times. It supports tilt series acquisition, allowing users to specify desired tilt angles and corresponding exposure times; the program then captures images for each angle accordingly. The minimum exposure time must be at least equal to the complete rotation time determined by the chosen step size.

4.3 Experimental: Software Implementation

The initial material used is a Mg–Gd alloy containing 2.0 wt% Gd, selected due to the advantageous role of gadolinium in stabilizing grain boundaries (GBs). Rare-earth (RE) elements, such as Gd, tend to segregate at GBs, contributing to the preservation of the nanocrystalline structure. The ingot is wire-cut into cylindrical specimens measuring 10 mm in diameter and 1 mm in height. After cutting, each cylinder undergoes a series of mechanical polishing steps designed to reduce surface roughness and prepare the sample for electrochemical treatments. Polishing begins with sandpaper of 6 µm particle size, followed by 3 µm, 1 µm, and finally 0.5 µm. At each stage, a constant polishing rate is maintained to achieve a uniform and consistent surface finish. This mechanical polishing sequence effectively removes surface oxides, scratches, and residual deformations introduced by the wire-cutting process. Subsequently, the samples are punched into small circular disks, appropriately sized to fit into the TEM sample holder.

Following the sandpaper treatments, electro-polishing is carried out to further enhance the surface quality and remove any remaining surface imperfections. By applying an appropriate electrolyte and voltage, electro-polishing selectively dissolves higher areas on the surface, resulting in a smooth, mirror-like finish.

After electrochemical polishing, the specimens are loaded into a double-tilt sample holder in preparation for image acquisition. The double-tilt capability offers enhanced flexibility by allowing the specimen to be tilted about two orthogonal axes. This additional degree of freedom significantly facilitates the search for zone axes within the specimen, particularly when compared to single-tilt holders, because it enables precise adjustment of the crystal orientation relative to the electron beam.

Once the specimen is secured in the holder, the process begins with searching for zone axes by identifying suitable grains displaying well-defined diffraction patterns. These diffraction patterns are then indexed, which helps confirm the orientation of the grain and verifies that it aligns with the targeted zone axis. Because the crystallographic orientation critically influences the resulting diffraction conditions and, consequently, the contrast mechanisms in HCDF imaging, ensuring a precise match between the experimental geometry and the simulated conditions is paramount.

With the grain orientation determined and the zone axis established, the HCDF imaging process can commence. Different imaging conditions are used to acquire comprehensive datasets for subsequent intensity calculations. Of particular importance are the bright field (BF) images obtained in the absence of an objective aperture, as these images reveal mass-thickness contrast devoid of strong diffraction effects. These BF images constitute the primary source of data for thickness determination in the region of interest. A detailed explanation of the thickness measurement procedure is provided in the following section, wherein the intensity-based methods used to convert grayscale values into quantitative thickness information are discussed thoroughly.

4.3.1 Thickness Measurement

In low-magnification TEM micrographs, the contrast arises primarily from two sources: mass-thickness contrast (caused by incoherent elastic scattering, such as Rutherford scattering) and

diffraction contrast (resulting from coherent elastic scattering via Bragg diffraction) [97]. When crystals are not aligned along their zone axes, the contribution from diffraction contrast diminishes, making the image contrast primarily dependent on the sample's mass-thickness distribution.
For homogeneous materials, where the density remains constant throughout the sample (as is the case here), the image contrast can be directly related to the sample's thickness. This holds true when Bragg diffraction effects are minimized. The relationship between image contrast and sample thickness can be expressed by Equation below [143]:

$$C = \log_{10}(\frac{I_0}{I_{tr}}) = k.\frac{Z^x}{A} \quad \text{Eq 3}$$

Here:

- C represents the image contrast.
- I_0 is the electron intensity measured in areas without the specimen (background intensity).
- I_{tr} is the transmitted electron intensity measured after passing through the sample.
- k is a proportionality constant.
- Z and A are the atomic number and atomic weight of the material, respectively.
- x is an exponential coefficient dependent on the accelerating voltage.

Pozsgai's experimentally derived equation [143] is used to refine this approach, assuming consistent accelerating voltage and similar TEM illumination conditions.:

$$C = \log_{10}(\frac{I_0}{I_{tr}}) = \frac{1.44 \times 10^{-4}.\log_{10} e\,.\rho t Z^{1.96}}{A} \quad \text{Eq 4}$$

Here, ρ represents the density of the material, and t is the sample thickness. This equation is specifically tailored to include experimentally determined coefficients for 200 kV accelerating voltage. Using Equation above, we can rearrange to calculate the sample thickness (t):

$$t = \frac{C.A}{1.44 \times 10^{-4}.\log_{10} e\,.\rho.Z^{1.96}} \quad \text{Eq 5}$$

To ensure accurate thickness measurement using the Pozsgai method, it is important to minimize diffraction contrast by capturing TEM images without an objective aperture, as this reduces the influence of Bragg diffraction. The method assumes a homogeneous material with uniform density throughout the sample, making it suitable for cases where density variations are negligible. Additionally, it is crucial to maintain consistent TEM illumination and an accelerating voltage of 200 kV to align with Pozsgai's experimental conditions, ensuring reliable and accurate results.

4.3.2 Hollow Cone Scanning Software Operation

In acquiring HCDF images of Mg–Gd, the key objective is to ensure that the electron beam rotates at a selected tilt angle—within the 8.4–11.7 mrad aperture range—so that the relevant slip-plane reflections (basal {0001}, prismatic $\{10\bar{1}0\}$, and pyramidal $\{10\bar{1}1\}$) pass through the objective aperture. The aperture thus acts much like an annulus, collecting diffracted beams only within the designated semi-angle range. By design, these reflections dominate the contrast in Mg–Gd under HCDF conditions, enabling direct observation of orientation-dependent features.

In practice, the beam rotation can be performed either manually—by physically adjusting the microscope control knobs—or automatically—through a software interface integrated into the microscope control system. When using the software, the user begins by specifying the semi-angle of beam tilt (e.g., 10 mrad) and an “Arc Step” parameter (expressed in degrees), which defines the angular increment between beam positions as the electron beam traces the hollow cone. Once these parameters are set, the program calculates the rotation time required for a full 360-degree sweep. Because the beam circles around the optical axis, the camera exposure time must be synchronized so that each image integrates intensity over a complete rotation—or at least an integer multiple of complete rotations. This approach ensures that the image acquisition faithfully captures the entire diffraction ring rather than just portions of it, minimizing motion artifacts and enhancing contrast uniformity.

The software’s dwell time—the period during which the electron beam rests at each angular position—defaults to the minimum allowable value (typically 0.01 s). Shorter dwell times reduce overall scan duration, but they also need to be balanced against practical considerations, such as network latency and the microscope’s response time for tilt changes. Once the user sets an “Arc Step,” the total rotation time is automatically displayed on the interface.

By matching or setting the camera exposure time to a precise integer multiple of this rotation time, the software ensures that each captured frame corresponds either to exactly one—or multiple complete—circular sweeps of the hollow cone beam. This automated synchronization is crucial: if the camera exposure is shorter or longer than the rotation period by a non-integer fraction, partial arcs of the diffraction ring will be included in the integration window, creating potential banding or blurry artifacts in the final HCDF image.

When the hollow cone tilting routine is executed, the software simultaneously triggers the image acquisition routine according to the user-defined parameters. As the electron beam advances from one angular position to the next, the associated deflector coils in the microscope adjust in step, while the software tracks the elapsed time and dwell intervals to coordinate image capture. If the user wishes to operate at a somewhat slower rate for improved image quality or to collect more photons (especially in relatively low-intensity conditions), a longer exposure time is selected. The software automatically respects the integer multiple constraint so that each image still corresponds to an integral number of beam rotations.

In situations demanding more operator control, manual fine-tuning is possible. Operators may, for instance, set the tilt angle to slightly different values to center a specific reflection in the objective aperture or manually intervene if unexpected changes in specimen orientation occur during in-situ experiments (e.g., mechanical deformation tests). However, once the correct alignment is achieved, returning to the automated scanning mode generally provides more consistent and reproducible images because the software continuously regulates the rotation speed, dwell time, and exposure settings.

Figure 10 below is a flowchart illustrating how the hollow cone scanning software operates, from input of scanning parameters through image acquisition and final data output:

4.3 Experimental: Software Implementation

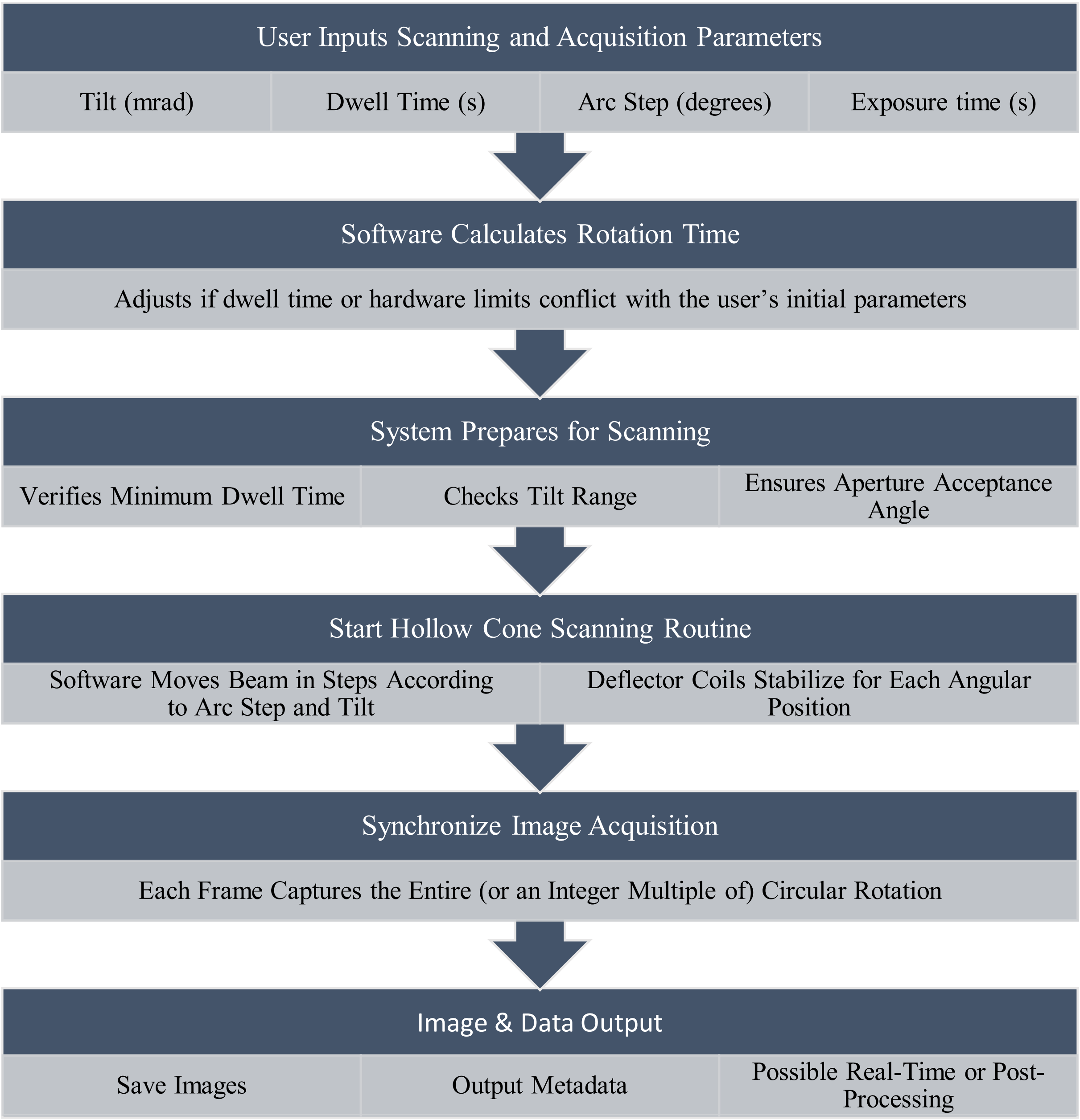

Figure 10: Flowchart summarizing the operational steps of the Hollow Cone Scanning Software.

Chapter 5
Results and Discussions

5.1 Uniform grid of orientation

The orientations evenly distributed in Euler space correspond to the atomic models used for multi-slice simulations, aligning with these specific orientations. A resolution of 1.5° for the orientations effectively covers the orientation space in a way that 790 orientations generated at this resolution provide a balanced compromise between coverage and computational feasibility for this study. As the resolution increases (i.e., smaller degree values), the number of orientations increases exponentially. Resolutions of 2°, 1.5°, 1°, and 0.5° generate 451, 790, 1757, and 6959 orientations, respectively.

For generating 790 atomic models, the process takes about 2 hours using the Python programming language on an Apple M1 processor. The true computational demand arises during the multi-slice simulation phase, which uses the generated models to simulate the exit wave and potentials. This step, performed on an Intel Core i7 processor, takes around 20 hours of processing time. If the resolution is increased to 1.0 degrees, it results in the generation of orientations more than doubling the number of models compared to a 1.5-degree resolution. This increase in the number of orientations likely causes the time required to generate these models to rise to approximately 5 hours, assuming a linear relationship in processing time. The multi-slice simulation could extend to 40–50 hours due to the increased computational load from the additional orientations.

At an even finer resolution of 0.5 degrees, the number of orientations generated jumps to nearly nine times the original number at 1.5 degrees. The initial generation of these models could take as long as 15–20 hours. The time required for the multi-slice simulations also increases dramatically, potentially exceeding 150 hours—or more than 6 days—to complete only for one value of sample thickness. The computational time variations in relation to resolution are illustrated in Figure 11.

5.1 Uniform grid of orientation

Figure 11-a illustrates 790 symmetrized orientations of the Z-axis within the fundamental region. Additionally, Figure 12-b presents 11 manually generated low-index zone axes distributed around the periphery of the inverse pole figure within the fundamental region, supplementing the missing data points in Figure 12-a.

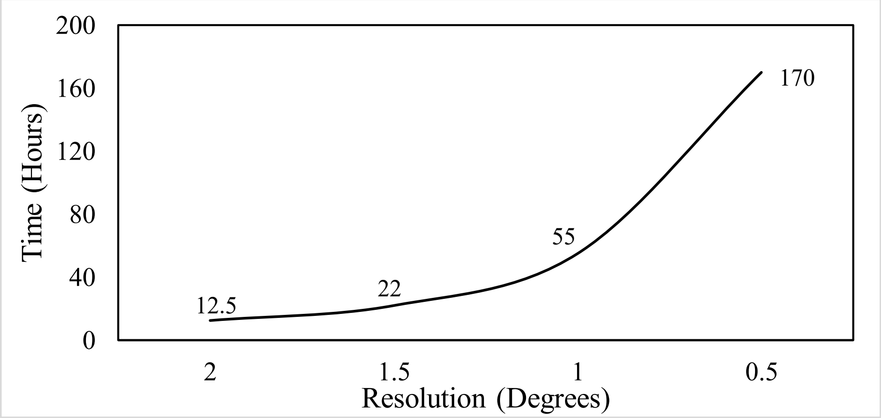

Figure 11: The trend of total processing time in relation to resolution on a personal computer

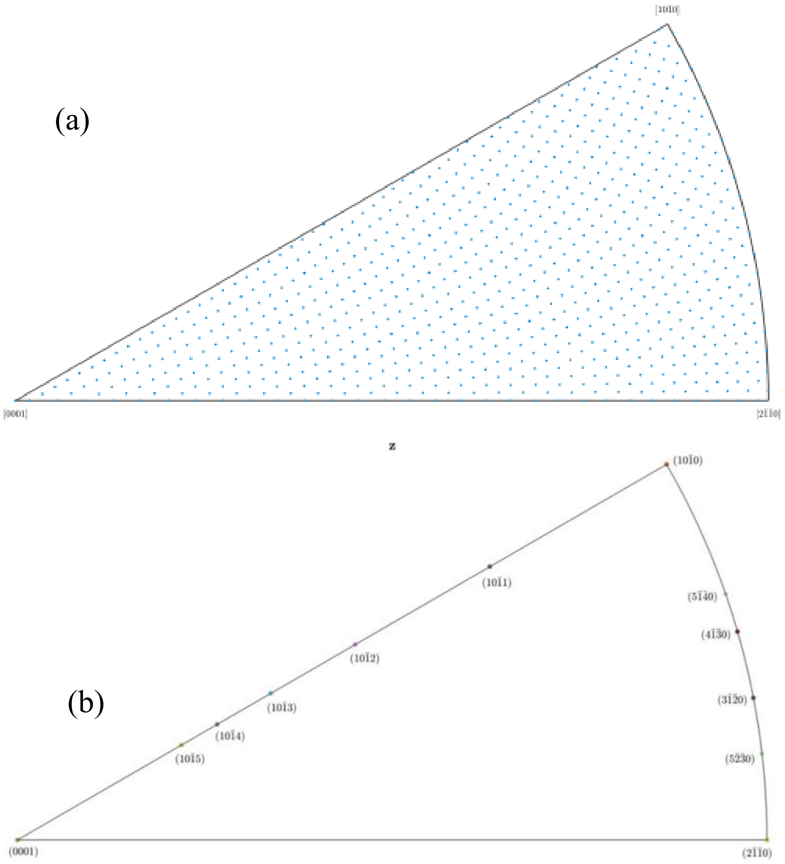

Figure 12: a) 790 Equally spaced orientations are generated by MATLAB – MTEX toolbox. b) Complementary orientations are selected along the periphery of the IPF.

5.2 Additional adjustments to orthogonalize models

The cell size can be multiplied to transform hexagonal cells into orthogonal ones. However, it is important to note that all computers use limited precision for floating-point numbers, which can introduce inevitable round-off errors during calculations. The program's runtime scales with the number of atoms in the simulation box, which increases by 27 times for each threefold expansion (3×3×3). For high-order zone axes with exceptionally large unit-cell dimensions, the required expansion can overwhelm computational resources, potentially leading to memory exhaustion before successfully determining all parameters *a*, *b*, and *c*.

Given this context, creating orthogonal supercells by merely multiplying the unit cell lattice parameters for high-order zone axes results in massive supercells. These supercells demand significant computational resources and lead to unreasonably long model creation and simulation times on a personal computer. To address this challenge while preserving the precision of the simulation, an alternative approach is employed: applying a very slight strain to the initial orientation of the cell. This minor adjustment aligns the cell with the Cartesian axes, allowing the simulation box to remain smaller and reducing both simulation and processing times. The resulting new orientations, as shown in Figure 13-b, deviate only negligibly from the original generated orientations. This approach provides a balanced solution that reduces computation time while maintaining high precision in the results.

The transformations are applied to achieve orthogonality along the $[10\bar{1}2]$ zone axis is detailed in table 5. The inverse pole figures display all 790 orientations before and after orthogonalization, demonstrated in figure 13, revealing that the transformations applied are minimal and nearly imperceptible, underscoring the effectiveness and precision of the orthogonalization procedure and the script used.

5.2 Additional adjustments to orthogonalize models

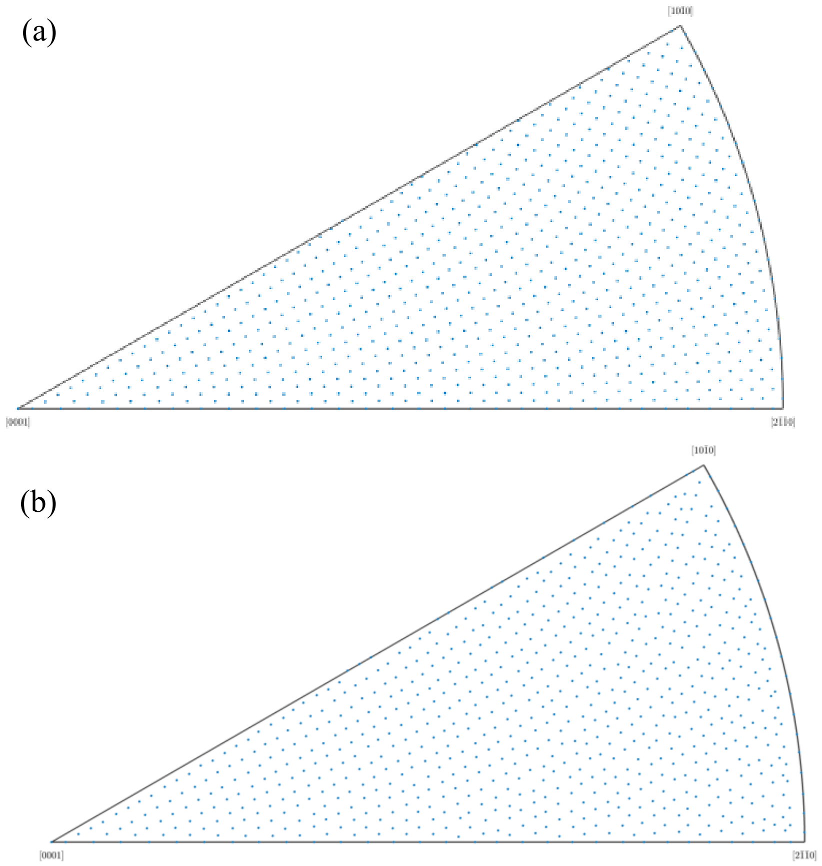

Figure 13: Inverse pole figure of 790 orientations a) Before orthogonalization. b) After orthogonalization.

As represented in Table 5 below, achieving the desired orthogonal cell along the $[10\,\bar{1}2]$ direction necessitates an additional -1.25° rotation around the Z-axis, which introduces both normal and shear strains in the crystal lattice. The normal strains, represented in percentage, include a slight tensile strain of 0.17% along the x-axis, indicating a minor expansion in that direction, and a small compressive strain of -0.024% along the y-axis, signifying a slight contraction. The z-axis remains unaffected with no strain observed, meaning the lattice structure in that direction is unchanged. The rotation also results in a shear strain of -2.19% in the xy-plane, reflecting the distortion between the x and y axes due to the rotation. No shear strains are observed in the xz or yz planes, indicating that the primary effect of the rotation is confined to the xy-plane.

These strains arise because the rotation alters the original lattice orientation, requiring adjustments in the lattice vectors to maintain orthogonality, leading to slight stretching and compression in the x and y directions and a change in the angle between them. This implies that, under the limitation of repeating the structure up to 10 times in any direction, the nearest periodic and orthogonal configuration achieved deviates from the initially specified rotation. The number of repetitions can be increased for greater precision. For instance, with a repetitions value of 20, the required transformation is just -0.114° around the Z-axis.

Table 5: Additional applied transformation to achieve an orthogonal cell.

Euler angles (degrees)	x = 0	y = 0	z = -1.25
Normal strains (percent)	x = 0.17	y = -0.02	z = 0
Shear strains (percent)	xy = -2.19	yz = 0	xz = 0

5.3 Effect of Slice Thickness

The multi-slice method involves projecting the atomic potential of a specimen along the z-axis, integrating it over the specimen's entire thickness. This projection is typically approximated by the potential within a single slice of thickness Δz. This approximation remains valid as long as Δz is sufficiently larger than the effective range of the atomic potential, which is approximately 1 Å for most materials. However, if Δz becomes smaller than this range, the atomic potential cannot be fully captured within such a thin slice, causing the approximation to fail. Consequently, selecting a slice thickness smaller than the atomic potential range introduces inaccuracies into the simulation, as the interactions between atoms are not adequately represented within each slice.

On the other hand, if the slice thickness is too large, the detailed variations in the wave function across the thickness of the material might be lost. The multi-slice method focuses on calculating the slowly varying component of the wave function as it propagates through the specimen. However, if the slice thickness Δz is too large, the method may overlook finer variations in the wave function. This can result in significant errors in the simulation, as critical details of the wave function's evolution through the specimen are inadequately resolved [94]. This, in turn, leads to inaccuracies in the final simulation results, especially when dealing with heavy atoms or when operating at lower electron acceleration voltages.

An optimum slice thickness for this study ensures that the multi-slice method remains both computationally efficient and accurate, providing reliable results. When performing multi-slice simulations, the atomic potential within each slice is integrated over a thickness, Δz. This integration is meant to capture the contribution of atomic potential from all atoms near the slice, typically within a range of about 3 Å. However, if the slice thickness is not well-aligned with the atomic periodicity, the atomic interactions of each slice may not be fully represented, potentially compromising the accuracy of the simulation.

Therefore, selecting a proper slice thickness is essential to balance accurate representation of atomic potentials and computational efficiency. To validate the accuracy of the slice thickness calculation algorithm, the number of atoms within each slice is manually calculated, and this process is repeated across the entire model thickness. The expectation is that the atom count within each slice remains consistent within a tolerance of ±1 atom, which is observed consistently until the final slice. No atoms are observed after the final slice, confirming the accuracy of the criteria. Furthermore, when the slice thickness is reduced to the scale of the vacuum length along the Mg [0001] zone axis, layers corresponding to the vacuum exhibit a zero-atom count, as expected.

Figure 14 illustrates the intensity oscillation curves as a function of increasing sample thickness, alongside the corresponding simulated HCDF image for a sample thickness of 210 Å and two different slice thicknesses.

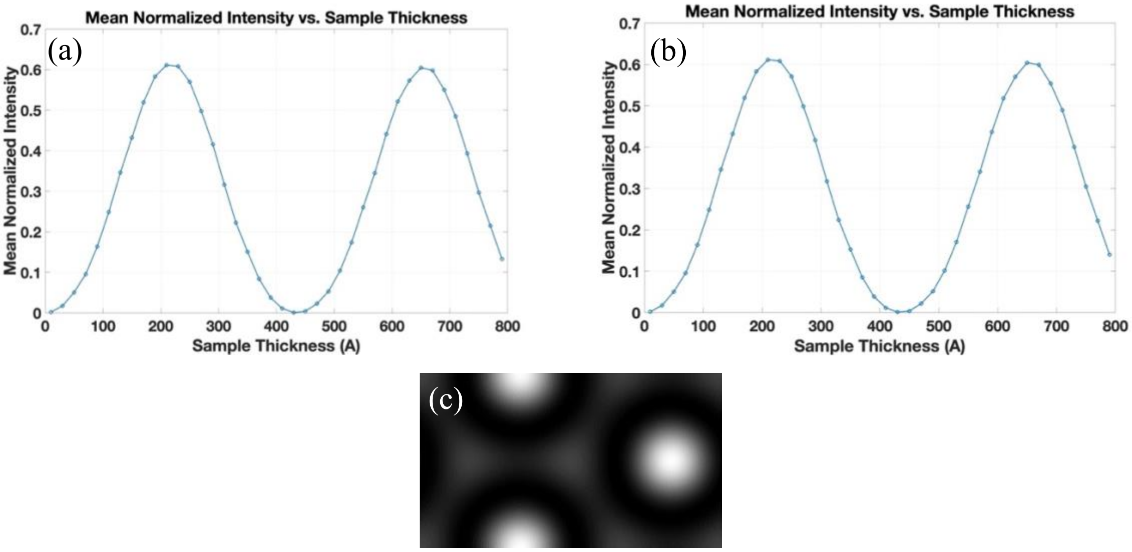

Figure 14: (a) Intensity oscillation with sample thickness for Mg [0001] zone axis. Slice thickness = 1 Å. Average intensity = 0.294370. (b) Intensity oscillation with sample thickness for Mg [0001] zone axis. Slice thickness = 2.5936 Å. Average intensity= 0.293869. (c) Corresponding simulated HCDF image with sample thickness 210 Å.

To validate the effectiveness of the calculated optimum slice thicknesses, in addition to the simulation conducted on Mg [0001] zone axis, multi-slice simulations are performed for an atomic model oriented approximately along the $[\bar{4}313]$ zone axis. Two slice thicknesses are tested: the minimum allowable by the simulation program (1Å) and the calculated optimum thickness of 2.5617 Å. The intensity oscillation curves as a function of sample thickness are presented in Figure 15 for both simulations. The simulation utilizing the calculated slice thickness demonstrates a marginally higher mean normalized intensity compared to the simulation with the minimum thickness. Adopting an optimally calculated slice thickness provides an effective compromise between numerical precision and computational speed in multi-slice simulations for this work. By tailoring the slice to the crystal's extinction distance rather than defaulting to a 1 Å increment, the total run-time can be reduced without sacrificing accuracy.

For magnesium oriented along the [0001] zone axis, the simulation is completed in 38 minutes 11 seconds when the slice thickness set to 2.5936 Å, compared with 43 minutes 27 seconds for a 1 Å slice—an improvement of roughly 12 percent. A similar benefit is observed for the Mg $[\bar{4}313]$ zone axis: optimization to a 2.5617 Å slice shortens the runtime from 54 minutes 07 seconds to 48 minutes 33 seconds, or about 10 percent.

When extended across the hundreds of orientations needed for comprehensive analyses, these efficiencies yield a substantial cumulative reduction in total processing time.

These results confirm the adequacy of the calculated optimum slice thickness values for this thesis.

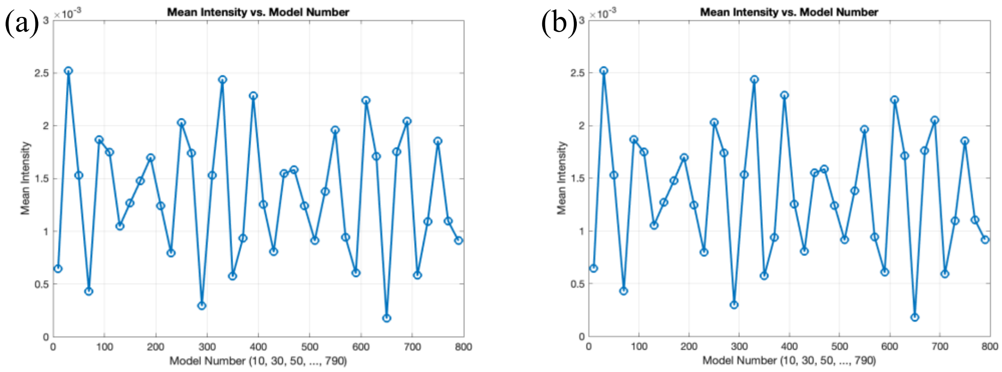

Figure 15: Intensity oscillation with sample thickness for Mg $[\bar{4}313]$ zone axis. (a) Slice thickness = 1Å, Average intensity 0.001344. (b) Slice thickness =2.5617Å, Average intensity 0.001348.

5.4 Intensity Oscillation

Multi-slice simulation results of selected zone axes in Mg: $[2\bar{1}\bar{1}0]$, $[\bar{1}100]$, $[\bar{1}102]$, $[\bar{2}201]$, $[1\bar{1}0\bar{1}]$, $[26\,\overline{13}\,\overline{13}\,\bar{3}]$ and $[\overline{28}\,20\,8\,3]$, are shown in Figures 16-18. These zone axes are selected to represent strong scattering events and their combinations, as shown in Table 6. By systematically varying the sample thickness from 0 Å to 800 Å and plotting the normalized intensity versus thickness, it becomes clear that the intensity of certain zone axes peaks around 200 Å and reaches a minimum near 500 Å. This behavior underpins the choice of using 200 Å and 500 Å thicknesses for subsequent simulations of 790 orientations, enabling the generation of contrast-based inverse pole figures (IPFs). By selecting these two key thickness values, it is possible to capture complementary points along the oscillation curve—one near a maximum and the other near a minimum—thus revealing a broader range of contrast variations across different orientations.

Table 6: Included g-vectors for each zone axis. PTCLAB software [98] is utilized to identify zone axes containing the relevant reflections.

Zone Axis	**Included Reflections**
$[2\bar{1}\bar{1}0]$	(0002), $(0\bar{1}11)$, $(0\bar{1}12)$
$[\bar{1}100]$	Only (0002)
$[\bar{1}102]$	Only $(0\bar{1}11)$
$[4\bar{2}\bar{2}3]$	Only $(0\bar{1}12)$
$[1\bar{1}0\bar{1}]$	Only $(0\bar{1}11)$ & $(0\bar{1}12)$
$[26\,\overline{13}\,\overline{13}\,\bar{3}]$	Only $(0\bar{1}11)$ & (0002)
$[\overline{28}\,20\,8\,3]$	Only $(0\bar{1}12)$ & (0002)

Comparing the three intensity oscillation curves for the $[\bar{1}100]$, $[\bar{1}102]$, and $[4\bar{2}\bar{2}3]$ zone axes in Mg (Figure 16) reveals the dynamical diffraction behaviors associated with each strong reflection (major g-vector): the $[\bar{1}100]$ orientation includes the (0002) reflection, the $[\bar{1}102]$ orientation includes the $(0\bar{1}11)$ reflection, and the $[4\bar{2}\bar{2}3]$ orientation includes the $(0\bar{1}12)$ reflection. For the $[\bar{1}100]$ orientation, the intensity rises from near-zero (≈0.0019 at 10 Å) to a distinct maximum surpassing 0.55 around ~210 Å in sample thickness, after which the intensity oscillates downward and partially recovers. This pattern reflects dynamical scattering, where multiple reflections within the crystal generate periodic intensity maxima and minima [94, 139]. Notably, the intensity is substantially higher than the other two orientations. Such high amplitude and strong peak intensity are consistent with the dominance of the basal planes in scattering. In contrast, the $[\bar{1}102]$ orientation contains the $(0\bar{1}11)$ reflection, intensity increases to a peak of about 0.31 at ~210 Å in sample thickness and then follows a similar periodic attenuation pattern. Although the overall oscillatory shape resembles that seen for the basal reflection, the maximum is considerably lower, and the mean intensity of 0.1584 is notably below that of the basal case. Non-basal reflections typically have a lower structure factor than the basal ones, leading to smaller diffraction intensities under the same thickness and electron energy conditions [94, 140]. Nonetheless, the presence of clear oscillations underscores that these planes still diffract efficiently at certain thicknesses, reflecting the multi-beam interference phenomena inherent in dynamical scattering [94]. The $[4\bar{2}\bar{2}3]$ orientation includes the $(0\bar{1}12)$ reflection. The intensity from 10 Å to 790 Å range from ≈0.0007 at the lowest thickness to peak around 0.18 at ~250 Å in sample thickness, then oscillate similarly to the other two cases. Despite the generally weaker scattering, the regular oscillatory pattern indicates that multiple scattering paths within the crystal continue to produce well-defined maxima and minima. When viewed side by side, each curve shows a broadly “wave-like” profile with thickness, consistent with known dynamical diffraction principles: electron beams penetrate the crystal, interfere constructively at certain thicknesses (leading to intensity maxima), and destructively at others (leading to intensity minima). However, the amplitude and overall average intensity vary according to the specific reflection. These results stem from each plane’s structure factor and geometric orientation in the HCP lattice.

5.4 Intensity Oscillation

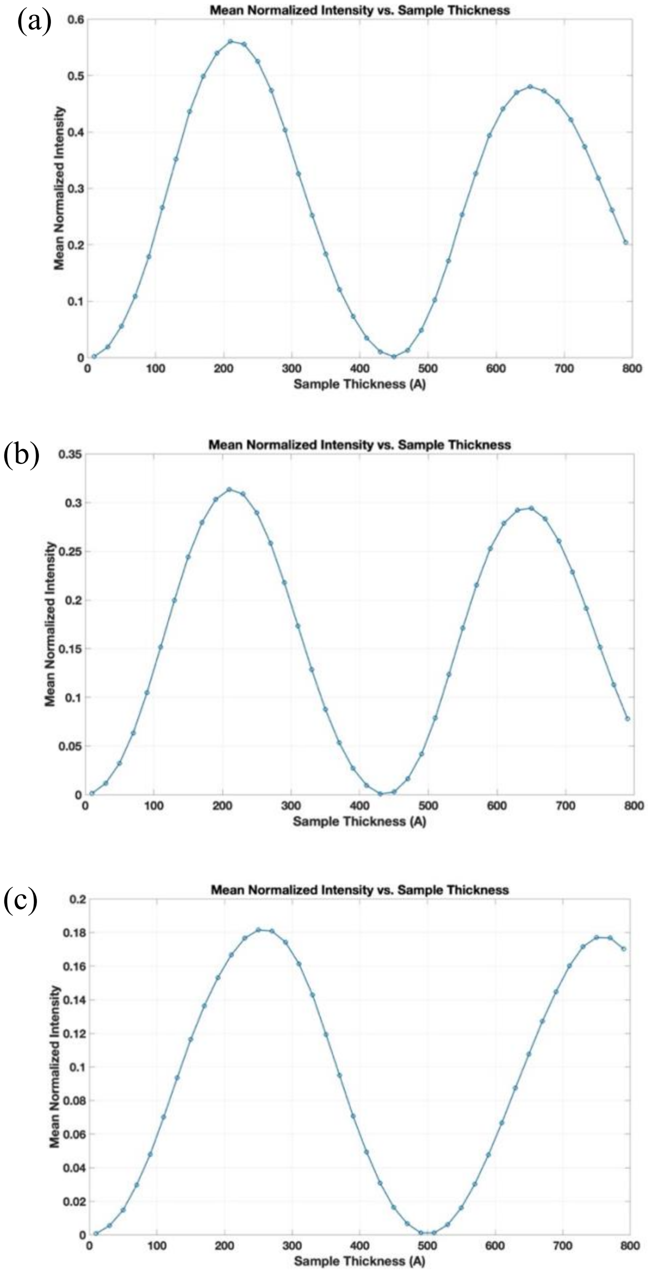

Figure 16: Intensity oscillation with sample thickness for Mg a) $[\bar{1}100]$ *zone axis b)* $[\bar{1}102]$ *zone axis c)* $[4\bar{2}\bar{2}3]$ *zone axis*

In figure17, unlike in the previously discussed cases where each zone axis contained only a single slip-plane g-vector, these new orientations simultaneously include two or even three major slip-plane reflections. Specifically, the $[2\ \bar{1}\bar{1}\ 0]$ zone axis encompasses (0002), $(0\bar{1}11)$, and $(0\bar{1}12)$; $[1\bar{1}0\bar{1}]$ zone axis contains $(0\bar{1}11)$ and $(0\bar{1}12)$; while $[26\ \overline{13}\ \overline{13}\ \bar{3}]$ zone axis includes $(0\bar{1}11)$ and (0002). Notably, the presence of multiple strongly diffracting planes can lead to more complex intensity distributions and differences compared to single-g-vector scenarios.

5.4 Intensity Oscillation

From a quantitative standpoint, $[2\,\bar{1}\bar{1}\,0]$ has a maximum of 0.6305 at ~150 Å in sample thickness, $[1\bar{1}0\bar{1}]$ has a maximum of 0.605 at ~225 Å in sample thickness, and $[26\;\overline{13}\;\overline{13}\;\bar{3}]$ has notably lower maximum of 0.147 at ~250 Å in sample thickness. The first two cases exhibit distinctly higher intensities while the third case remains relatively weak despite including (0002) and $(0\bar{1}11)$ reflections. The high-order zone axis of the third one likely disperses intensity into other reflections such as higher-order Laue zone (HOLZ) reflections, thus diminishing the net intensity associated with these two reflections [94, 138, 139]. The involvement of multiple g-vectors fosters more multi-beam interactions, producing broad, high-amplitude peaks and a complex interference pattern. As a result, $[2\bar{1}\bar{1}0]$ (Figure 17-a) has the oscillation period of ~295 Å while $[1\bar{1}0\bar{1}]$ (Figure 17-b) displays oscillation period of ~470 Å. Contrasting these multi-g-vector results with the earlier single-g-vector analyses illuminates the significant impact of reflection multiplicity on both the amplitude and periodicity of the thickness fringes. Single-plane excitations yield relatively "clean" oscillations primarily governed by one extinction distance; adding two or three slip-plane reflections leads to more nuanced interactions among the beams. Interference conditions can overlap or offset each other, generating a broader plateau of elevated intensity or multiple smaller peaks over the thickness range. Consequently, the average intensities can be higher or lower than single-plane scenarios depending on whether constructive multi-beam coupling dominates (as in $[1\bar{1}0\bar{1}]$) or if a high-order zone axis redirects scattering into other HOLZ reflections, as in $[26\;\overline{13}\;\overline{13}\;\bar{3}]$.

5.4 Intensity Oscillation

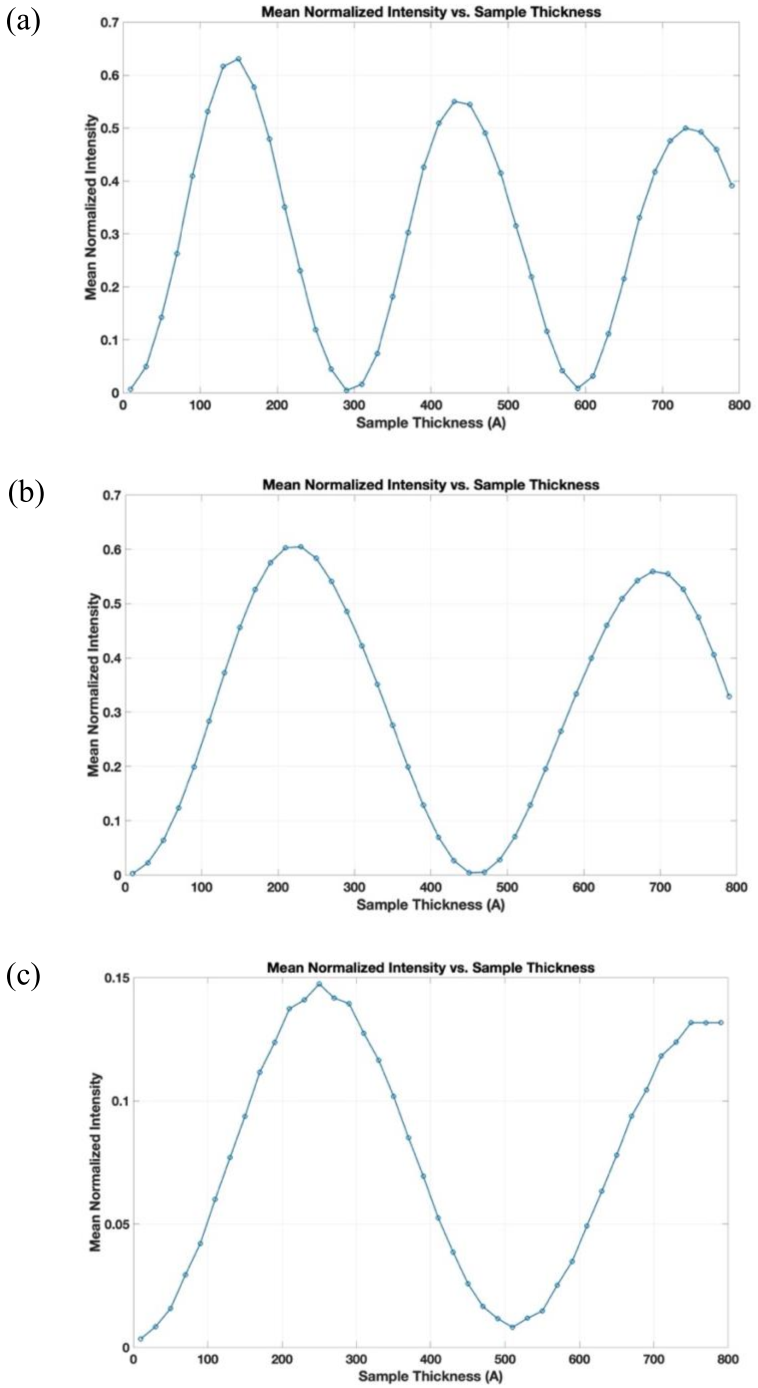

Figure 17: Intensity oscillation with sample thickness for Mg a) $[2\bar{1}\bar{1}0]$ *zone axis b)* $[1\bar{1}0\bar{1}]$ *zone axis c)* $[26\ \overline{13}\ \overline{13}\ \bar{3}]$ *zone axis.*

As demonstrated in figure 18, the $[\overline{28}\ 20\ 8\ 3]$ zone axis in Mg, which includes only the $(0\bar{1}12)$ and (0002) g-vectors, exhibits notably low intensity values—on the order of 10^{-4} to 10^{-3}—even though it encompasses two major slip planes. This high-order $[\overline{28}\ 20\ 8\ 3]$ orientation channels some of the scattered beams into more complex reciprocal-lattice rods. As a result, each individual g-vector receives only a fraction of the total electron flux at any given thickness. The oscillation curve for this orientation shows an irregular pattern with small values that hover around 10^{-4}. Such high-order orientations can display more erratic fringe spacing due to the interplay of multiple beams entering and exiting resonance. As a result, the curve looks “noisy” or “scattered” around a narrow band of values, rarely rising into the 0.01–0.1 range that is commonly seen in simpler cases.

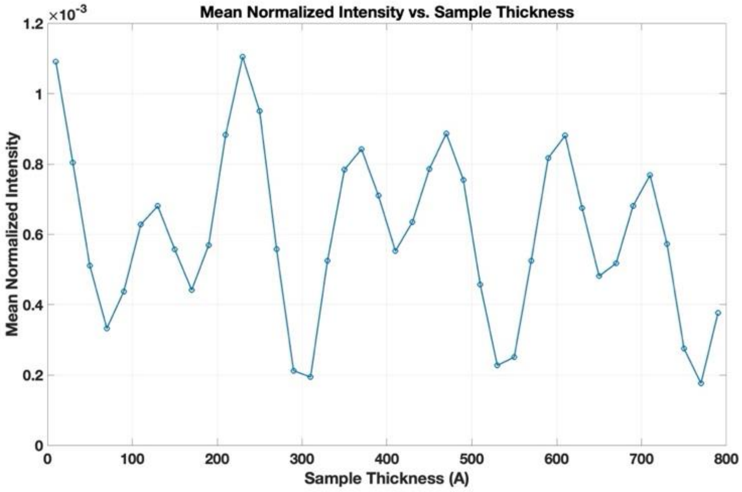

Figure 18*: Intensity oscillation with sample thickness for Mg* $[\overline{28}\ 20\ 8\ 3]$ *zone axis.*

5.5 Hollow Cone Contrast on IPFs

A comprehensive examination of the contrast–orientation relationship in HCDF imaging is presented through a systematic evaluation of 790 unique crystallographic orientations. For each orientation, the intensity arising from zone axes aligned with slip planes—those known to produce strong Bragg reflections—is analyzed using multi-slice simulations. Specifically, three principal slip planes are considered, and the presence of their corresponding reciprocal lattice vectors (g-vectors) within the zone axis cone is found to significantly enhance the observed diffraction contrast. This enhancement is manifested as heightened intensity values, which often exceed 0.1 for zone axes containing at least one of these slip plane g-vectors, confirming that orientations facilitating Bragg diffraction through these planes yield substantially stronger contrast signals.

In contrast, zone axes that do not contain any of the relevant g-vectors corresponding to the three identified slip planes—such as the $[\bar{4}313]$ zone axis—exhibit negligible intensities, on the order of ~0.002 or lower, even when evaluated at sample thicknesses up to approximately 500 Å. To illustrate these findings, color-coded inverse pole figures (IPFs) are constructed using stereographic projection [97], effectively mapping each orientation's calculated intensity. In these visualizations, orientations devoid of slip-plane g-vectors are depicted as near-black dark blue data points. For orientations that do include slip-plane g-vectors, the IPF exhibits distinctly more intense coloration, reflecting the higher diffraction intensities that these configurations produce.

To verify the accuracy of the intensity values associated with the orientations located along the edges of the inverse pole figure (IPF), as illustrated in Figure 12-b, a series of complementary multi-slice simulations are conducted. These orientations, while highly similar to those represented in the original IPF, are not included in the initial dataset and thus must be generated and analyzed manually. This validation exercise demonstrates consistency in intensity values between the manually generated orientations and their closest pre-existing neighbors on the IPF. This close agreement not only reaffirms the accuracy and stability of the multi-slice simulation approach but also substantiates the underlying trend that the intensity distribution remains coherent across the IPF's orientation space, extending all the way to its boundaries.

To further validate and elucidate the observed intensity behaviors, a second series of simulations is performed under analogous conditions using the same set of 790 orientations. In this case, the sample thickness is increased to 500 Å. As per the well-documented intensity oscillation phenomena in electron diffraction, increasing the sample thickness shifts many orientations toward a region of lower average intensity along the oscillation curve. Consequently, while the same trend of higher intensity for zone axes containing slip-plane g-vectors is preserved, the absolute intensities are generally reduced compared to the 200 Å simulations. The maximum intensity observed for these thicker samples is approximately 0.1, significantly lower than the maximum of about 0.6 measured at 200 Å, yet still substantially stronger than the near-zero intensities for orientations lacking the relevant slip-plane g-vectors.

These comprehensive simulations, encompassing a wide array of orientations, confirm that the diffraction intensity distribution within HCDF is highly sensitive to both crystal orientation and sample thickness. Orientations conducive to Bragg diffraction through slip-plane g-vectors produce a pronounced intensity signature, which remains consistent despite variations in thickness-induced intensity oscillations.

5.5 Hollow Cone Contrast on IPFs

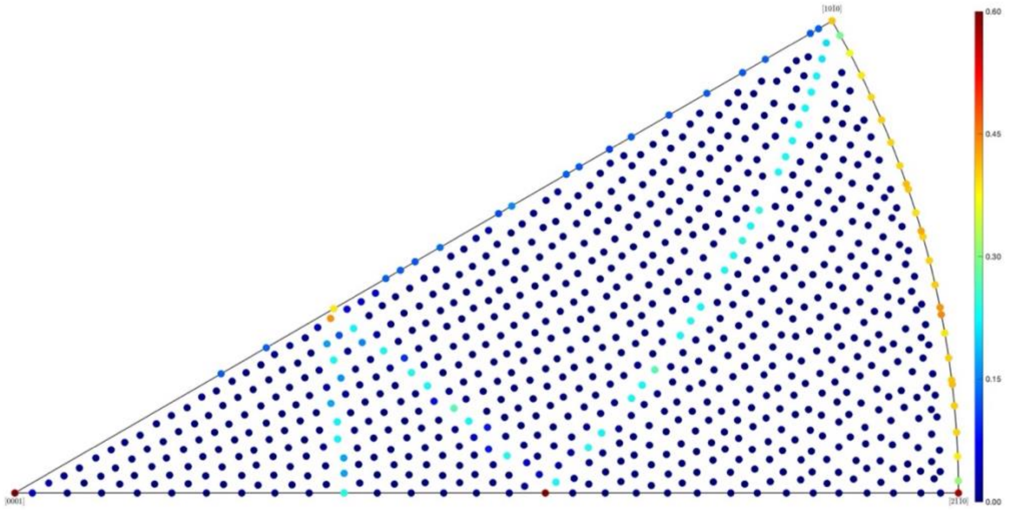

Figure 19: IPF color-coded is based on the calculated intensity of each zone axis, sample thickness is held constant at 200Å for all 801 data point in the plot.

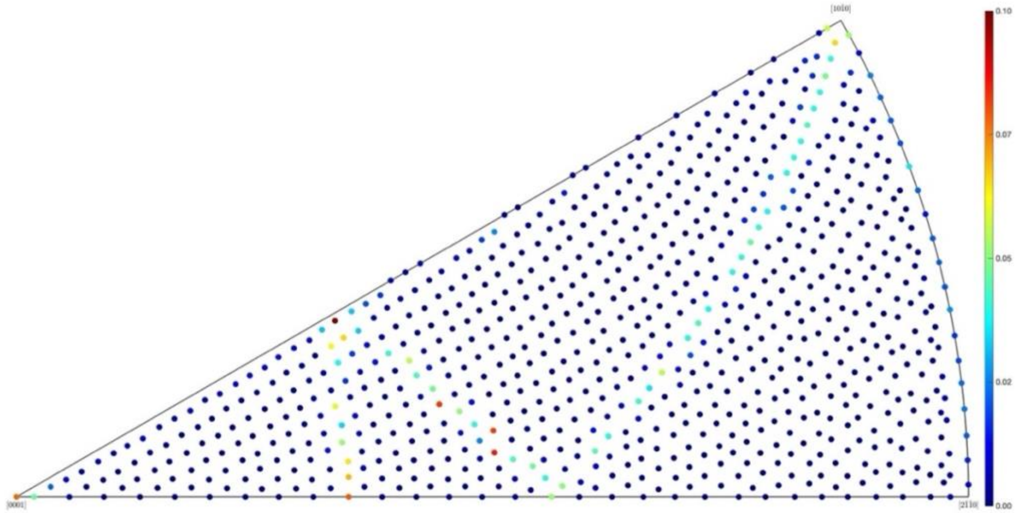

Figure 20: IPF color-coded is based on the calculated intensity of each zone axis, sample thickness is held constant at 500Å for all 790 data point in the plot.

5.6 Experimental Results

Five different grains are identified, and their corresponding diffraction patterns are recorded, as shown in a typical diffraction in Figure 21.

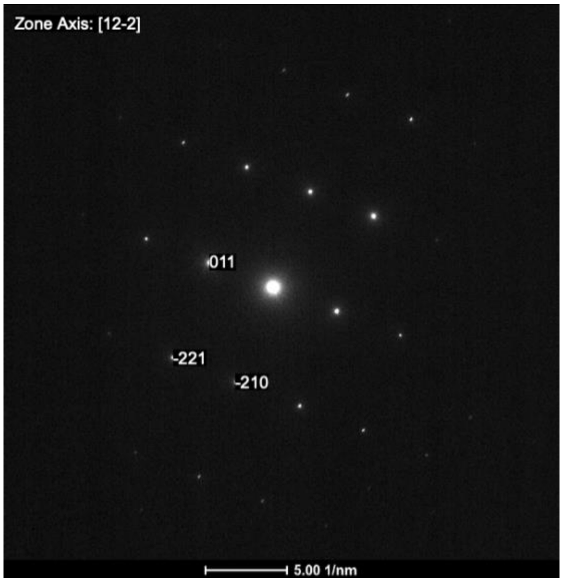

Figure 21: Diffraction pattern of G2 corresponding to $[01\bar{1}\bar{2}]$ *zone axis.*

Next, bright field images without the objective aperture are acquired to determine the thickness of each selected region. As shown in figure 22, these images are taken at the specimen edge so that they encompass both the region of interest within the specimen and a portion of blank area, which is used to measure the beam intensity according to the procedure described in Section 4.3.

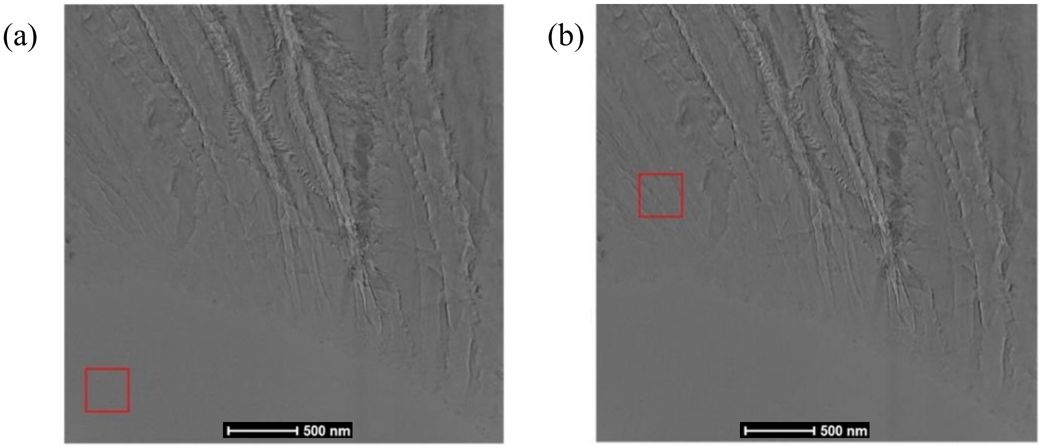

Figure 22: BF image of G2 without objective aperture (a) Selected region in the blank area to calculate mean incident intensity I_0*, and (b) selected region on the specimen to calculate mean transmitted intensity* I_{tr}*.*

5.6 Experimental Results

In line with the recommendations provided in ref. [143], images are acquired without using an objective aperture, thereby mitigating potential errors originating from strong diffraction contrast. Practically, the transmitted intensity I_{tr} are measured by averaging the intensity over the region of interest within the specimen, and the incident intensity I_0 are obtained by averaging the blank area outside the specimen edge. By substituting these averaged intensities into Equation, the thickness of each grain are calculated. This method ensures that any strong Bragg diffraction is 'evened out' by considering an average value rather than a single pixel or small subset of pixels.

The calculated values for G2 ($[01\bar{1}\bar{2}]$ zone axis) corresponding to area shown in Figure 22-b are as:

- I_0 = 98617.4456
- I_{tr} = 97623.4963
- x=1.96 (Depending on the accelerating voltage)
- t = 50.32 nm

The mean normalized HCDF intensity is determined by analyzing the exact same region of interest (ROI) previously used for thickness evaluation in the aperture-free images, to ensure consistency. First, the relevant ROI in each HCDF image is identified, and its corresponding raw intensity data are extracted from the proprietary FEI .ser file format using MATLAB scripts. This .ser format preserves the native electron microscope image data, thus allowing direct access to the unprocessed grayscale values.

Next, the necessary metadata (acquisition time and binning) are retrieved from the .emi files generated by the microscope. These parameters are then incorporated into the calculation to correct for any variations in detector exposure. Specifically, the mean intensity value of the specimen area is divided by the product of the binning and the acquisition time to yield a time- and binning-corrected intensity. The same correction is applied to the previously measured blank region used in the thickness calculations.

Finally, to obtain the mean normalized HCDF intensity, the corrected mean intensity of the specimen ROI is divided by the corrected blank-region intensity. This ratio provides a direct measure of normalized contrast that can be compared reliably to simulation results or to other experimental conditions.

5.6 Experimental Results

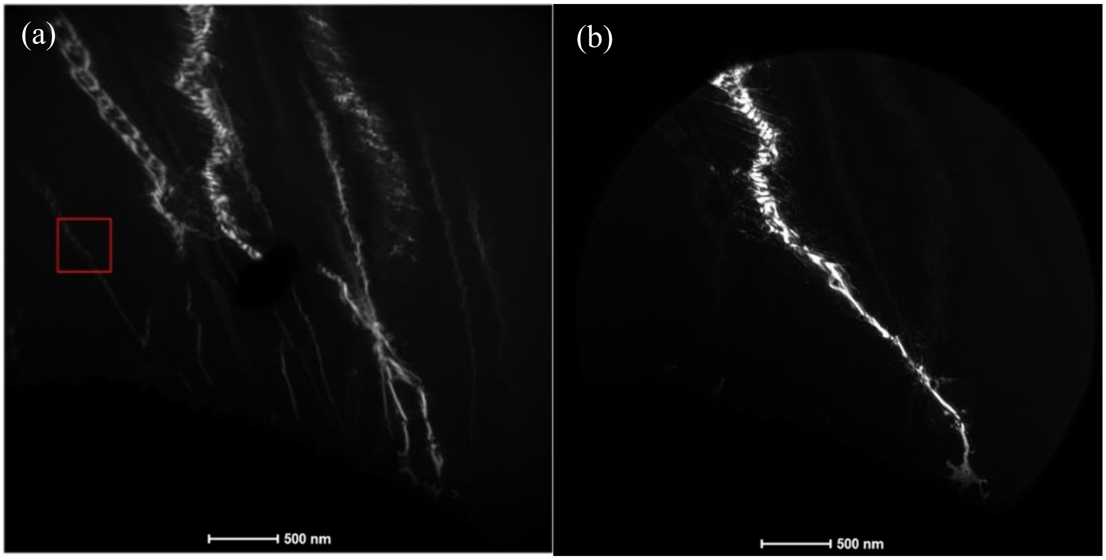

Figure 23: (a) Hollow Cone Dark field image of G2 using scattering angle of reflection (011), (b) Conventional Dark field image of G2 corresponding to reflection (011).

The average normalized HCDF intensity of G2 within the region outlined by the red square in Figure 23-a is calculated as follows:

- I_0 = 98617.4456
- I_0 Exposure time = 4s, Binning = 4
- I_{Sq} = 2331.5748
- I_{Sq} Exposure time = 8s, Binning = 4
- $I_{HCDF,G2} = 0.0118$

In Figure 23-a, the HCDF image displays substantially more bright parts compared to the conventional DF image shown in Figure 23-b. This difference arises because conventional DF imaging selects only a g-vector (011) for image formation, thereby discarding most of the diffracted electrons. In practice, this means that only grains oriented within the specific diffraction segment selected by the objective aperture contribute to image contrast. As a result, other reflections—even those that could be contributing useful signal on other parts of the same scattering angle—are missed and remain invisible in the conventional DF image. Furthermore, whenever the grain orientation changes such that its diffraction spot shifts outside the chosen aperture segment, it is erroneously treated as if it has rotated away from the "edge-on" condition and simply disappears from the DF image.

5.6 Experimental Results

Table 7 below presents the normalized average HCDF intensities measured from the five experimentally obtained zone axes, along with their corresponding thickness values. All this data is acquired using the same procedure described earlier for G2, calculating both thickness and intensities.

Table 7: Experimentally Determined Mean Normalized Intensity and Corresponding Thickness Values for Each Zone Axis.

Zone Axis	**G1 =** $[\mathbf{01\bar{1}1}]$	**G2 =** $[\mathbf{01\bar{1}\bar{2}}]$	**G3 =** $[\mathbf{11\bar{2}\bar{3}}]$	**G4 =** $[\mathbf{01\bar{1}\bar{1}}]$	**G5 =** $[\mathbf{\bar{4}\bar{1}56}]$
IHCDF	0.0608	0.0118	0.0518	0.0657	0.0539
Thickness (nm)	238.61	50.32	55.31	51.8	126.77

For an accurate comparison with the experimental data, multi-slice simulations are performed for the specific zone axes corresponding to the experimental images in table 7. In addition, the simulations are conducted over a thickness range extending 50 nm above and below the initially determined thickness. This extended range allows for potential inaccuracies in the measured thickness, which may arise from local variations in sample preparation or residual diffraction effects, as discussed previously. Subsequently, the experimentally derived mean normalized intensities are plotted against the sample thickness in figure 24. This comparison enables a direct assessment of how well the measured data fits within the theoretical predictions across the selected thickness range.

5.6 Experimental Results

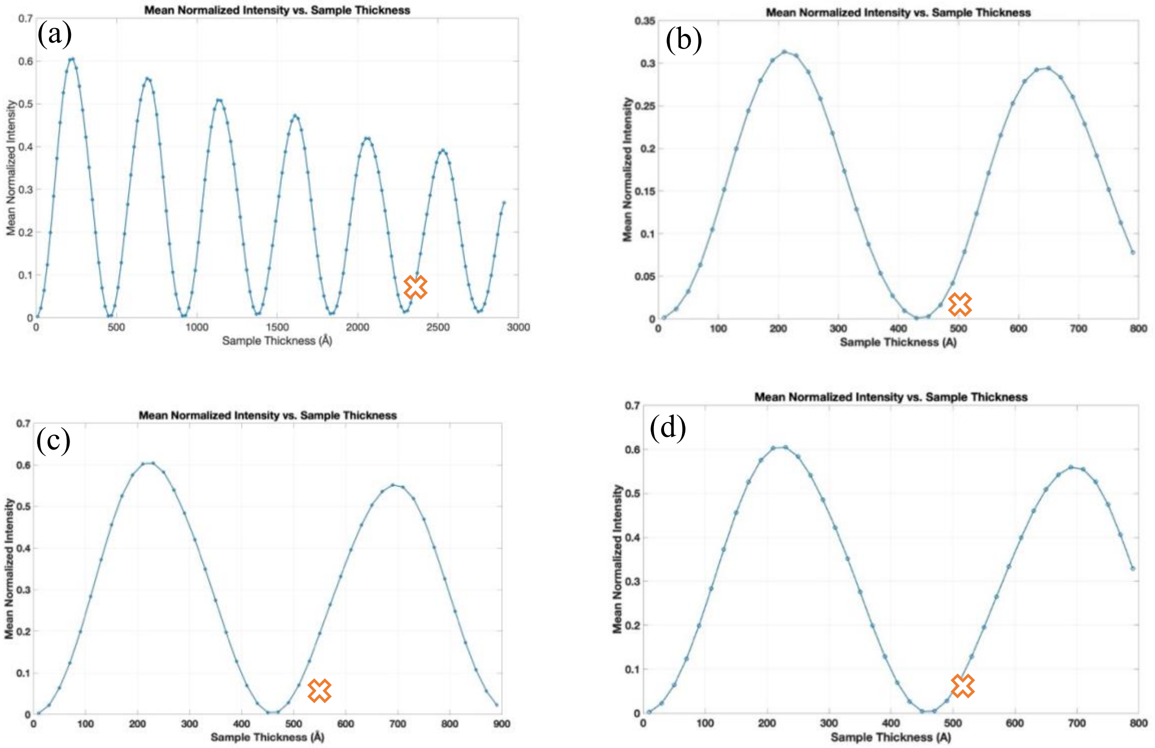

Figure 24: Intensity Oscillation with sample thickness for (a) G1 = [01$\bar{1}$1], *(b) G2 =* [01$\bar{1}\bar{2}$], *(c) G3 =* [11$\bar{2}\bar{3}$], *and (d) G4 =* [01$\bar{1}\bar{1}$]. *Blue curves are simulation data and red crosses are experimental results from table 7.*

Figure 24 presents the results of the multi-slice simulations carried out using the same parameters employed in the experimental images, along with experimental results from Table 7 for comparison. Simulation results show good agreement with experimental observations. For instance, in the case of G1, an experimental intensity of approximately 0.0608 is measured at a thickness of 238.61 nm. Referring to Figure 24(a), the simulated intensity is around 0.06 at 230 nm and about 0.05 at 240 nm—both of which closely bracket the experimentally observed value. A similar level of consistency is observed for G2, G3, and G4, further confirming that the simulation approach provides results that are in close accordance with the measured intensities. These findings underscore the reliability of the simulation methodology and validate its utility for predicting intensities over a range of thicknesses in this study.

For G5, the experimentally measured intensity is 0.0539 at a thickness of 126.77 nm, which is noticeably higher than the corresponding simulated intensity presented in Figure 25(a). This discrepancy can be attributed primarily to the presence of a significant number of dislocations within the sample. As these dislocations undergo Bragg diffraction, they can result in local increases in scattered intensity, thus explaining the experimentally measured value exceeding the theoretical prediction. Evidence of these dislocations is clearly visible in the HCDF image shown in Figure 25(b), where the highlighted red square indicates the specific region of the sample from which the intensity is measured.

In addition to dislocations, various other factors can contribute to mismatches between experimental data and multi-slice simulation results. Potential sources of error include inaccuracies in the assumed atomic models, slicing errors, and insufficient sampling of the reciprocal space or specimen thickness during simulation. Operator errors during data acquisition and other experimental artifacts can also lead to inconsistencies, particularly if aspects such as alignment, focus, or detector calibration deviate from ideal conditions. Collectively, these considerations underscore the complex interplay of material defects, experimental parameters, and computational assumptions that influence the correlation between experimental and simulated intensity values.

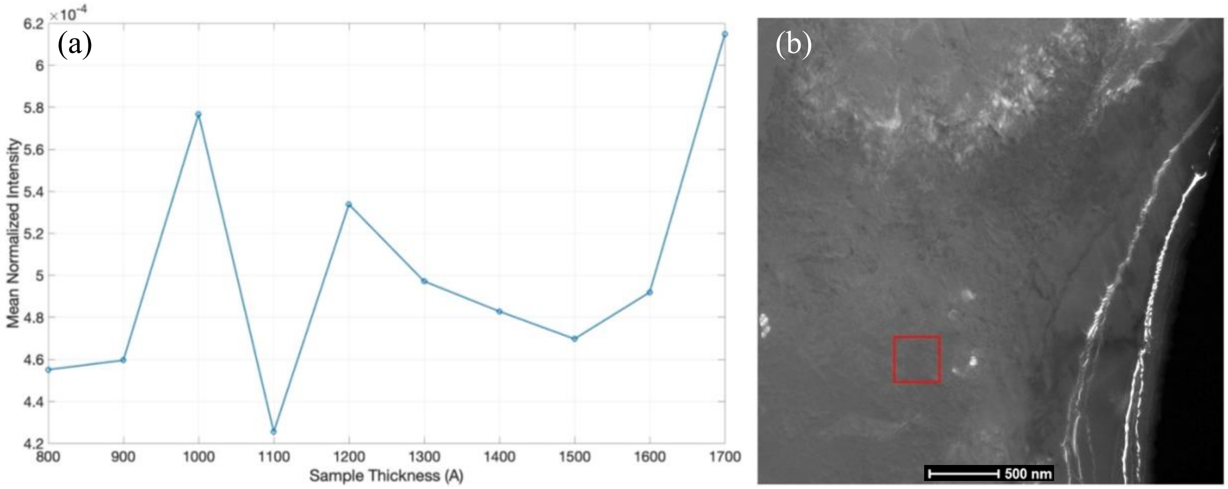

Figure 25: (a) Intensity Oscillation with sample thickness for G5 = [$\bar{4}\bar{1}56$]*, (b) HCDF image of G5 with tilt angle of* 0.631°*.*

5.6.1 Delphi TEM-Scripting Compiling and Verification

Figure 26 illustrates the successful acquisition of HCDF image using the Delphi TEM-Scripting interface. As shown in the red box, the software clearly displays the start and end times of the image acquisition process, confirming that the operation is completed without error. For testing purposes, several images are taken under different microscope parameters, but the tilt angle is maintained at 10 milliradians, and the step size is set to 30 degrees to reduce the exposure time.

Communication with the microscope via TEM-Scripting is achieved reliably, enabling both the control and retrieval of microscope parameters through the software. Furthermore, all parameters observed on the TEM user interface and those displayed in the Delphi TEM-Scripting environment are found to be consistent and in agreement, demonstrating both the robustness of the scripting process and the reproducibility of the experimental setup.

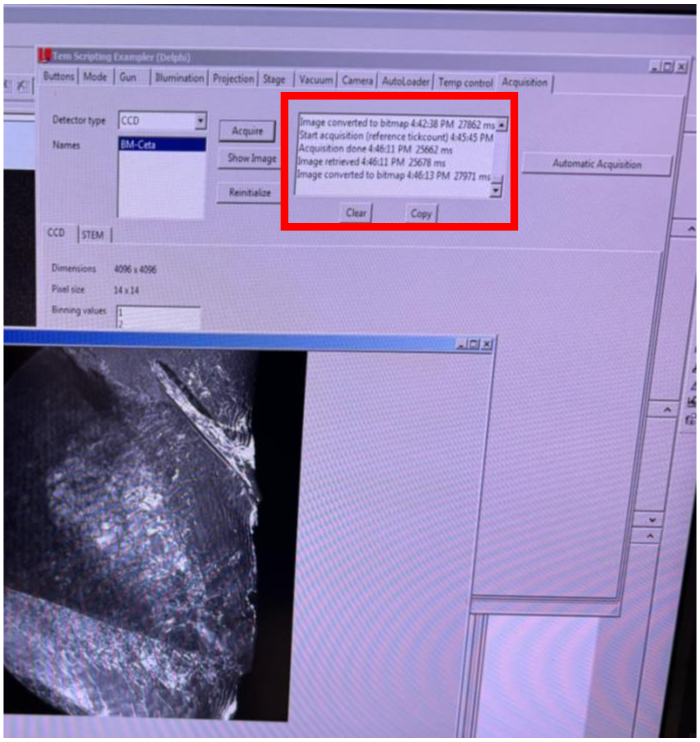

Detector type: CCD
Names: BM-Ceta

```
Image converted to bitmap 4:42:38 PM  27862 ms
Start acquisition (reference tickcount) 4:45:45 PM
Acquisition done 4:46:11 PM  25662 ms
Image retrieved 4:46:11 PM  25678 ms
Image converted to bitmap 4:46:13 PM  27971 ms
```

Dimensions: 4096 x 4096
Pixel size: 14 x 14
Binning values: 1, 2

Figure 26: Successful HCDF image acquisition with Delphi TEM-Scripting.

Figure 27 provides a comparison between HCDF images acquired through manual microscope control and that obtained automatically via Delphi TEM-Scripting. As illustrated, the images appear essentially identical; however, Figure 27(a) is captured manually. Consistency in the overall image quality demonstrates that the automatic acquisition using Delphi TEM-Scripting can produce results comparable to manual methods.

To further confirm the equivalence of the two acquisition approaches, the mean intensity of the same region highlighted in Figure 25(b) is measured. Both images show an averaged normalized intensity of approximately 0.053 over that outlined area, reinforcing the success of the automatic method. Consequently, the Delphi TEM-Scripting system offers a reliable way to acquire HCDF images with minimal operator intervention. This feature is especially beneficial for in-situ experiments, such as nano-indentation studies, where automated control and real-time data collection help reduce artifacts introduced by manual adjustments and allow for uninterrupted observation of dynamic processes.

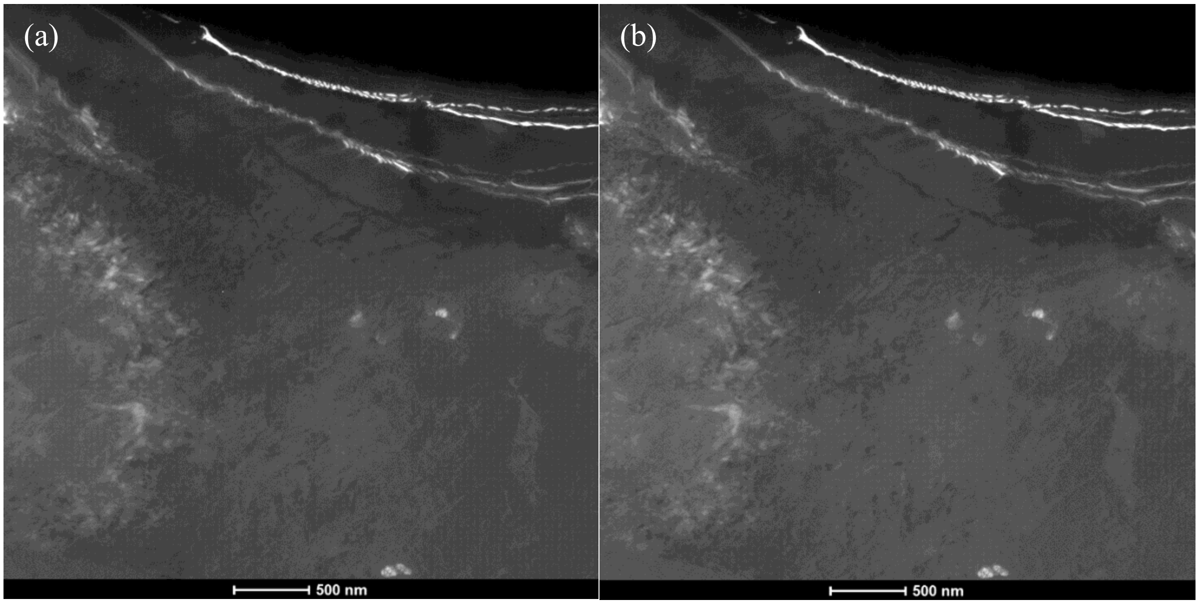

Figure 27: HCDF image of G5 acquired (a) Manually using built-in microscope controls, (b) Automatically using Delphi TEM-Scripting.

Chapter 6
Summary and Future Work

6.1 Thesis Summary

This thesis presents a unified framework that integrates both simulation and automated experimental acquisition and microscope control for HCDF imaging.

The first contribution of this work involves the development of a simulation framework incorporating several software tools to characterize the effect of crystal orientation on HCDF image contrast. Accurate atomic models of magnesium are constructed and sliced with calculated thickness to minimize numerical artifacts, while a uniform sampling of crystallographic orientations are generated to ensure comprehensive coverage of reciprocal space. Through these simulations, contrast inverse pole figures (IPFs) are produced, revealing how different zone axes influence the distribution of scattered intensity. The simulations also exposed periodic intensity oscillations associated with specific orientations and sample thicknesses, offering deeper insight into dynamical electron scattering effects.

The second key contribution is the implementation of an automated HCDF acquisition script using the integration of Delphi TEM-Scripting functions with respect to the microscope objects and capabilities. This script enables control over critical microscope parameters—including beam tilt angle, step size, and camera exposure time—allowing the electron beam to continuously sweep through a defined hollow-cone geometry while synchronizing with real-time image capture and multiple tilt series acquisition.

Simulated predictions and experimental HCDF data acquired by the scripting are validated, confirming the consistency of the results across a range of thicknesses.

6.2 Suggestions for Future Works

Several avenues exist for expanding and refining the work presented in this thesis. First, the resolution of the orientation grid can be further increased to capture a more comprehensive and fine-grained representation of the fundamental region, thereby improving the accuracy of orientation-dependent intensity predictions. Additionally, constructing and validating more atomic models, each optimized with specific slicing and sampling parameters, would enable more precise simulations, and reduce potential artifacts.

The use of more powerful computer hardware, including multi-core processors or GPU-accelerated systems, could significantly accelerate multi-slice simulations, allowing for a broader exploration of crystallographic orientations at higher resolutions. Beyond Mg, the same simulation framework can be applied to other crystalline or polycrystalline materials to test and validate its accuracy, facilitating comparative studies and potentially broadening the impact of HCDF imaging. On the software side, additional features could be integrated into the automated HCDF acquisition tool, such as algorithms for intelligently selecting camera exposure times, dwell times, and rotation angles, further enhancing image quality while minimizing operator input. Finally, incorporating emerging artificial intelligence (AI) techniques could streamline both the data acquisition and analysis processes, enabling faster feedback loops and more sophisticated image processing strategies. This AI-driven approach could pave the way for new high-throughput or fully autonomous workflows in electron microscopy.

Appendices

A.Script: Uniform grid of orientation

```
CS = crystalSymmetry('6/mmm', [0.32 0.32 0.52], 'X||a*', 'Y||b', 'Z||c');
cs_phase=loadCIF("Mg-Magnesium.cif");
SS = specimenSymmetry('1');
sphericalRegion = fundamentalSector(CS);
S2G = equispacedS2Grid('resolution', 1.5 * degree, sphericalRegion);
[beta,alpha] = polar(S2G);
re = cos(beta).*cos(alpha) + cos(alpha);
im = -(cos(beta)+1).*sin(alpha);
dGamma = atan2(im,re);
ori = orientation.byEuler(alpha,beta,dGamma,'YZY',cs_phase,SS);
G_array=ori.matrix;


r = vector3d.Z;
h = inv(ori) * r;
figure
plot(ori,'all');
figure
plot(h.symmetrise,'fundamentalRegion');
```

First, crystal symmetry is defined as a hexagonal system with the symmetry group 6/mmm, specifying the lattice parameters and the alignment of the crystal axes relative to the laboratory coordinate system. Next, phase information is loaded from a CIF file to ensure that the correct crystallographic data for magnesium is used. The specimen symmetry is then defined as “1,” indicating the absence of any additional symmetry at the macroscopic sample level.

With both crystal and specimen symmetries established, a fundamental sector on the spherical orientation space is identified. Due to symmetries inherent in the crystal structure, only a reduced region of the orientation space—called the fundamental sector—is needed to represent all unique orientations. Within this region, an equispaced spherical grid is generated. The grid is constructed at a specified resolution in degrees, creating a uniform distribution of sample directions on a sphere. These directions are expressed in terms of spherical angles, which can be converted into

Euler angles. By performing a series of trigonometric transformations, a third angle is determined so that the final set of Euler angles uniformly samples the orientation space.

Each triplet of Euler angles is then translated into an orientation object that captures how a given crystal frame is oriented relative to the specimen frame. From these orientation objects, one can easily extract rotation matrices if needed, which can be utilized for a variety of orientation-related computations, such as pole figure analysis, inverse pole figure plotting, or texture simulations.

The next step involves examining the orientation distribution by transforming a reference direction (here, the laboratory Z-axis) into each of the generated crystal reference frames. The inverse of the orientation is applied to this reference direction to see how a fixed sample direction would appear in each crystal orientation. The set of transformed directions is then symmetrized with respect to the fundamental region, ensuring that the directional data remains consistent with the crystal symmetry and does not extend outside the minimal representative domain.

Finally, visualization routines are employed to plot both the orientations and the symmetrized directions. These plots can reveal whether the orientation sampling is uniform, as intended, and allow for a direct examination of how different symmetries affect the distribution of directions within the fundamental sector.

B. Script: Creating and orthogonalizing atomic models

```
import ase
import matplotlib.pyplot as plt
import numpy as np
from pymatgen.ext.matproj import MPRester
from ase.io import write
import abtem
from abtem.atoms import pretty_print_transform
from scipy.spatial.transform import Rotation as R
from ase.visualize import view

m = np.array([
  [ 0.630203, 0,  -0.776431],
 [0, 1, 0],
 [0.776431,  0,  0.630203]
])

r = R.from_matrix(m)

vector = r.as_rotvec(degrees=True)
angle = np.linalg.norm(vector)
axis = vector/angle


Mg = ase.build.bulk('Mg', 'hcp', a=3.1954, b=3.1954, c=5.1872)
desired_rotation =  angle

Mg.rotate(desired_rotation, axis, rotate_cell=True)

Mg, transform = abtem.orthogonalize_cell(
   Mg, max_repetitions=50, return_transform=True
)

ase.io.write("/Users/farhangparsa/Desktop/Models/ThicknessModels/4-2-23/Mg_4-2-23.xyz", Mg)
```

The Python code snippet above demonstrates how to generate and manipulate an atomic model of magnesium using various Python libraries, including ASE (Atomic Simulation Environment), pymatgen, NumPy, and abTEM. Initially, necessary modules are imported, including functions for 3D transformations and visualization. A rotation matrix `m` is defined as a NumPy array that will be used to rotate the atomic structure. The rotation matrix is converted into a Rotation object from the `scipy.spatial.transform` module, which provides a convenient interface to determine rotation angles and axes. By calling `r.as_rotvec(degrees=True)`, the code retrieves the rotation vector representation of the transformation in degrees. The magnitude of this vector corresponds to the rotation angle, while its direction indicates the rotation axis. Dividing the vector by its magnitude provides a unit vector aligned with the rotation axis.

Next, a bulk hexagonal close-packed (hcp) magnesium structure is generated using ASE's built-in `build.bulk` function, which constructs a periodic crystal with given lattice parameters (in this case, `a = b = 3.1954 Å` and `c = 5.1872 Å`). The code then applies the previously determined rotation to the magnesium structure. The `Mg.rotate` method takes the rotation angle and axis as input, and optionally `rotate_cell=True` ensures that the simulation cell is also rotated accordingly, aligning the cell axes with the chosen direction. After the rotation, the `abtem.orthogonalize_cell` function is used to transform the simulation cell into an orthogonal form. This step ensures that the resulting model has orthogonal cell vectors, which can simplify subsequent image simulations or diffraction calculations. The `max_repetitions=50` parameter sets an upper limit on how many times the unit cell can be replicated during this orthogonalization process, while `return_transform=True` returns the transformation object that is used. Finally, the resulting orthogonalized magnesium structure is saved to a file in `.xyz` format, enabling the model to be readily accessed and used in other visualization or simulation tools.

C. Script: Calculating Slice thickness

```
import os
import numpy as np
from ase.io import read
import pandas as pd

# Specify the directory containing the files
directory = '/Users/farhangparsa/Desktop/Models/Mg[1-21-3]'

# Function to extract lattice parameters from .xyz file
def get_lattice_parameters(file_path):
    try:
        with open(file_path, 'r') as file:
            # Skip the first line and read the second line
            file.readline()  # Skip the first line
            second_line = file.readline().strip()

            # Extract lattice parameters
            if 'Lattice=' in second_line:
                lattice_string = second_line.split('Lattice=')[1].split('Properties=')[0].strip('" ')
                lattice_params = lattice_string.split()

                if len(lattice_params) == 9:
                    a, b, c = float(lattice_params[0]), float(lattice_params[4]), float(lattice_params[8])
                    return a, b, c
                else:
                    raise ValueError(f"Lattice parameters are not in the expected format: {lattice_params}")
            else:
                raise ValueError(f"Lattice parameter string 'Lattice=' not found in the second line: {second_line}")
    except Exception as e:
        print(f"Error processing file {file_path}: {e}")
        return None, None, None

# Function to check the criteria
def check_criteria(atomic_model, t):
    positions = atomic_model.get_positions()
    z_values = positions[:, 2]
    slice_thickness = t
    atom_counts = []

    for i in range(5):
        z_start = i * slice_thickness
        z_end = z_start + slice_thickness
        count = np.sum((z_values >= z_start) & (z_values < z_end))
        atom_counts.append(count)
```

C Script: Calculating Slice thickness

```
    X0 = atom_counts[0]
    return all(X0 - 1 <= count <= X0 + 1 for count in atom_counts[1:])

# Prepare a list to store the results
results = []

# Iterate through the files and calculate the optimum slice thickness
for i in range(1, 10):
    file_name = f'Mg1-2-3.xyz'
    file_path = os.path.join(directory, file_name)

    if not os.path.isfile(file_path):
        print(f"File {file_path} does not exist. Skipping.")
        continue

    atomic_model = read(file_path)

    # Get the c lattice parameter from the .xyz file
    a, b, c = get_lattice_parameters(file_path)
    if c is None:
        print(f"Could not read lattice parameters from {file_path}. Skipping.")
        continue

    # Calculate Cmax and Cmin
    Cmax = int(c / 1)
    Cmin = int(c / 2.5936)+1

    # Iterate from Cmin to Cmax to find the optimum slice thickness
    optimum_t = 1
    for num_slices in range(Cmin, Cmax + 1):
        t = c / num_slices
        if check_criteria(atomic_model, t):
            optimum_t = t
            break

    # Append the result to the list
    results.append({'File': file_name, 'Optimum Slice Thickness': optimum_t})
    print(f'File: {file_name}, Optimum Slice Thickness: {optimum_t}')

# Convert the results to a DataFrame
results_df = pd.DataFrame(results)

# Write the results to an Excel file
output_file = os.path.join(directory, 'slicethicknesses2.xlsx')
results_df.to_excel(output_file, index=False)
print(f'Results saved to {output_file}')
```

C Script: Calculating Slice thickness

The script begins by importing the necessary libraries, including `os` for file and directory handling, `numpy` for numeric computations, `ase.io` for reading atomic configuration files, and `pandas` for organizing and exporting results. The `directory` variable is set to the folder containing the input `.xyz` files, each representing an atomic model of magnesium or a related crystal structure. A custom function `get_lattice_parameters` is then defined, which opens each `.xyz` file, reads the header lines, and extracts the crystal lattice parameters directly from the file. These lattice parameters (a, b, c) are crucial for subsequent calculations. Another function, `check_criteria`, uses the ASE atomic model's positions to slice the crystal along the z-axis into five equal-thickness portions and count how many atoms reside in each slice. The criterion for determining if a given slice thickness `t` is acceptable is that the number of atoms in each slice must be within plus or minus one atom of the count found in the first slice. This ensures a roughly uniform atom distribution along the z-direction for the chosen thickness.

After defining these helper functions, the script loops through a series of input files. For each file, it reads the atomic model, extracts the lattice parameters, and calculates two values, `Cmax` and `Cmin`, which provide a range for how many slices the structure could reasonably be divided into. Using these bounds, the code attempts various slice counts to find the one that satisfies the uniformity criteria set forth in `check_criteria`. Specifically, it iterates from `Cmin` up to `Cmax`, computing a slice thickness `t = c / num_slices` at each step. Once it finds a thickness that meets the criteria—i.e., all slices have a nearly uniform atom count—the code considers it the "optimum slice thickness." If none of the tested thicknesses satisfy the criteria, the code defaults to a thickness of 1 (Å or the chosen unit) as a fallback.

As it processes each file, the script compiles results into a list of dictionaries, which are then converted into a Pandas DataFrame. Finally, these results are saved to an Excel file, allowing the user to easily review and compare the optimum slice thicknesses found for each model in the specified directory.

D.Script: Generating Supercells

```
import os
import numpy as np
from ase.io import read, write
from ase.build import make_supercell
from ase import Atoms

def get_lattice_parameters(file_path):
    try:
        with open(file_path, 'r') as file:
            file.readline()  # Skip the first line
            second_line = file.readline().strip()
            if 'Lattice=' in second_line:
                lattice_string = second_line.split('Lattice=')[1].split('Properties=')[0].strip('" ')
                lattice_params = lattice_string.split()
                if len(lattice_params) == 9:
                    # Extract lattice vectors
                    a_vector = [float(lattice_params[0]), float(lattice_params[1]), float(lattice_params[2])]
                    b_vector = [float(lattice_params[3]), float(lattice_params[4]), float(lattice_params[5])]
                    c_vector = [float(lattice_params[6]), float(lattice_params[7]), float(lattice_params[8])]
                    # Calculate lattice parameters
                    a = np.linalg.norm(a_vector)
                    b = np.linalg.norm(b_vector)
                    c = np.linalg.norm(c_vector)
                    return a, b, c
                else:
                    raise ValueError(f"Lattice parameters are not in the expected format: {lattice_params}")
            else:
                raise ValueError(f"Lattice parameter string 'Lattice=' not found in the second line: {second_line}")
    except Exception as e:
        print(f"Error processing file {file_path}: {e}")
        return None, None, None

# Specify the working directory
working_dir = '/Users/farhangparsa/Desktop/Models/ThicknessModels/-2201/hexagonal'  #
os.chdir(working_dir)

# Open atomic model and read the lattice parameters
file_path = 'Mg_-2201.xyz'
a, b, c_initial = get_lattice_parameters(file_path)

# Multiplication factors for each direction
multipliers = [2, 3, 66]  # [x_multiplier, y_multiplier, z_multiplier]

# Calculate new lattice parameters after multiplication
```

D Script: Generating Supercells

```
a_new = a * multipliers[0]
b_new = b * multipliers[1]
c_new = c_initial * multipliers[2]

# Create the supercell matrix
supercell_matrix = np.diag(multipliers)

# Read the initial structure and create the supercell
structure = read(file_path)
supercell = make_supercell(structure, supercell_matrix)

# Cut the supercell to new models with specified c values
c_values = list(range(10, 810, 20))
for c_cut in c_values:
    # Select atoms within the specified c value
    atoms_to_keep = [atom for atom in supercell if atom.position[2] < c_cut]

    # Create a new structure with these atoms
    new_structure = Atoms(symbols=[atom.symbol for atom in atoms_to_keep],
                          positions=[atom.position for atom in atoms_to_keep],
                          cell=[a_new, b_new, c_cut],
                          pbc=[True, True, True])

    # Prepare the content for the new .xyz file
    content = f'one unit cell of orth-Mg_-2201\n'
    content += f'{a_new:.4f} {b_new:.5f} {c_cut:.5f}\n'
    for atom in new_structure:
        content += f'12 {atom.position[0]:.4f} {atom.position[1]:.4f} {atom.position[2]:.4f} 1 0.078\n'
    content += '-1\n'

    # Write to the new .xyz file
    output_file = os.path.join(working_dir, f'Mg_-2201_{c_cut}.xyz')
    with open(output_file, 'w') as f:
        f.write(content)

print("Files generated successfully!")
```

This Python script performs a series of operations to manipulate atomic models stored in `.xyz` format. It starts by defining a previously discussed function, `get_lattice_parameters`, to extract lattice parameters (a, b, c).

It calculates new lattice parameters by scaling the original lattice constants using predefined multiplication factors for each crystallographic direction: `x`, `y`, and `z`. These factors are stored in a diagonal matrix, which is used to create a supercell from the initial structure via ASE's `make_supercell` function.

The script then iterates over a range of `c` values, representing the desired heights (or thicknesses) of atomic models. For each specified `c_cut` value, it filters the atoms within the supercell to retain only those whose `z`-coordinates are below the specified height. A new atomic model is created using these filtered atoms, with its cell updated to reflect the new lattice dimensions.

For each modified model, the script prepares content for a new `.xyz` file, including the updated lattice parameters and the positions of the selected atoms. Each atom is described with its symbol, position, and additional metadata formatted as required. The output `.xyz` file is saved in the working directory with a name indicating the corresponding `c_cut` value. The script concludes by generating the new files for all specified thicknesses, ensuring consistent formatting and structure.

E. Script: Image Quantification

```
% Define the working directory
workingDir = '/Users/farhangparsa/Desktop/Models/all200/Mg788_200';

% Define the base file name and the range of indices
baseFileName = 'Mg';
suffixFileName = '_200.tif';
indices = 1:790;  % Indices: 1, 2, 3, ..., 790
numFiles = length(indices);

% Initialize cell arrays to store data and means
data = cell(1, numFiles);
mean_values = zeros(1, numFiles);

% Loop through each file, read the data, and calculate the mean
for i = 1:numFiles
   % Construct the file name
   fileName = sprintf('%s%d%s', baseFileName, indices(i), suffixFileName);

   % Construct the full file path
   filePath = fullfile(workingDir, fileName);

   % Read the tif file
   data{i} = imread(filePath, 2);  % Read the second image from the tif file

   % Calculate the mean of the data
   mean_values(i) = mean(data{i}(:));

   % Assign data to individual variables (data1, data2, ...)
   assignin('base', sprintf('data%d', indices(i)), data{i});
end

% Assign mean values to individual variables (mean1, mean2, ...)
for i = 1:numFiles
   assignin('base', sprintf('mean%d', indices(i)), mean_values(i));
end

% Display the mean values
for i = 1:numFiles
   fprintf('The mean of data for %s%d%s is: %f\n', baseFileName, indices(i), suffixFileName, mean_values(i));
end

% Plot the mean values with respect to the model number
figure;
plot(indices, mean_values, '-o', 'LineWidth', 2, 'MarkerSize', 8);
xlabel('Model Number (1, 2, 3, ..., 790)');
ylabel('Mean Intensity');
title('Mean Intensity vs. Model Number');
grid on;
```

E Script: Image Quantification

This MATLAB script automates the process of loading a series of TIFF images, computing the mean intensity of each image, and then plotting these mean values against the model (file) index. At the beginning, key parameters such as the working directory (`workingDir`) and the file naming convention (`baseFileName`, `suffixFileName`) are defined, along with a range of indices (`1:790`) corresponding to the file sequence.

Within the main `for` loop, each TIFF file is loaded using `imread(filePath, 2)`, which reads the second image from a multi-image TIFF stack. The script calculates the mean intensity (`mean(data{i}(:))`) of the loaded image and stores it in the `mean_values` array. Additionally, the script dynamically generates variable names (`data1, data2, …`) and (`mean1, mean2, …`) in the MATLAB "base" workspace to allow for direct access to each image's data and mean value if needed.

After processing all files, the script prints out the mean values for each TIFF image, providing an overview of how the intensities vary across the 790 models. Finally, it plots the mean intensities (`mean_values`) as a function of the model number (`indices`) to visually depict the distribution or trend in image brightness/intensity across the entire dataset.

Bibliography

1. C. Kisielowski, B. Freitag, M. Bischoff, H. van Lin, et al., Detection of single atoms and buried defects in three dimensions by aberration-corrected electron microscope with 0.5-A information limit, Microscopy and Micro- ˚ analysis: the Official Journal of Microscopy Society of America, Microbeam Analysis Society, Microscopical Society of Canada 14 (2008) 469–477.
2. P.D. Nellist, M.F. Chisholm, N. Dellby, O.L. Krivanek, M.F. Murfitt, Z.S. Szilagyi, A.R. Lupini, A. Borisevich, W.H. Sides Jr., S.J. Pennycook, Direct sub-angstrom imaging of a crystal lattice, Science 305 (2004) 1741.
3. Song J, Chen J, Xiong X, Peng X, Chen D, Pan F. Research advances of magnesium and magnesium alloys worldwide in 2021. J Magnesium Alloys 2022;10(4): 863–98. https://doi.org/10.1016/j.jma.2022.04.001.
4. Song J, She J, Chen D, Pan F. Latest research advances on magnesium and magnesium alloys worldwide. J Magnesium Alloys 2020;8(1):1–41. https://doi.org/10.1016/j.jma.2020.02.003.
5. Yang Y, Xiong X, Chen J, Peng X, Chen D, Pan F. Research advances in magnesium and magnesium alloys worldwide in 2020. J Magnesium Alloys 2021; 9(3):705–47. https://doi.org/10.1016/j.jma.2021.04.001.
6. Li ZH, Sasaki TT, Bian MZ, Nakata T, Yoshida Y, Kawabe N, et al. Role of Zn on the room temperature formability and strength in Mg–Al–Ca–Mn sheet alloys. J Alloys Compd 2020;847:156347. https://doi.org/10.1016/j. jallcom.2020.156347.
7. Jayasathyakawin S, Ravichandran M, Baskar N, Anand Chairman C, Balasundaram R. Mechanical properties and applications of Magnesium alloy – _review. Mater Today Proc 2020;27:909–13. https://doi.org/10.1016/j. matpr.2020.01.255.
8. Wang S, Pan H, Xie D, Zhang D, Li J, Xie H, et al. Grain refinement and strength enhancement in Mg wrought alloys: a review. J Magnesium Alloys 2023;11(11): 4128–45. https://doi.org/10.1016/j.jma.2023.11.002.

9. Wang Q, Zhai H, Liu L, Xia H, Jiang B, Zhao J, et al. Novel Mg-Bi-Mn wrought alloys: the effects of extrusion temperature and Mn addition on their microstructures and mechanical properties. J Magnesium Alloys 2022;10(9): 2588–606. https://doi.org/10.1016/j.jma.2021.11.028.
10. Midgley, PA., Sleight, ME., & Vincent, R. (1994). The use of precession patterns for the determination of unknown structures. In Unknown (Vol. 1, pp. 919 - 920)
11. https://nanomegas.com
12. O. Scherzer. J. Appl. Phys. 20 (1949) 20.
13. Ultramicroscopy 2 (1976) 53-67 © North-Holland Publishing Company a method for producing hollow cone illumination electronically in the conventional transmission microscope William KRAKOW and Leon A. HOWLAND Xerox Corporation, Xerox Square, W114 Rochester, N. Y. 14644, USA
14. The Use of Hollow-Cone Illumination for Increasing Image Contrast in Microscopy Willis W. Mathews Transactions of the American Microscopical Society, Vol. 72, No. 2 (Apr., 1953), pp.190-195
15. Hollow cone illumination--i. Dark-field electron microscopy of biological specimens b. V. Johansen and ellen namork national institute of public health, postuttak-oslo 1, norway and t. Krekling
16. Krakow W, Howland LA. A method for producing hollow cone illumination electronically in the conventional transmission microscope. Ultramicroscopy. 1976 Dec;2(1):53-67. doi: 10.1016/s0304-3991(76)90416-2. PMID: 195374.
17. T. Geipel and W. Mader, "Practical aspects of hollow-cone imaging," Ultramicroscopy, vol. 63, no. 1, pp. 65–74, Apr. 1996, doi: 10.1016/0304-3991(96)00030-7.
18. C. Dinges, H. Kohl, H. Rose, High-resolution imaging of crystalline objects by hollow-cone illumination, Ultramicroscopy, Volume 55, Issue 1, 1994, Pages 91-100, ISSN 0304-3991, https://doi.org/10.1016/0304-3991(94)90083-3.
19. H.A. Bethe, Theorie der Beugung von Elektronen an Kristallen, Annals of Physics 87 (1928) 55.
20. A.F. Cowley, J.M. Moodie, The scattering of electrons by atoms and crystals. I. A new theoretical approach, Acta Cystallography 10 (1957) 609.

21. P.G. Self, M.A. O’Keefe, P.R Buseck, A.E.C. Spargo, Practical computation of amplitudes and phases in electron diffraction, Ultramicroscopy 11 (1983) 35.
22. B. Edwards, E.J. Kirkland, J. Silcox, D.A. Muller, Simulation of thermal diffuse scattering including a detailed phonon dispersion curve, Ultramicroscopy 86 (2001) 371.
23. M.J. Hytch, W.M. Stobbs, Quantitative comparison of high resolution TEM images with image simulations, Ultramicroscopy 53 (1994) 191.
24. Koch, C. T. (2008). *A software package for the simulation of transmission electron micrographs of inhomogeneous materials*. Ultramicroscopy, 108(12), 1412–1420.
25. Information on QSTEM: https://www.qstem.org/
26. Ophus, C. (2017). *A fast image simulation algorithm for scanning transmission electron microscopy*. Advanced Structural and Chemical Imaging, 3(13).
27. xHREM by HREM Research Inc.: https://www.hremresearch.com/
28. Multi-convergence-angle ptychography with simultaneous strong contrast and high resolution arXiv 2024 Mao, W.; Zhang, W.; Huang, C.; Zhou, L.; Kim, J. S.; Gao, S.; Lei, Y.; Wu, X.; Hu, Y.; Pei, X.; Fang, W.; Liu, X.; Song, J.; Fan, C.; Nie, Y.; Kirkland, A. I.; Wang, P.
29. S. V. Kalinin *et al.*, “Machine learning for automated experimentation in scanning transmission electron microscopy,” *npj Computational Materials*, vol. 9, no. 1, p. 227, Dec. 2023, doi: 10.1038/s41524-023-01142-0.
30. S. Kret, P. Ruterana, A. Rosenauer, D. Gerthsen, Extracting quantitative information from high resolution electron microscopy, Physica Status Solidi B 227 (2001) 247.
31. P. Stadelmann, EMS—a software package for electron diffraction analysis and HREM image simulation in materials science, Ultramicroscopy 21 (1987) 131.
32. E.J. Kirkland, Advanced Computing in Electron Microscopy, Plenum Press, New York, 1998.
33. K. Ishizuka, A practical approach for STEM image simulation based on the FFT multi-slice method, Ultramicroscopy 90 (2002) 71.
34. C Koch. /http://www.christophtkoch.com/stem/index.htmlS.
35. R. Kilaas, in: Proceedings of the 45th Annual Meeting of the Microscopy Society of America, 1987, p. 66.

36. P.R. Buseck, O' Keefe, Transactions of the American Crystallographic Association 15 (1979) 27.
37. http://www.totalresolution.com/S.
38. Z.L. Wang, Dynamical inelastic scattering in high-energy electron diffraction and imaging: a new theoretical approach, Physical Review B 41 (1990) 12818.
39. J.H. Chen, D. Van Dyck, Accurate multi-slice theory for elastic electron scattering in transmission electron microscopy, Ultramicroscopy 70 (1997) 29.
40. W. Coene, D. Van Dyck, The real space method for dynamical electron diffraction calculations in high resolution electron microscopy: I. principles of the method, Ultramicroscopy 15 (1984) 29.
41. R.F. Loane, P. Xu, J. Silcox, Thermal vibrations in convergent-beam electron diffraction, Acta Crystallographica A 47 (1991) 267.
42. B.D. Forbes, A.V. Martin, S.D. Findlay, A.J.D'alfonso, L.J. Allen, Quantum mechanical model for phonon excitation in electron diffraction and imaging using a Born–Oppenheimer approximation, Physical Review B 82 (2010) 104103.
43. B. Yao, T. Sun, A. Warren, H. Heinrich, K. Barmak, and K. R. Coffey, "High contrast hollow-cone dark field transmission electron microscopy for nanocrystalline grain size quantification," *Micron*, vol. 41, no. 3, pp. 177–182, Apr. 2010, doi: 10.1016/j.micron.2009.11.008.
44. B. Yao, H. Heinrich, C. Smith, M. Van Den Bergh, K. Cho, and Y. Sohn, "Hollow-cone dark-field transmission electron microscopy for dislocation density characterization of trimodal Al composites," Micron, vol. 42, no. 1, pp. 29–35, Jan. 2011, doi: 10.1016/j.micron.2010.08.010.
45. A. K. Kulovits, G. Facco, and J. M. K. Wiezorek, "Grain size determination in nano-scale polycrystalline aggregates by precession illumination-hollow cone dark field imaging in the transmission electron microscope," Mater. Charact., vol. 63, pp. 17–26, Jan. 2012, doi: 10.1016/j.matchar.2011.10.003.
46. B. Yao and K. R. Coffey, "Quantification of L1 phase volume fraction in annealed [Fe/Pt]n multilayer films," J. Appl. Phys., vol. 105, no. 3, p. 033901, Feb. 2009, doi: 10.1063/1.3068364.

47. Christian Suloway, Jian Shi, Anchi Cheng, James Pulokas, Bridget Carragher, Clinton S. Potter, Shawn Q. Zheng, David A. Agard, Grant J. Jensen, Fully automated, sequential tilt-series acquisition with Leginon, Journal of Structural Biology, Volume 167, Issue 1, 2009, Pages 11-18, ISSN 1047-8477, https://doi.org/10.1016/j.jsb.2009.03.019.
48. David N. Mastronarde, Automated electron microscope tomography using robust prediction of specimen movements, Journal of Structural Biology, Volume 152, Issue 1, 2005, Pages 36-51, ISSN 1047-8477, https://doi.org/10.1016/j.jsb.2005.07.007.
49. Stephan Nickell, Friedrich Förster, Alexandros Linaroudis, William Del Net, Florian Beck, Reiner Hegerl, Wolfgang Baumeister, Jürgen M. Plitzko, TOM software toolbox: acquisition and analysis for electron tomography, Journal of Structural Biology, Volume 149, Issue 3, 2005, Pages 227-234, ISSN 1047-8477, https://doi.org/10.1016/j.jsb.2004.10.006.
50. Y. Z. Tan, A. Cheng, C. S. Potter, B. Carragher, Automated data collection in single particle electron microscopy, Microscopy 65 (1) (2016) 43–56.
51. LeBeau J, Kumar A, Hauwiller M. A Universal Scripting Engine for Transmission Electron Microscopy. Microscopy and Microanalysis. 2020;26(S2):2958-2959. doi:10.1017/S1431927620023338
52. Baumeister, Wolfgang & Steven, Alasdair. (2001). Baumeister, W. & Steven, A. C. Macromolecular electron microscopy in the era of structural genomics. Trends Biochem. Sci. 25, 624-631. Trends in biochemical sciences. 25. 624-31. 10.1016/S0968-0004(00)01720-5.
53. Leapman RD. Novel techniques in electron microscopy. *Curr Opin Neurobiol*. 2004;14(5):591-598. doi:10.1016/j.conb.2004.08.004
54. Mcintosh, Richard & Nicastro, Daniela & Mastronarde, David. (2005). McIntosh, J. R., Nicastro, D. & Mastronarde, D. N. New views of cells in 3D: an introduction to electron tomography. Trends Cell Biol. 15, 43-51. Trends in cell biology. 15. 43-51. 10.1016/j.tcb.2004.11.009.
55. A. C. Steven and U. Aebi, “The next ice age: cryo-electron tomography of intact cells,” Trends in Cell Biology, vol. 13, no. 3, pp. 107–110, Mar. 2003, doi: 10.1016/S0962-8924(03)00023-0.

56. Radermacher, Michael. (2006). Weighted Back-Projection Methods. Electron Tomography: Methods for Three-Dimensional Visualization of Structures in the Cell. 10.1007/978-1-4757-2163-8_5.
57. Mannella, C.A., Buttle, K., Rath, B.K. and Marko, M. (1998), Electron microscopic tomography of rat-liver mitochondria and their interactions with the endoplasmic reticulum. BioFactors, 8: 225-228. https://doi.org/10.1002/biof.5520080309
58. Ziese, U., Janssen, A.H., Murk, J.-.-L., Geerts, W.J.C., Van der Krift, T., Verkleij, A.J. and Koster, A.J. (2002), Automated high-throughput electron tomography by pre-calibration of image shifts. Journal of Microscopy, 205: 187-200. https://doi.org/10.1046/j.0022-2720.2001.00987.x
59. Zheng, Songmu. Nonlinear Evolution Equations / by Song-Mu, Zheng. Chapman & Hall/CRC Press, 2004, https://doi.org/10.1201/9780203492222.
60. D.R.G. Mitchell, B. Schaffer, Scripting-customised microscopy tools for Digital Micrograph™, Ultramicroscopy, Volume 103, Issue 4, 2005, Pages 319-332, ISSN 0304-3991, https://doi.org/10.1016/j.ultramic.2005.02.003.
61. Spurgeon, S.R., Ophus, C., Jones, L. et al. Towards data-driven next-generation transmission electron microscopy. Nat. Mater. 20, 274–279 (2021). https://doi.org/10.1038/s41563-020-00833-z
62. A. Darbal *et al.*, "Orientation Imaging of Nanocrystalline Platinum Films in the TEM," *Microsc Microanal*, vol. 15, no. S2, pp. 1232–1233, Jul. 2009, doi: 10.1017/S1431927609093131.
63. W. Krakow and B.M. Siegel, Optik 42 (1975) 245.
64. T. Geipel and M. Hohenstein. Ultramicroscopy 45 (1992) 167.
65. BURGE, R., SMITH, G. Electron Microscopy at High Beam Accelerating Voltages. *Nature* 195, 140–141 (1962). https://doi.org/10.1038/195140a0
66. V. Grillo, E. Carlino, F. Glas, Influence of the static atomic displacement on atomic resolution Z-contrast imaging, Physical Review B 77 (2008) 054103.
67. J.M. LeBeau, S.D. Findlay, L.J. Allen, S. Stemmer, Quantitative atomic resolution scanning transmission electron microscopy, Physical Review Letters 100 (2008) 206101.
68. E. Carlino, V. Grillo, and P. Palazzari, in Microscopy of Semiconducting Materials, 2007.

69. E. Carlino, V. Grillo, Atomic resolution stem-HAADF imaging in the study of interfaces, Archives of Metallurgy and Materials 51 (2006) 23.
70. C. Dweyer, Simulation of scanning transmission electron microscope images on desktop computers, Ultramicroscopy 110 (2010) 195.
71. E.J. Kirkland. /http://people.ccmr.cornell.edu/kirkland/index.htmlS.
72. M.D. Robertson, et al., The simulation of annular dark field images of InAs/InP quantum dots, Micros and Microanal 12 (2) (2006) 714.
73. J.H. Chen, D. Van Dyck, M. Op De Beeck, Multi-slice method for large beam tilt with application to HOLZ effects in triclinic and monoclinic crystals, Acta Crystallography A 53 (1997) 576.
74. Jacob Madsen and Toma Susi. The abTEM code: transmission electron microscopy from first principles. *Open Research Europe* 1:24, 2021. doi:10.12688/openreseurope.13015.1.
75. Henderson R (1995). The potential and limitations of neutrons, electrons and X-rays for atomic resolution microscopy of unstained biological molecules. Q Rev Biophys 28, 171–193.

76. Rez P (2003). Comparison of phase contrast transmission electron microscopy with optimized scanning transmission annular dark field imaging for protein imaging. Ultramicroscopy 96, 117–124.
77. Pennycook SJ & Boatner LA (1988). Chemically sensitive structure-imaging with a scanning transmission electron microscope. Nature 336, 565.
78. Findlay SD, Shibata N, Sawada H, Okunishi E, Kondo Y, Yamamoto T & Ikuhara Y (2009). Robust atomic resolution imaging of light elements using scanning transmission electron microscopy. Appl Phys Lett 95, 191913.
79. Findlay SD, Shibata N, Sawada H, Okunishi E, Kondo Y & Ikuhara Y (2010). Dynamics of annular bright field imaging in scanning transmission electron microscopy. Ultramicroscopy 110, 903–923.
80. Transmission Electron Microscopy A Textbook for Materials Science David B. Williams C. Barry Carter
81. https://assets.thermofisher.com/TFS-Assets/MSD/Licensing-Information/TEMScripting-Software-License.pdf

82. Hartree, D. R. (1928). The Wave Mechanics of an Atom with a Non-Coulomb Central Field. *Mathematical Proceedings of the Cambridge Philosophical Society, 24*(1), 89-110. https://doi.org/10.1017/S0305004100011919
83. Fock, V. (1930). Näherungsmethode zur Lösung des quantenmechanischen Mehrkörperproblems. *Zeitschrift für Physik, 61*(1-2), 126-148. https://doi.org/10.1007/BF01340294
84. Hohenberg, P., & Kohn, W. (1964). Inhomogeneous Electron Gas. *Physical Review, 136*(3B), B864. https://doi.org/10.1103/PhysRev.136.B864
85. Kohn, W., & Sham, L. J. (1965). Self-Consistent Equations Including Exchange and Correlation Effects. *Physical Review, 140*(4A), A1133. https://doi.org/10.1103/PhysRev.140.A1133
86. Lobato, I., & Van Dyck, D. (2014). An accurate parameterization for scattering factors, electron densities, and electrostatic potentials for neutral atoms that obey all physical constraints. *Acta Crystallographica Section A: Foundations and Advances, 70*(6), 636–649. https://doi.org/10.1107/S205327331401744X
87. Jacob Madsen, Timothy J. Pennycook, and Toma Susi. Ab initio description of bonding for transmission electron microscopy. *Ultramicroscopy*, 231:113253, 2021. doi:https://doi.org/10.1016/j.ultramic.2021.113253.
88. Waasmaier, D., & Kirfel, A. (1995). New analytical scattering-factor functions for atoms and ions. *Acta Crystallographica Section A: Foundations of Crystallography, 51*(3), 416–431. https://doi.org/10.1107/S0108767394013292
89. W. Van den Broek, X. Jiang, and C.T. Koch. Fdes, a gpu-based multi-slice algorithm with increased efficiency of the computation of the projected potential. *Ultramicroscopy*, 158:89–97, 2015. doi:10.1016/j.ultramic.2015.07.005.
90. Ishizuka, K., & Uyeda, N. (1977). A new theoretical and practical approach to the multi-slice method. *Acta Crystallographica Section A: Crystal Physics, Diffraction, Theoretical and General Crystallography, 33*(6), 740–749. https://doi.org/10.1107/S0567739477001518
91. Cooley, J. W., & Tukey, J. W. (1965). An algorithm for the machine calculation of complex Fourier series. *Mathematics of Computation, 19*(90), 297–301. https://doi.org/10.2307/2003354

92. Ask Hjorth Larsen, Jens Jørgen Mortensen, Jakob Blomqvist, Ivano E. Castelli, Rune Christensen, Marcin Dułak, Jesper Friis, Michael N. Groves, Bjørk Hammer, Cory Hargus, Eric D. Hermes, Paul C. Jennings, Peter Bjerre Jensen, James Kermode, John R. Kitchin, Esben Leonhard Kolsbjerg, Joseph Kubal, Kristen Kaasbjerg, Steen Lysgaard, Jón Bergmann Maronsson, Tristan Maxson, Thomas Olsen, Lars Pastewka, Andrew Peterson, Carsten Rostgaard, Jakob Schiøtz, Ole Schütt, Mikkel Strange, Kristian S. Thygesen, Tejs Vegge, Lasse Vilhelmsen, Michael Walter, Zhenhua Zeng, Karsten Wedel Jacobsen The Atomic Simulation Environment—A Python library for working with atoms J. Phys.: Condens. Matter Vol. 29 273002, 2017

93. Jacob Madsen and Toma Susi. The abTEM code: transmission electron microscopy from first principles. *Open Research Europe* 1:24, 2021. doi:10.12688/openreseurope.13015.1.

94. Kirkland, E.J., Advanced computing in electron microscopy. Vol. 12. 1998: Springer.

95. G. Nolze and R. Hielscher, “Orientations – perfectly colored,” *Journal of Applied Crystallography*, vol. 49, no. 5, pp. 1786–1802, Oct. 2016, doi: 10.1107/S1600576716012942.

96. Y. Liu, “THE DESIGN AND DEFORMATION MECHANISM OF DEFECT- BASED MICROSTRUCTURE WITHIN MAGNESIUM”.

97. Williams, D.B. and Carterc, C.B., Transmission electron microscopy: A textbook for materials science. 2009: Springer Science &Business Media.

98. Gu, X.-F., Furuhara, T., & Zhang, W.-Z. (2016). PTCLab: free and open-source software for calculating phase transformation crystallography. *Journal of Applied Crystallography, 49*(3), 1099–1106. https://doi.org/10.1107/S1600576716006075

99. Xin Y, Hu T, Chu PK. In vitro studies of biomedical magnesium alloys in a simulated physiological environment: a review. Acta Biomater 2011;7(4): 1452–9. https://doi.org/10.1016/j.actbio.2010.12.004.

100. Griffiths D. Explaining texture weakening and improved formability in magnesium rare earth alloys. Mater Sci Technol 2014;31(1):10–24. https://doi.org/10.1179/1743284714y.0000000632.

101. Panchal M, Kaushik L, Khatirkar R, Choi S-H, Singh J. Recent advances in the in-plane shear testing of Mg alloy sheets. J Magnesium Alloys 2023;11(2):405–24. https://doi.org/10.1016/j.jma.2023.02.006.

102. Shah S, Liu M, Khan A, Ahmad F, Abdullah M, Zhang X, et al. Twinning aspects and their efficient roles in wrought Mg alloys: a comprehensive review. J Magnesium Alloys 2024;12(6):2201–30. https://doi.org/10.1016/j. jma.2024.04.035.

103. Hou C, Cao H, Qi F, Wang Q, Li L, Zhao N, et al. Investigation on microstructures and mechanical properties of Mg–6Zn–0.5 Ce–xMn (x=0 and 1) wrought magnesium alloys. J Magnesium Alloys 2022;10(4):993–1003. https://doi.org/ 10.1016/j.jma.2020.09.019.

104. Xu J, Liu W, Jiang B, Yang H, Li X, Kang Y, et al. Forming novel texture and enhancing the formability in Mg–3Al–Zn alloy sheets fabricated by transverse gradient extrusion. J Mater Res Technol 2022;18:3143–9. https://doi.org/ 10.1016/j.jmrt.2022.03.165.

105. Bian M, Huang X, Chino Y. Substantial improvement in cold formability of concentrated Mg–Al–Zn–Ca alloy sheets by high temperature final rolling. Acta Mater 2021;220:117328. https://doi.org/10.1016/j.actamat.2021.117328.

106. Shi B, Yang C, Peng Y, Zhang F, Pan F. Anisotropy of wrought magnesium alloys: a focused overview. J Magnesium Alloys 2022;10(6):1476–510. https://doi.org/ 10.1016/j.jma.2022.03.006.

107. Wang H, Sun X, Kurukuri S, Worswick M, Li D, Peng Y, Wu P. The strain rate sensitive and anisotropic behavior of rare-earth magnesium alloy ZEK100 sheet. J Magnesium Alloys 2023;11(3):882–91. https://doi.org/10.1016/j. jma.2021.06.010.

108. Wen J, de Rango P, Allain N, Laversenne L, Grosdidier T. Improving hydrogen storage performance of Mg-based alloy through microstructure optimization. J Power Sources 2020;480:228823. https://doi.org/10.1016/j. jpowsour.2020.228823.

109. Edalati K, Akiba E, Botta WJ, Estrin Y, Floriano R, Fruchart D, et al. Impact of severe plastic deformation on kinetics and thermodynamics of hydrogen storage in magnesium and its alloys. J Mater Sci Technol 2023;146:221–39. https://doi. org/10.1016/j.jmst.2022.10.068.

110. Jorge Jr AM, De Lima GF, Triques MRM, Botta WJ, Kiminami CS, Nogueira RP, et al. Correlation between hydrogen storage properties and textures induced in magnesium through ECAP and cold rolling. Int J Hydrogen Energy 2014;39(8): 3810–21. https://doi.org/10.1016/j.ijhydene.2013.12.154.

111. Zhang F, Liu Z, Yang M, Su G, Zhao R, Mao P, et al. Microscopic mechanism exploration and constitutive equation construction for compression characteristics of AZ31-TD magnesium alloy at high strain rate. Mater Sci Eng: A 2020;771:138571. https://doi.org/10.1016/j.msea.2019.138571.

112. Yang B, Shi C, Ye X, Teng J, Lai R, Cui Y, et al. Underlying slip/twinning activities of Mg-xGd alloys investigated by modified lattice rotation analysis. J Magnesium Alloys 2023;11(3):998–1015. https://doi.org/10.1016/j.jma.2021.06.008.

113. Yin DD, Boehlert CJ, Long LJ, Huang GH, Zhou H, Zheng J, Wang QD. Tension-compression asymmetry and the underlying slip/twinning activity in extruded Mg–Y sheets. Int J Plast 2021;136:102878. https://doi.org/10.1016/j. ijplas.2020.102878.

114. Yaghoobi M, Voyiadjis G, Sundararaghavan V. Crystal plasticity simulation of magnesium and its alloys: a review of recent advances. Crystals 2021;11(4):435. https://doi.org/10.3390/cryst11040435.

115. Agnew SR, Yoo MH, Tom´e CN. Application of texture simulation to understanding mechanical behavior of Mg and solid solution alloys containing Li or Y. Acta Mater 2001;49(20):4277–89. https://doi.org/10.1016/S1359-6454(01)00297-X.

116. Zhou R, Roy A, Silberschmidt VV. A crystal-plasticity model of extruded AM30 magnesium alloy. Comput Mater Sci 2019;170:109140. https://doi.org/10.1016/j.commatsci.2019.109140.

117. Liu B-Y, Liu F, Yang N, Zhai X-B, Zhang L, Yang Y, et al. Large plasticity in magnesium mediated by pyramidal dislocations. Science 2019;365(6448):73–5. https://doi.org/10.1126/science.aaw2843.

118. Song B, Guo N, Liu T, Yang Q. Improvement of formability and mechanical properties of magnesium alloys via pre-twinning: a review. Mater Des 2014;62: 352–60. https://doi.org/10.1016/j.matdes.2014.05.034.

119. Tom´e CN, Beyerlein IJ, McCabe RJ. A multi-scale statistical study of twinning in magnesium. JOM 2011;63:19–23. https://doi.org/10.1007/s11837-011-0038-x.

120. Liu Q. Research progress on plastic deformation mechanism of Mg alloys. Acta Metall Sin 2010;46(11):1458–72. https://doi.org/10.3724/SP. J.1037.2010.00446.

121. Zhang J, Joshi SP. Phenomenological crystal plasticity modeling and detailed micromechanical investigations of pure magnesium. J Mech Phys Solid 2012;60 (5):945–72. https://doi.org/10.1016/j.jmps.2012.01.005.

122. Herrera-Solaz V, Hidalgo-Manrique P, P´erez-Prado MT, Letzig D, Llorca J, Segurado J. Effect of rare earth additions on the critical resolved shear stresses of magnesium alloys. Mater Lett 2014;128:199–203. https://doi.org/10.1016/j. matlet.2014.04.144.

123. Wang Y, Huang J. Texture analysis in hexagonal materials. Mater Chem Phys 2003;81(1):11–26. https://doi.org/10.1016/S0254-0584(03)00168-8.

124. Fan H, Wang Q, Tian X, El-Awady JA. Temperature effects on the mobility of pyramidal <c +a >dislocations in magnesium. Scripta Mater 2017;127:68–71. https://doi.org/10.1016/j.scriptamat.2016.09.002.

125. Alekseeva, S., et al., *Grain boundary mediated hydriding phase transformations in individual polycrystalline metal nanoparticles.* Nature Communications, 2017. 8(1): p. 1084.

126. Dingley, D.J., *Orientation imaging microscopy for the transmission electron microscope.* Microchimica Acta, 2006. 155(1): p. 19-29.

127. Wu, G. and Zaefferer, S., *Advances in TEM orientation microscopy by combination of dark-field conical scanning and improved image matching.* Ultramicroscopy, 2009. 109(11): p. 1317-1325.

128. Liu, H., et al., *Three-dimensional orientation mapping in the transmission electron microscope.* Science, 2011. 332(6031): p. 833-834.

129. Kumar, V., *Orientation imaging microscopy with optimized convergence angle using CBED patterns in TEMs.* IEEE transactions on image processing, 2013. 22(7): p. 2637-2645.

130. Rauch, E., et al., *Automatic crystal orientation and phase mapping in TEM by precession diffraction.* Microscopy and Analysis, 2008. 128: p. S5-S8.

131. Ke, M., et al., *Observation and measurement of grain rotation and plastic strain in nanostructured metal thin films.* Nanostructured Materials, 1995. 5(6): p. 689-697.

132. Zhang, Y., G.J. Tucker, and J.R. Trelewicz, *Stress-assisted grain growth in nanocrystalline metals: Grain boundary mediated mechanisms and stabilization through alloying.* Acta Materialia, 2017. 131: p. 39-47.

133. Wang, Y.B., et al., *Deformation-induced grain rotation and growth in nanocrystalline Ni.* Applied Physics Letters, 2008. 92(1): p. 011903.

134. Williams, D.B. and Carterc, C.B., *Transmission electron microscopy: A textbook for materials science*. 2009: Springer Science &Business Media.

135. Yao, B., et al., *Hollow-cone dark-field transmission electron microscopy for dislocation density characterization of trimodal Al composites.* Micron, 2011. 42(1): p. 29-35.

136. Yao, B., et al., *High contrast hollow-cone dark field transmission electron microscopy for nanocrystalline grain size quantification.* Micron, 2010. 41(3): p. 177-182.

137. Jin, M., et al., *Direct observation of deformation-induced grain growth during the nanoindentation of ultrafine-grained Al at room temperature.* Acta Materialia, 2004. 52(18): p. 5381-5387.

138. T. B. Britton et al., *Acta Mater.* 59, 5383–5393 (2011).

139. J. M. Zuo & J. C. H. Spence, *Advanced Transmission Electron Microscopy: Imaging and Diffraction in Nanoscience*, Springer (2017).

140. A. Ghasemi et al., *Mater. Charact.* 157, 109930 (2019).

141. S. Sandlobes & D. Raabe, *Acta Mater.* 59, 429–439 (2011).

142. M. R. Barnett, *Mater. Sci. Eng. A* 464, 8–16 (2007).

143. Pozsgai, I., *Mass thickness determination and microanalysis of thin films in the TEM—Revisite.* Ultramicroscopy, 2007. 68(1): p. 69-75.

144. Rotunno, Enzo. (2012). STEM_CELL: A software tool for electron microscopy: Part I-simulations. Ultramicroscopy. 125. 10.1016/j.ultramic.2012.10.016.

145. J.M. de la Rosa-Trevín, A. Quintana, L. del Cano, A. Zaldívar, I. Foche, J. Gutiérrez, J. Gómez-Blanco, J. Burguet-Castell, J. Cuenca-Alba, V. Abrishami, J. Vargas, J. Otón, G. Sharov, J.L. Vilas, J. Navas, P. Conesa, M. Kazemi, R. Marabini, C.O.S. Sorzano, J.M. Carazo,

146. Scipion: A software framework toward integration, reproducibility and validation in 3D electron microscopy, Journal of Structural Biology, Volume 195, Issue 1, 2016, Pages 93-99, ISSN 1047-8477, https://doi.org/10.1016/j.jsb.2016.04.010.

147. G. C. Lander, S. M. Stagg, N. R. Voss, A. Cheng, D. Fellmann, J. Pulokas, C. Yoshioka, C. Irving, A. Mulder, P. W. Lau, D. Lyumkis, C. S. Potter, and B. Carragher. Appion: an integrated, database-driven pipeline to facilitate EM image processing. J. Struc. Biol., 166(1):95–102, 2009.

148. J. Frank et al., "SPIDER and WEB: Processing and visualization of images in 3D EM," *J. Struct. Biol.*, vol. 116, no. 1, pp. 190–199, 1996.

149. S. J. Ludtke, P. R. Baldwin, and W. Chiu, "EMAN: Semiautomated software for high-resolution single-particle reconstructions," *J. Struct. Biol.*, vol. 128, no. 1, pp. 82–97, 1999.

150. M. Hohn et al., "SPARX, a new environment for cryo-EM image processing," *J. Struct. Biol.*, vol. 157, no. 1, pp. 47–55, 2007.

151. J. M. de la Rosa-Trevín et al., "Xmipp 3.0: An improved software suite for image processing in electron microscopy," *J. Struct. Biol.*, vol. 200, no. 3, pp. 303–312, 2017.

152. I. Lobato and D. Van Dyck, "MULTEM: A new multislice program to perform accurate and fast electron diffraction and imaging simulations using graphics processing units," Ultramicroscopy, vol. 156, pp. 9–17, 2015 pmc.ncbi.nlm.nih.gov; and I. Lobato et al., Ultramicroscopy, vol. 168, pp. 17–27, 2016

153. J. Oelerich et al., "STEMsalabim: a high-performance computing cluster friendly code for STEM image simulations of thin specimens," Ultramicroscopy, vol. 177, pp. 91–96, 2017

154. L.J. Allen, A.J. D′Alfonso, S.D. Findlay, Modelling the inelastic scattering of fast electrons, Ultramicroscopy, Volume 151, 2015, Pages 11-22, ISSN 0304-3991, https://doi.org/10.1016/j.ultramic.2014.10.011.